UNIVERSITÄT BONN
Physikalisches Institut

Beauty Photoproduction using Decays into Muons at HERA

von
Ursula Samson geb. Meyer

Inclusive cross-sections for the production of open beauty in ep collisions at HERA are measured. The data were recorded with the ZEUS detector between 1996 and 2000. The measurements are restricted to photoproduction processes, i.e. collision events with small four-momentum transfer squared, $Q^2 \approx 0$. Two jets with transverse momentum $p_T > 7(6)\,\text{GeV}$ and pseudo-rapidities $|\eta| < 2.5$ are required. The flavour is tagged by the identification of muons from semi-leptonic decays of the beauty quark. The variable used to discriminate between beauty and background is the transverse momentum of the muon with respect to the jet axis. The fraction of beauty is determined by a fit of Monte Carlo templates to the data. Cross-sections have been measured as a function of the muon and jet variables as well as a function of dijet correlation variables. Dijet correlations in beauty production have been measured for the first time in ZEUS and are found in agreement with QCD NLO predictions.

Post address:
Nussallee 12
53115 Bonn
Germany

BONN-IR-2008-06
Bonn University
May 2008
ISSN-0172-8741

UNIVERSITÄT BONN
Physikalisches Institut

Beauty Photoproduction using Decays into Muons at HERA

von
Ursula Samson geb. Meyer

Erscheinungsjahr: 2008
Referent: Prof. Dr. Ian C. Brock
Korreferent: Prof. Dr. Klaus Desch

Tag der Promotion: 21.05.2008

Contents

1. Introduction

The Standard Model (SM) of particle physics is a theory which provides a successful description of the elementary structure of matter. In this theory matter is made of 12 fundamental fermions; quarks and leptons, plus their antiparticles. Interactions between these fermions are mediated by the exchange of gauge bosons. Leptons are observed as free particles, while the quarks can only be observed in bound states (hadrons) due to so-called confinement. This is an important property of Quantum Chromodynamics (QCD), which is the theory of the strong interaction. For processes at high energy (higher than about 1 GeV) the coupling strength becomes small and perturbative methods can be applied. Thus perturbative calculations should be reliable in all processes where a high enough energy scale is present. The masses of heavy quarks provide such a scale hence processes involving heavy quarks provide a rich testing ground for QCD, although the presence of more than one hard scale (e.g. additional large transverse momenta) can complicate the calculations.

The HERA electron/positron-proton collider provides energies high enough for a hard scale. Therefore a multitude of experimental tests of Quantum Chromodynamics are possible: the running of the coupling constant, scaling violations in deep inelastic scattering, measurements of jets and event shapes, and the production of vector mesons or heavy quarks. The beam energies of the machine allow for the production of beauty and charm quarks.

The aim of this thesis is the measurement of beauty production cross-sections in ep collisions at HERA using the ZEUS detector. Beauty quarks are identified through hadrons with non-zero flavour quantum number. This is often referred to as “open” beauty production. The tagging of beauty is done with the help of semi-leptonic decays of the beauty hadrons originating from the hadronisation of the quarks. For the data analysed in this thesis, no lifetime information of the heavy hadrons is available, therefore the beauty tagging is based on the muon identification and kinematics of the semi-leptonic decays with respect to the heavy quark jets. The muon identification has been improved substantially with respect to previous analyses. The redundancy of different muon finding algorithms and a larger geometrical coverage made it possible to lower the muon p_T cut. Together with the higher efficiency for the muon finding, the number of events could be increased by a factor 10 and the number of beauty events by a factor of 7.5. This made it possible to measure for the first time at ZEUS dijet correlations in beauty.

Another major aspect of this thesis is the study of the feasibility to determine the fake muon background from the data. This opens the possibility to enlarge the kinematic range to regions where the background determination from Monte Carlo simulations is no longer possible. This is of special interest for the HERA II running period, where a micro-vertex detector allows heavy flavour to be tagged using lifetime information. A beauty analysis without a jet requirement and only one muon would then be possible using this background determination method.

For experimental reasons this analysis is restricted to low momentum transfers ($Q^2 < 1\,\text{GeV}$), where the photon is quasi-real. The physics of hard photoproduction with two jets and the production of heavy quarks in *ep* collisions is the subject of Chapter 2. In Chapter 3 a short overview of previous results on heavy-flavour production at hadron colliders is given. In Chapter 4 the experimental setup, i.e. the HERA machine and the ZEUS detector, is presented. Chapter 5 describes the reconstruction of the different final-state quantities such as jets and muons, with emphasis on the new general muon reconstruction. In Chapter 6 the different data and Monte Carlo samples are introduced and the event selection is discussed. In Chapter 7 the method used to identify beauty is explained. Chapter 8 introduces a method to determine the light flavour background from the data and gives the results of tests on two different analyses, where an alternative method to determine the background also exists. In Chapter 9 the results of the cross-section measurements are given and compared to next-to-leading-order predictions. Chapter 10 then concludes the thesis.

2. Beauty Production - Theoretical Context

2.1. The Standard Model

The Standard Model (SM) [1] of elementary particle physics comprises a set of theories describing the fundamental particles and their interactions. To our understanding matter is made up from 12 fundamental constituents (leptons and quarks), which are spin 1/2 fermions, plus their corresponding antiparticles. Down to a resolution of 10^{-18}m no substructure of these particles has been observed so far. They are grouped in three generations ordered in mass as indicated in Table 2.1. Only fermions of the first generation are stable, the other particles only exist as short-lived states that can be produced e.g. in high-energy particle collisions. They decay in a chain back to particles of the first generation. The topic of this thesis is the analysis of the production mechanism of one of these short-lived states.

There are only four forces: gravity, electromagnetism, the weak force and the strong force. Each of these forces is transmitted by different particles called gauge bosons (bosons are integer spin particles). Their different strengths in interacting with matter are referred to as couplings. While quarks can interact via all forces, leptons do not carry a colour charge and can therefore not interact via the strong force.

The interaction transmitted by those forces can be described using field theories. In field theories particles are associated with functions of space-time coordinates called fields, which can be regarded as generalised coordinates.

For a given set of observables corresponding to some interaction, it is generally possible to construct so-called gauge theories with the appropriate symmetries and kinematics. A relatively easy example of a gauge theory is quantum electrodynamics (QED). The coupled electron field has to be invariant under local gauge transformations of the following form:

$$\Psi(x) \rightarrow e^{ie\Theta(x)}\Psi(x) \quad . \tag{2.1}$$

The free electron field is not invariant under such a transformation, therefore the derivative, ∂_μ, in the Lagrangian has to be substituted by the covariant derivative, D_μ

$$\partial_\mu \rightarrow D_\mu = \partial_\mu + ieA_\mu \ , \tag{2.2}$$

where e is the electron charge and A_μ is the photon field, which transforms as

$$A_\mu \rightarrow A_\mu - \frac{1}{e}\partial^\mu\Theta(x) \ . \tag{2.3}$$

	Fermions			
	Leptons		Quarks	
Electric Charge [e]	0	-1	$+2/3$	$-1/3$
Generation				
1st	ν_e	e	u	d
2nd	ν_μ	μ	c	s
3rd	ν_τ	τ	t	b

Bosons/Mass [GeV]		Typical coupling strength
g / $m = 0$	strong	$0.1 - 1$
γ / $m = 0$	electromagnetic	$\frac{1}{137}$
$W^\pm$, Z / $m = 80$	weak	$\frac{1}{30}$ at scale of M_W
(graviton)	(gravitation)	10^{-38}

Table 2.1: The elementary fermions, their charge in units of the electron charge (e), the fundamental forces that act on them and the corresponding mediator bosons. A further electroweak boson, the Higgs, is predicted by the Standard Model, but has not been observed so far.

The requirement of local gauge invariance fixes the interaction between the fields, but not the coupling strength. In general group generators obey the commutation rules

$$[T^a, T^b] = f^{abc} T^c \ . \tag{2.4}$$

In electromagnetism there is only one group generator related to the electric charge which commutes with itself, the group is therefore called Abelian. For non-Abelian groups with non-vanishing f^{abc} the covariant derivative has the form:

$$D_\mu = \partial_\mu + ie\vec{T}\vec{A}_\mu \ , \tag{2.5}$$

giving rise to one vector field per generator. Both the combined theory of electroweak interactions and the theory of the strong force, quantum chromodynamics (QCD), are non-Abelian gauge theories. The non-vanishing f^{abc} leads to a self-coupling of the mediating bosons (weak intermediate vector bosons and gluons). The combination of the electroweak theory and QCD is called the Standard Model. A detailed description can be found in standard textbooks e.g. [2].

2.2. Quantum Chromodynamics

Quantum Chromodynamics (QCD) is the non-Abelian gauge theory of the strong interaction [3]. The main aspects will be discussed here and further details concerning the heavy quark production will be given in Section 2.4.

Within QCD, the gauge bosons called gluons interact with quarks carrying colour charges. These colour charges have nothing to do with colour in everyday life, but are a theoretical construct using properties of colour. In contrast to QED, the gauge bosons in QCD are not neutral which opens the possibility of gluon self-interactions. As QCD is based on the SU(3) gauge group, the gluons contain three different colours (red, green, blue) and the corresponding anti-colours. They build a colour octet of linearly independent colour-anticolour combinations and a colour singlet, which has not been observed so far.

Up to now no free colour charge has been observed. The quarks and gluons have therefore to 'fragment' (split and recombine) into hadrons (e.g. mesons, $q\bar{q}$, or baryons, qqq or $\bar{q}\bar{q}\bar{q}$) which at high enough energies can be observed as localised clusters of particles called jets. This is called *confinement* and can be explained with the self-coupling of the gluons, leading to an anti-screening effect of the colour charge. For the same reason, the strong coupling constant becomes small at small distances. Here, quarks and gluons behave locally as if they were free particles. This is called *asymptotic freedom*. In Figure 2.1 the dependence of a_s on the relevant energy scale is shown. For high energies, corresponding to small distances, the coupling is small and perturbative methods (pQCD) can be used, while for low energies, i.e. long distances, the coupling and thus the binding force becomes large and one has to rely on non-perturbative models.

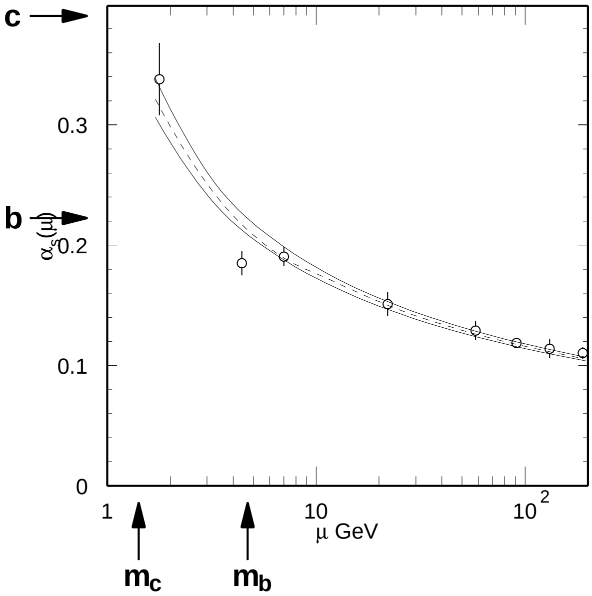

Figure 2.1: The dependence of the strong coupling, α_s, on the renormalisation scale, μ. The data are, in increasing order of μ, τ width, Υ decays, deep inelastic scattering, e^+e^- event shapes at 22 GeV from the JADE data, event shapes at TRISTAN at 58 GeV, Z width, and e^+e^- event shapes at 135 and 189 GeV [4].

Going from leading order (LO) to next-to-leading-order (NLO) calculations, quark and gluon loop Feynman diagrams appear which lead to *ultraviolet divergencies* when integrating over phase-space. These divergencies can be removed through renormalisation, that is replacing the divergent integrals by finite expressions. Doing so, a new parameter, μ, the *renormalisation scale* of dimension mass is introduced. As μ is arbitrary, no physical quantity should depend on its value and a set of rules have to be specified in order to determine μ. The *renormalisation scheme* used in this thesis is the so-called *modified minimal subtraction scheme* $\overline{MS}$ [5]. In this scheme the divergencies are removed through dimensional regularization which means that the space-time integration dimensions are changed from 4 to 4 - ϵ ($\int d^4 \rightarrow lim_{\epsilon\rightarrow 0} \int d^{4-\epsilon}$). This mechanism leads to a coupling constant of mass dimension ϵ. Therefore an arbitrary parameter μ of unit mass dimension is introduced, in order to keep the coupling dimensionless. The poles at $\epsilon = 0$ together with some constants appearing at the pole are substracted and the bare coupling is replaced by the renormalised one [6]. In order not to depend on the renormalisation scale, physical quantities have to fulfill the renormalisation group equation:

$$\mu^2 \frac{\partial \alpha_s(\mu)}{\partial \mu^2} = \beta(\alpha_s(\mu)) \ . \tag{2.6}$$

The β-function can be written as a perturbative expansion in α_s, describing the dependence of α_s on the renormalisation scale (running coupling). In LO the solution of this equation can be written as:

$$\alpha_s(\mu) = \frac{12\pi}{(33 - 2n_f)\ln(\mu^2/\Lambda^2_{QCD})} \ . \tag{2.7}$$

Λ_{QCD} is a free parameter which has to be determined experimentally. It represents the scale at which the coupling would diverge, if extrapolated outside the perturbative domain. Its value depends on the number of active flavours, n_f, ($m_q \leq \mu$) and the chosen renormalisation scheme. Consequently the coupling is small for $\mu \gg \Lambda_{QCD}$ and perturbative calculations break down for $\mu \rightarrow \Lambda_{QCD}$.

In the $\overline{MS}$ scheme and for five active flavours, Λ_{QCD} has been measured to [7]:

$$\Lambda^{(5)}_{QCD} = 217^{+25}_{-23}\text{MeV} \ . \tag{2.8}$$

2.3. Electron-Proton Scattering at HERA

Electron[1]-proton scattering provides a rich source of information on the electroweak and strong force as well as on the photon and proton structure. In the following the main aspects and variables of ep scattering are introduced and some main results are given.

Generally there are two processes contributing to the total ep cross-section depending on the charge of the exchanged boson. If it is neutral (γ or Z), one speaks of a neutral-current (NC) process $ep \rightarrow eX$, which is shown in first order in Figure 2.3 (left). In charged-current (CC) processes with an exchanged $W^{\pm}$ shown in

---

[1] Electron is used in this thesis for both the electron and the positron.

Figure 2.3 (right) the incoming electron becomes a neutrino, ν_e, and escapes undetected.

The variables used to describe the kinematics of a particular scattering event are expressed in terms of the 4-momenta of the particles taking part: the incoming (k) and the scattered electron or neutrino (k'), the incoming proton (P) and the exchanged boson (q, $q = k - k'$).

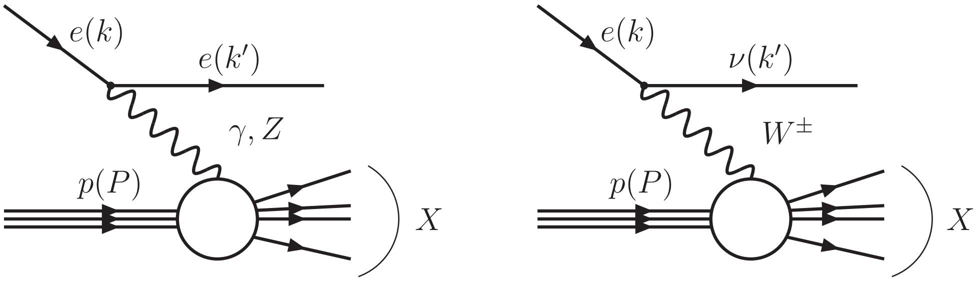

Figure 2.2: Diagram of the ep scattering processes at HERA. In the NC case a γ or Z boson is exchanged, while in the CC case the reaction takes place by a W boson exchange.

The following Lorentz-invariant variables describe the event kinematics: The centre-of-mass energy, $\sqrt{s}$, of the ep system:

$$s = (k + P)^2 \; ; \tag{2.9}$$

the square of the transfered momentum or photon virtuality[2]:

$$Q^2 = -q^2 = (k - k')^2 \; , \quad 0 \leq Q^2 \leq s \; ; \tag{2.10}$$

the centre-of-mass energy of the hadronic system:

$$W^2 = (P + q)^2 \; ; \tag{2.11}$$

the Bjorken scaling variable, x:

$$x = Q^2/(2P \cdot q) \; ; \tag{2.12}$$

the so-called inelasticity y:

$$y = (P \cdot q)/(P \cdot k) \; . \tag{2.13}$$

At fixed $\sqrt{s}$, only two of these variables are independent. For example, if x and y are given:

$$\begin{aligned} Q^2 &= (s - m_p^2)\, xy \;\approx\; sxy \; , \\ W^2 &= (s - m_p^2)\, y - Q^2 + m_p^2 \;\approx\; sy - Q^2 \\ &= Q^2(\frac{1}{x} - 1) + m_p^2 \; , \end{aligned} \tag{2.14}$$

---

[2] As the exchange of a Z boson is strongly suppressed for $Q^2 < m_Z^2$, the exchanged boson will mainly be a photon in NC events.

where the indicated approximation means neglecting the mass of the proton, m_p; the electron mass, m_e, is always neglected. The squared four-momentum transfer, q^2, is negative, i.e. time-like, so Q^2 is positive. Q^2 is called the "virtuality" of the photon. The higher Q^2, the further the photon is off its mass shell. Two regimes are defined depending on Q^2. Events with a high photon virtuality of $Q^2 \geq 1\,\mathrm{GeV}^2$ are referred to as *Deep Inelastic Scattering* (DIS), whereas those where the exchanged photon is only weakly virtual ($Q^2 \ll 1\,\mathrm{GeV}^2$) are called *photoproduction*.

In the simplest model of the proton, the *quark parton model* (QPM), in which the proton is assumed to be composed of a number of point-like partons, and boosting to the infinite momentum frame, $E_p \gg m_p$, the Bjorken scaling variable, x, can be interpreted as the fraction of the proton momentum carried by the struck (massless) quark. Consequently it ranges from 0 to 1. Going to the proton rest frame, y measures the relative energy transfer to the proton. Thus, its range is from 0 (no energy transfer) to 1 (all energy transferred). It can be thought of as the *inelasticity* of an event.

These Lorentz invariants can be determined by measurements in the laboratory, e.g. the energy, E_e', of the scattered electron and its angle, θ_e, with respect to the incoming proton. Defining the laboratory coordinate system as:

$$\begin{aligned} k &= (E_e, 0, 0, -E_e) \ , \\ k' &= (E_e', E_e' \sin\theta_e \cos\varphi_e, E_e' \sin\theta_e \sin\varphi_e, -E_e \cos\theta_e) \ , \\ P_p &= (E_p, 0, 0, E_p) \ , \end{aligned} \tag{2.15}$$

the kinematic variables can be calculated as:

$$Q^2 = 2E_eE_e'(1+\cos\theta_e) \ , \qquad s = 4E_eE_P \ , \tag{2.16}$$

$$y = (E_e'/2E_e)(1-\cos\theta_e) \ , \qquad x = Q^2/4yE_eE_P \ . \tag{2.17}$$

2.3.1. Cross-Section and Structure Functions

Calculating the *ep* cross-section in lowest order QED+EW, one has to take into account the structure of the proton. The cross-section can be separated into a leptonic and a hadronic part

$$d\sigma \sim L_{\mu\nu} \times W_{\mu\nu} \ , \tag{2.18}$$

where $L_{\mu\nu}$ is the leptonic tensor, describing the leptonic part of the interaction, and $W_{\mu\nu}$ is the hadronic tensor. While the leptonic part can be calculated using QED, the hadronic tensor, describing the proton part of the interaction cannot be calculated from first principles. Using symmetries and kinematic constraints, this part of the cross-section can be described by two unintegrated process-dependent form factors called structure functions $F_1(x, Q^2)$ and $F_2(x, Q^2)$ which depend on two independent variables, e.g. x and Q^2. A third structure function, F_3, appears at high Q^2 if the γ-Z interference is included. Using these structure functions the double differential cross section in x and Q^2 for photon (NC) and W (CC) exchange can be expressed as [7]:

$$\frac{d^2\sigma_{NC}}{dxdy} = \frac{4\pi\alpha^2}{xyQ^4}\left[\left(1-y-\frac{x^2y^2M^2}{Q^2}\right)F_2^{NC}+y^2xF_1^{NC}\mp\left(y-\frac{y^2}{2}\right)xF_3^{NC}\right] , \tag{2.19}$$

$$\begin{aligned}\frac{d^2\sigma_{CC}}{dxdy} &= \frac{4\pi\alpha^2}{xyQ^4}(1\pm\lambda^2)\frac{1}{2}\left(\frac{G_F M_W^2}{4\pi\alpha}\frac{Q^2}{Q^2+M_W^2}\right)^2 \\ &\left[\left(1-y-\frac{x^2y^2M^2}{Q^2}\right)F_2^{CC}+y^2xF_1^{CC}\mp\left(y-\frac{y^2}{2}\right)xF_3^{CC}\right] ,\end{aligned} \tag{2.20}$$

where α is the fine structure constant, $G_F = \frac{\sqrt{2}}{8}\left(\frac{g_w}{M_W}\right)^2$ denotes the Fermi Constant, λ is the helicity of the incoming lepton, with ± for $l^{\pm}$. In the last term the – sign is taken for an incoming e^+ and the + sign for an incoming e^-.

In the simple QPM, assuming the proton to be made of point-like spin 1/2 particles, the scattering process can be regarded as simply a scattering off a point-like particle inside the proton. As no further structure can be resolved, the Q^2 dependence vanishes and the structure functions F_1 and F_2 represent the sums over quark and anti-quark densities. They are connected via the Callan-Gross relation [8]:

$$F_2(x) = 2xF_1(x) \ . \tag{2.21}$$

This *scaling* behaviour is approximately true over a large range of Q^2 for high x. Going to lower x values, the gluons inside the proton play a more important role, quarks can radiate gluons etc. Some QCD corrections have therefore to be taken into account [9] and the structure function F_2 rises with increasing Q^2. Measurements of the inclusive NC and CC cross-sections are shown in Figure 2.3. Due to the dependence of the cross-section on the mass of the vector bosons, the CC cross-section is suppressed up to $Q^2 \sim 10^4\,\mathrm{GeV}^2$.

The difference between the electron and positron scattering cross-sections is related to the quark content of the proton. Electrons interact with up-type and positrons with down-type quarks in a charged-current reaction.

2.3.2. Factorisation and Parton Densities

When calculating lepton-hadron or hadron-hadron cross-sections, one has to deal with soft (long range) and hard (short range) interactions at the same time. In the concept of *factorisation* it has been shown theoretically that it is possible to separate the pQCD calculable hard process from the soft process in the interaction [10]. In this framework the proton structure function, F_2^p, has the form of a convolution of perturbatively calculable coefficient functions (Wilson coefficients), C_2^i, and parton density functions (PDFs)

$$F_2^p = \sum_{i=q,\bar{q},g}\int_x^1 d\xi C_2^i\left(\frac{x}{\xi},\frac{Q^2}{\mu_R^2},\frac{\mu_f^2}{\mu_R^2},\alpha_s(\mu_R^2)\right)f_i^p(\xi,\mu_f,\mu_R) \ . \tag{2.22}$$

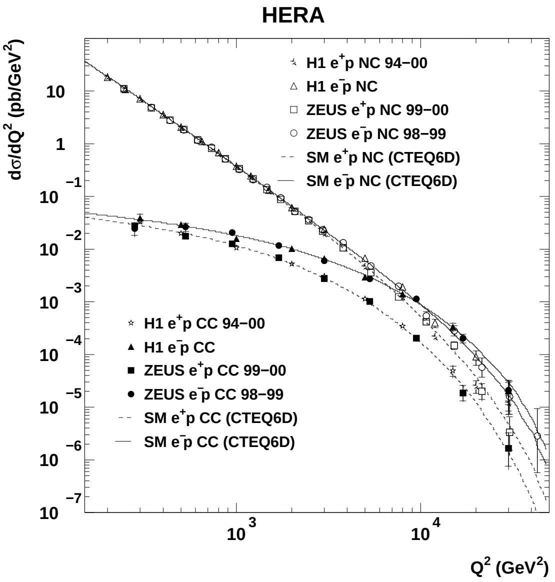

Figure 2.3: Inclusive differential NC and CC cross-section as a function of Q^2. Data points are measurements from ZEUS and H1, the lines show the SM predictions for the specific processes.

$f_i^p(\xi, \mu_f, \mu_R)$ gives the probability to find a parton, i, with momentum fraction, ξ, in the proton. It depends on the renormalisation scale, μ_R, and the factorisation scale, μ_f. μ_f is the value below which radiated soft gluons from the partons are included in the parton density functions according to a certain *factorisation scheme*. Using the structure function, (Equation 2.22), the inclusive *ep* cross-section can be separated into a parton-level cross-section, $\hat{\sigma}_{ei}$, and parton density functions, f_i^p:

$$\sigma_{ep} = \sum_{i=q,\bar{q},g} \hat{\sigma}_{ei}(\mu_F) \otimes f_i^p(\mu_F) \ . \tag{2.23}$$

The hard subprocess cross-section can be calculated in pQCD. The PDFs cannot be calculated from first principles and have to be extracted from experimental structure function data using *parton evolution equations*.

The underlying concept is universal, but in practice approximations have to be applied, resulting in different *parton evolution models* which make use of different ordering of the radiated gluons along the line connecting the parton and the hard scatter. The parton evolution model used in this thesis will be described next:

The DGLAP Equations

The Dokshitzer-Gribov-Lipatov-Altarelli-Parisi (DGLAP) [11] evolution equations describe the way in which the quark and gluon momentum distributions inside a hadron evolve in Q^2. The DGLAP equations are given by:

$$\frac{\mathrm{d}q_i(x,Q^2)}{\mathrm{d}\log Q^2} = \frac{\alpha_s(Q^2)}{2\pi}\int_x^1 \frac{\mathrm{d}y}{y}\left[\sum_i q_i(y,Q^2)P_{qq}\left(\frac{x}{y}\right) + g(y,Q^2)P_{qg}\left(\frac{x}{y}\right)\right] , \tag{2.24}$$

$$\frac{\mathrm{d}g(x,Q^2)}{\mathrm{d}\log Q^2} = \frac{\alpha_s(Q^2)}{2\pi}\int_x^1 \frac{\mathrm{d}y}{y}\left[\sum_i q_i(y,Q^2)P_{gq}\left(\frac{x}{y}\right) + g(y,Q^2)P_{gg}\left(\frac{x}{y}\right)\right] , \tag{2.25}$$

where $q_i(x,Q^2)$ is the quark density function for each quark flavour, i, and $g(x,Q^2)$ is the gluon density function. The Altarelli-Parisi splitting functions $P_{jk}\left(\frac{x}{y}\right)$ represent the probability of a parton, k, with momentum fraction, y, to emit a parton, j, of momentum fraction, x, in the interval $Q^2 \rightarrow Q^2 + \mathrm{d}\log Q^2$.
The DGLAP approach assumes that the dominant contribution to the evolution comes from successive parton emissions which are strongly ordered in transverse momentum, k_T, the largest of which corresponds to the parton interacting with the probe ($k^2_{T,1} \ll k^2_{T,2} \ll \ldots \ll k^2_{T,n} \ll Q^2$), as illustrated in Figure 2.4. This approach is often called collinear factorisation.

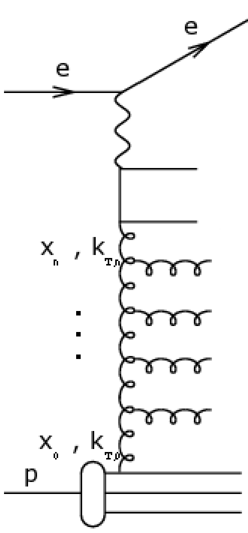

Figure 2.4: Diagram of the k_T evolution ladder. A quark from the proton interacts with a virtual photon from the electron after radiating n gluons. Each gluon is characterised by a longitudinal momentum fraction x_i and a transverse momentum $k_{T,i}$.

According to the factorisation theorem of QCD the PDFs are process independent, thus predictions can be made for processes other than the ones used for their determination. In Figure 2.5 the PDFs determined using NLO techniques for DIS data are shown. The u and d valence quarks carry only about 50% of the proton momentum and dominate at high x, while gluons and sea quarks dominate at low x.

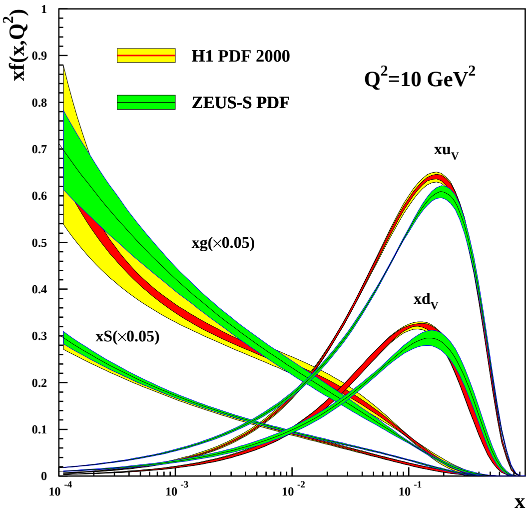

Figure 2.5: The gluon (xg), sea (xS), u and d valence distributions extracted from a ZEUS next-to-leading-order QCD fit at $Q^2 = 10\,\mathrm{GeV}^2$ [12]. Note the gluon and sea distributions are scaled by 0.05.

2.3.3. Photoproduction Processes and Photon Structure

In Equation 2.19 we have seen that the cross-section shows a $1/Q^4$ dependence due to the photon propagator. The dominant cross-section contribution will therefore come from photon exchange with very low virtuality. The average lifetime of the exchanged photon is $\sim E_\gamma/Q^2$, thus for photons of low virtuality this time can be long with respect to the time of the hard subprocess.

At HERA an electron scattered at very low angles can produce an almost real photon. Hence this kind of reaction can be regarded as a γp collision. The total photoproduction (PhP) cross-section, σ^{ep}_{tot}, can be separated into a photon-proton cross-section contribution and a flux factor $f_{e\to\gamma}(y)$, the probability to find a photon of energy $E_\gamma = yE_e$. For $Q^2 \to 0$ the photon longitudinal polarisation vanishes, hence the PhP cross-section can be written to a good approximation as:

$$\frac{d^2\sigma^{ep}}{dydQ^2} \sim f_{e\to\gamma_T}(y,Q^2)\sigma^{\gamma P}_{tot}(y,Q^2)\ , \qquad (2.26)$$

where the transverse photon flux $f_{e\to\gamma_T}(y,Q^2)$ is given by:

$$f_{e\to\gamma_T}(y,Q^2) = \frac{\alpha}{2\pi}\frac{1}{Q^2}\left(\frac{1+(1-y)^2}{y} - 2\frac{1-y}{y}\frac{Q^2_{min}}{Q^2}\right)\ , \qquad (2.27)$$

and Q^2_{min} represents the lower kinematic limit given by

$$Q^2_{min} = m_e^2y^2/(1-y)\ . \qquad (2.28)$$

This is known as the equivalent photon approximation (EPA).

Neglecting the Q^2 dependence of the γp cross-section and integrating over the photon virtuality from Q^2_{min} up to an upper kinematic limit Q^2_{max}, one obtains:

$$f^{WWA}_{e\to\gamma T}(y) = \frac{\alpha}{2\pi}\left(\frac{1+(1-y)^2}{y} - 2\frac{1-y}{y}\ln\frac{Q^2_{max}}{Q^2_{min}} - 2\frac{1-y}{y}\left(1-\frac{Q^2_{min}}{Q^2_{max}}\right)\right) , \quad (2.29)$$

which is known as the Weizsäcker-Williams approximation (WWA) [13, 14].

Despite its classification in the Standard Model as an elementary, colour-neutral particle, the photon can fluctuate into $q\bar{q}$ pairs. The lifetime of these fluctuations increases with decreasing Q^2. Thus the photon can act as a source of partons, and it is possible to use the same formalism as for hadron-hadron scattering and to introduce a *photon structure function*. The main experimental input to the photon structure function comes from $\gamma\gamma$ processes in e^+e^- scattering. In the case of one quasi-real and one virtual photon the interaction can be treated as deep inelastic $e\gamma$ scattering with the virtual photon probing the hadronic structure of the quasi-real photon. In analogy to the proton case, photon structure functions can be measured and parton density functions, f_i^γ, can be extracted using parton evolution equations.

Direct Photoproduction

In direct photoproduction, the photon behaves as a point-like object interacting with the partons in the proton; it participates *directly* in the hard subprocess. In contrast to hadronic reactions all the photon energy is available in the interaction with the parton. The final state should therefore have on average a higher transverse momentum in direct photoproduction than in reactions where only part of the photon momentum is involved.

The dominant LO direct processes at HERA are QCD Compton scattering and boson-gluon fusion. Lowest order Feynman graphs are shown in Figure 2.6. The processes look similar to the ones in DIS, but the hard scale can not be set by Q^2, because the photon is quasi-real. Instead a hard scale can be set by the internal propagator, producing e.g. jets with high transverse energy, E_T^{jet}.

Resolved Photoproduction

In resolved photoproduction, the photon acts as a source of partons with one of them interacting with a parton in the proton. Examples of leading-order processes are shown in Figure 2.7. In this example a gluon from the photon interacts with a gluon from the proton (gluon-gluon fusion), another possibility is a quark from the photon interacting with a gluon from the proton (photon excitation). In resolved photoproduction the fragmentation products from the photon are also present in the event, which distinguishes it from direct PhP.

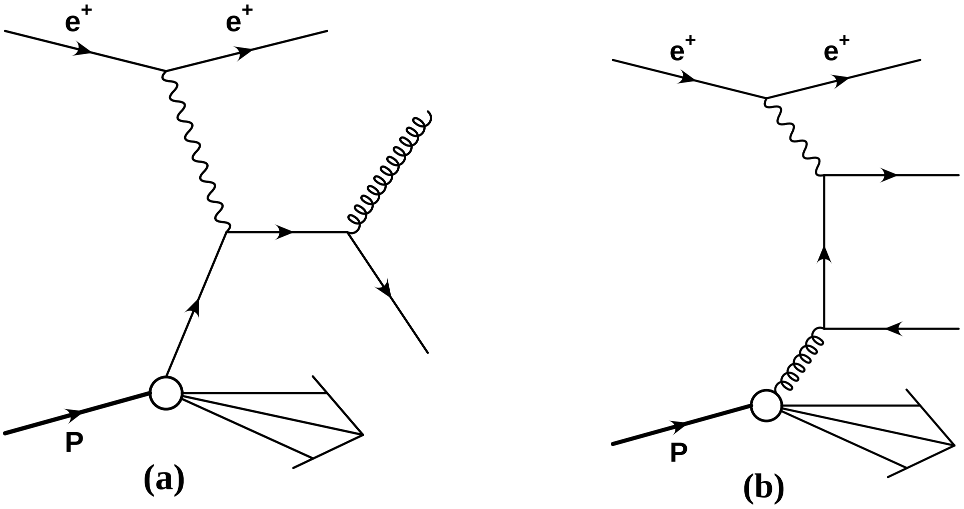

Figure 2.6: Examples for LO direct dijet photoproduction, a) QCD Compton scattering, b) boson-gluon fusion.

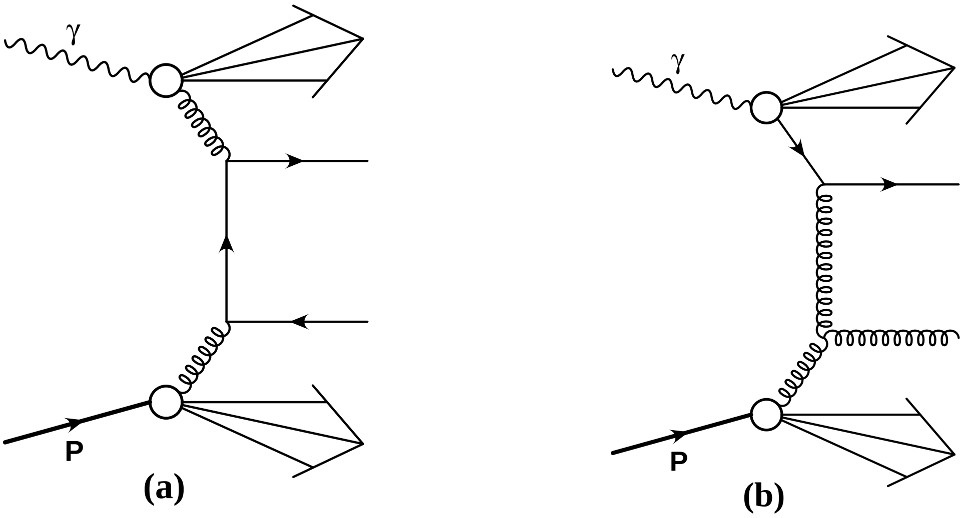

Figure 2.7: Examples for LO resolved dijet photoproduction, a) gluon-gluon fusion, b) excitation in the photon.

Photoproduction Generalised Model

The differential hard photoproduction cross-section can be written as the sum of the direct and resolved components:

$$d\sigma_{\gamma P}(p_\gamma, p_P) = d\sigma_{\gamma P}^{direct}(p_\gamma, p_P) + d\sigma_{\gamma P}^{resolved}(p_\gamma, p_P) \ . \tag{2.30}$$

Using the QCD factorisation theorems the soft and the hard parts of the cross-section can be separated leading to:

$$\begin{aligned} d\sigma_{\gamma P}^{\text{direct}}(p_\gamma, p_P) &= \sum_i \int dx f_{i/P}(x, \mu_F) \cdot \\ &\qquad d\sigma_\gamma(p_\gamma, xp_P, \alpha_s(\mu_R), \mu_R, \mu_F, \mu_\gamma) \ , \end{aligned} \tag{2.31}$$

$$\begin{aligned} d\sigma_{\gamma P}^{\text{resolved}}(p_\gamma, p_P) &= \sum_{ij} \int dx dx_\gamma f_{j/\gamma}(x_\gamma, \mu_\gamma) f_{i/P}(x, \mu'_F) \cdot \\ &\qquad d\sigma_{ij}(x_\gamma p_\gamma, xp_P, \alpha_s(\mu'_R), \mu'_R, \mu'_F, \mu_\gamma) \ . \end{aligned} \tag{2.32}$$

$d\sigma_\gamma$ and $d\sigma_{ij}$ represent the elementary 2 → 2 cross-sections of the hard sub-processes, $f_{i/P}$ and $f_{j/\gamma}$ give the probability to find a parton i and j with momentum fraction x and x_γ of the proton and the photon, respectively, in the scattering process. The renormalisation scales μ_R, μ'_R of the strong coupling constant, α_s, are set proportional to the transverse momentum, $\hat{p_t}$, of the final state partons (or their masses). Since α_s has to be small for reliable predictions, the parton transverse momentum (or its mass) has to be above some minimum value, usually taken to be about 2 GeV. A sketch of the general scheme for the factorisation of the photoproduction process is given in Figure 2.8

The factorisation scales μ_F, μ'_F and μ_γ separate the hard scatter from the soft long-range interactions in the photon and the proton. They are usually set equal to the renormalisation scale.

The distinction between direct and resolved processes is only possible at leading order and depends on the factorisation scale of the photon, μ_γ, as shown in Figure 2.9. Beyond leading order there is an interplay between the direct and resolved component. The divergences arising from collinear emission of quarks from the incoming direct photon are re-absorbed into the parton densities in the photon appearing in the resolved component. Thus only the sum of the direct and resolved components has a physical meaning.

The elementary cross-sections of the hard subprocess are the only components that are “pure” perturbative QCD predictions. The observable inclusive cross-sections rely on all the input distributions mentioned above, as well as on the factorisation of the different input distributions. Therefore comparisons of data with such calculations also give information on the input distributions.

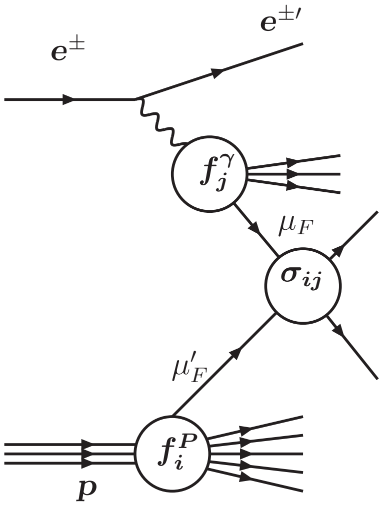

Figure 2.8: General scheme for the factorisation of the photoproduction process into a hard sub-process, denoted by σ_{ij}, calculable with perturbative QCD, and soft processes hidden in the parton distributions of the photon and the proton. The factorisation scales μ_F, μ'_F separate the short–distance hard scatter from the parton distributions. Only leading order is shown.

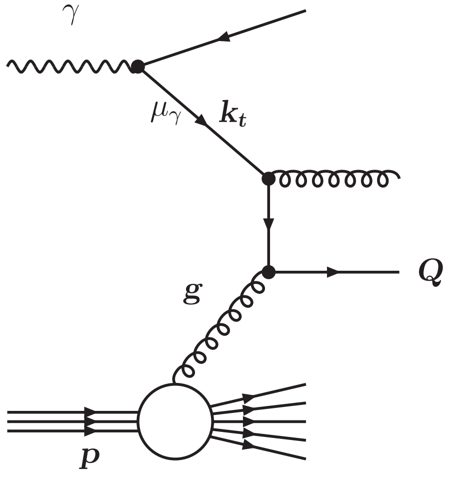

Figure 2.9: Ambiguity of direct and resolved classification in γp interactions. If the virtuality k_t of the parton propagator is lower than the factorisation scale μ_γ, the splitting process is included in the photon structure of the resolved calculation at *leading* order; while it is regarded as a direct process at *next-to-leading order*.

2.3.4. Parton Hadronisation

As no colour is observed directly in nature, the quarks of the hard subprocess have to form bound states directly after their production. This can be described as a series of different steps. In a first perturbative step, additional partons are emitted from the initial state parton(s) or the partons of the hard subprocess known as the *parton shower*, followed by a second non-perturbative step using phenomenological models to form hadrons from these partons (*hadronisation*).

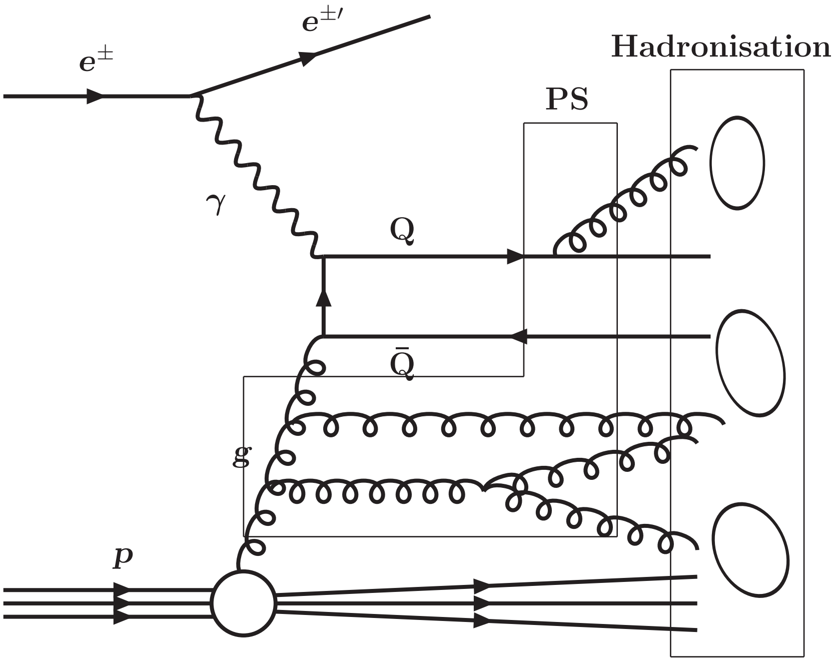

Figure 2.10: Parton evolution in direct photoproduction: parton showers (PS), formation of hadrons (Hadronisation).

Parton Showers (PS)

The model of parton showers, or *parton cascades*, approximates multiple parton emissions by a series of successive parton splittings, as illustrated in Figure 2.10. The probability that a parton is emitted from a parent parton with a given virtuality is taken from the corresponding *splitting functions* [11], which are part of the evolution equations described in Equation 2.25.

Initial-state and final-state parton showers have to be considered in a different manner. The initial-state parton shower starts from a parton coming from the proton which continues to emit partons with increasing virtuality until it enters the hard scatter, while for the outgoing partons the virtuality is negative and the emissions are stopped when reaching a minimal value necessary for perturbative calculations. This infrared cut-off value lies typically around 1 GeV^2.

Hadronisation

The transition from the final-state partons into bound hadrons cannot be calculated perturbatively. Therefore phenomenological methods have to be applied to describe the hadronic final state produced by a certain final state parton configuration.

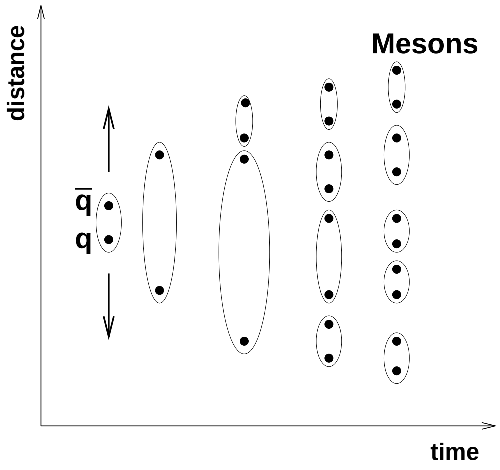

Figure 2.11: Illustration of the string fragmentation. $q\bar{q}$ pairs and the colour fields between them form uniform colour flux tubes (strings). If the potential energy is high enough, it breaks into two pieces forming new $q\bar{q}$ until the energy is not enough to produce new $q\bar{q}$ pairs.

The model used for the fragmentation in the MC generators of this thesis uses *string fragmentation* [15]. As shown in Figure 2.11, the $q\bar{q}$ pairs are connected by colour flux tubes, called strings. The string has a uniform energy per unit length, corresponding to a linear quark confining potential. Therefore the potential rises with increasing distance. If the potential energy is high enough, the string breaks up and new $q\bar{q}$ pairs are formed. This process continues as long as the invariant mass of the string pieces exceeds the on-shell mass of a hadron.

The hadron-level cross-section ($\sigma(ep \rightarrow eh(k)X)$) of the final-state partons is connected to the parton-level cross-section through the factorisation theorem. It can be expressed by the following equation [16]:

$$\frac{d^3\sigma_h(k)}{d^3k} = \int D(z) \, \frac{d^3\sigma_q(\hat{k})}{d^3\hat{k}} \, \delta^3(\vec{k} - z\vec{\hat{k}}) \, d^3\hat{k} \, dz \ , \tag{2.33}$$

where h is the hadron with momentum k, $\hat{k}$ is the momentum of the quark and σ_q is the parton-level cross-section. z is the momentum fraction of the parton carried by the hadron and $D(z)$ is the non-perturbative fragmentation function, which is not calculable, but assumed to be universal. A commonly used fragmentation function for heavy-flavour production is the *Peterson fragmentation function* [17], which has the form:

$$D_{h/i}(z) = P_{h/i} \cdot \frac{\mathcal{A}}{z \cdot \left(1 - \frac{1}{z} - \frac{\epsilon}{1-z}\right)^2} \ , \tag{2.34}$$

where $D_{h/i}(z)$ denotes the fragmentation of a final-state parton, i, into a hadron, h. $\mathcal{A}$ is a normalisation constant and $\mathcal{P}_{h/i}$ the total probability for the quark, i, to fragment to h. ϵ is a free parameter which depends on the order of the perturbative expansion and is expected to scale with the quark mass: $\epsilon \propto 1/m_{\mathrm{Q}}^2$. For beauty-quark production it has been determined to $\epsilon_b \approx 0.0035$[18], but the exact value depends on the chosen parton showering scheme.

Another fragmentation function is the *LUND symmetric fragmentation function* [19]

$$D_{h/i}(z) = P_{h/i} \cdot \frac{\mathcal{A}}{z}(1-z)^a \, e^{-bm_{t,h}^2/z} \ , \tag{2.35}$$

with $m_{t,h}$ denoting the transverse mass of the hadron in question. This fragmentation function is often used for the fragmentation of light-flavour quarks. The parameters a and b are usually chosen to be 0.3 and $0.58\,\mathrm{GeV}^{-2}$ respectively.

For the calculation of the theoretical uncertainty of the next-to-leading-order predictions the *Kartvelishvili parametrisation* [20] is used as an alternative to the Peterson fragmentation function:

$$D(z) = P_{h/i} \cdot \mathcal{A}\, z^{\alpha}(1-z) \ , \tag{2.36}$$

where α is the variable parameter.

2.4. Beauty Production and Decay

Beauty, together with charm and top quarks, are often referred to as *heavy quarks* as their mass is much higher than Λ_{QCD} as well as the mass of the other three quarks (u, d, s) which are therefore called *light quarks.* The high mass of the heavy quarks provides a hard scale and α_s is sufficiently small to allow perturbative calculations. Hence, heavy quark production is an excellent testing ground for pQCD. Even after many years of study, some small inconsistencies are still present. Especially the data from beauty tends sometimes to lie above the NLO QCD predictions. This may be due to different hard scales in the process, e.g. the p_T of the outcoming parton can present a second hard scale, or the photon virtuality, Q^2, which complicates the calculations. A second uncertainty can be the fragmentation and hadronisation processes necessary to compare the heavy-quark calculations with experimental data. The relevant methods for the production and decay of beauty quarks are described in the following.

The theoretical description of heavy-quark production and decay can be separated into several parts. At first the parton-level cross-section of beauty production is calculated at a scale close to the beauty mass. In a second step the beauty quark couples with a quark from the fragmentation process to build an on-mass-shell hadron. In a following step the heavy meson or baryon decays according to experimentally determined branching ratios.

2.4.1. Beauty Production

In leading order ($O(\alpha\alpha_s)$) the main contribution to beauty production at an *ep* collider comes from boson-gluon fusion (BGF), as shown in Figure 2.6a. The BGF cross-section can be calculated as

$$\sigma_{\mathrm{BGF}} = \frac{\pi e_b^2 \alpha \alpha_s}{\hat{s}} \left\{ (2 + 2\omega - \omega^2) \ln \frac{1+\chi}{1-\chi} - 2\chi(1-\chi) \right\} \ , \tag{2.37}$$

where $\hat{s} = (p_b + p_{\bar{b}})^2$ is the squared centre-of mass energy of the $b\bar{b}$ pair and e_b is the electromagnetic charge of the beauty quark [24]. The variables ω and χ are given by $\omega = 4m_b^2/\hat{s}$ and $\chi = \sqrt{1-\omega}$. The cross-section for charm can be obtained exchanging the charge and the mass. The lower mass and the higher charge lead to a much higher cross-section and hence to a strong suppression of the beauty cross-section.

Beauty production has also been calculated at NLO level, as the contribution for beauty is significant [21]. Compared to leading-order calculations, the main difference is the additional radiation of hard gluons and the interference with virtual corrections. Some examples of these processes are given in Figures 2.12 and 2.13. This means that part of the parton showering in leading order becomes now part of the hard scatter in NLO, see Figure 2.14.

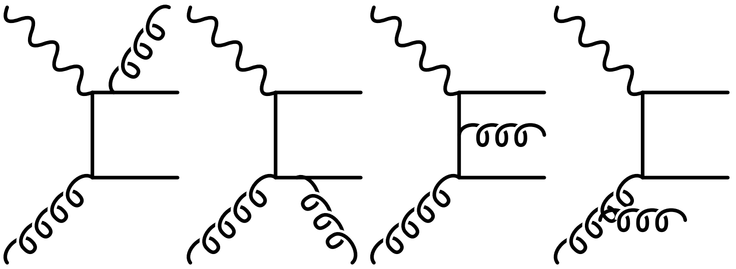

Figure 2.12: Examples of NLO contributions to the beauty cross-section from additional gluon radiation.

2.4.2. Beauty Fragmentation

A simple but successful way to describe the transformation from beauty and charm quarks to hadrons is via the Peterson fragmentation function, given in Equation 2.34. The value of ϵ_q has to be determined experimentally. Typical values for charm and

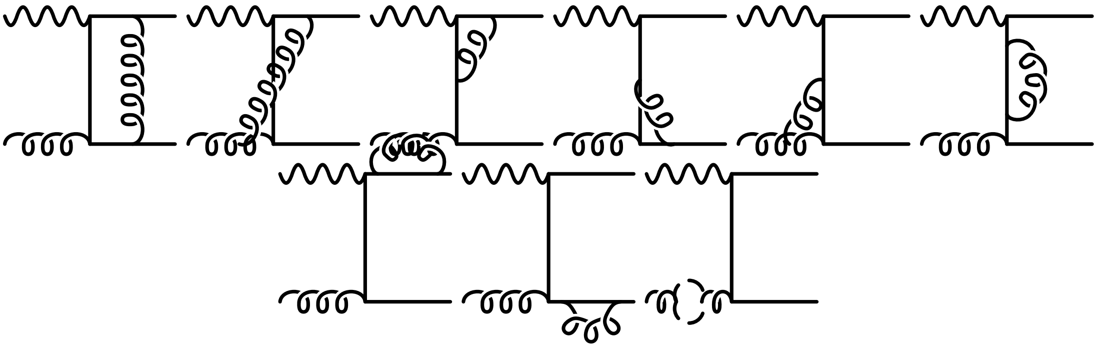

Figure 2.13: Examples of NLO contributions to the beauty cross-section from virtual corrections.

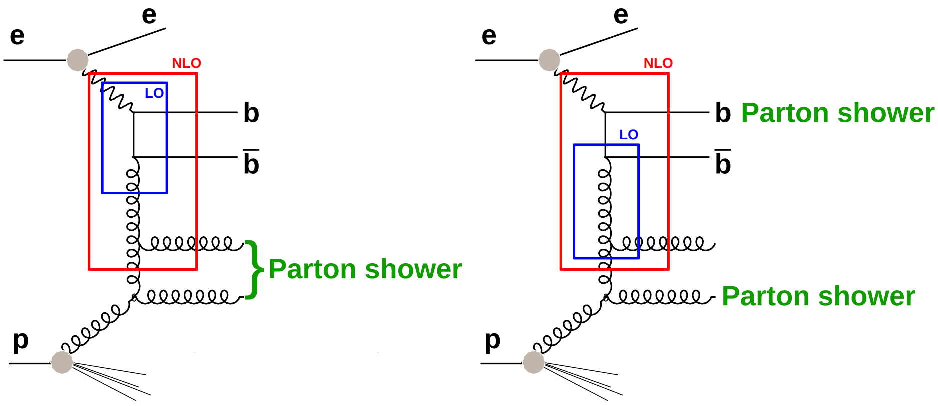

Figure 2.14: LO, NLO and PS in $b\bar{b}$ production. A part of the parton shower applied to initial and final state partons in LO is part of the hard scatter in NLO.

beauty are $\epsilon_c = 0.035$ and $\epsilon_b = 0.0035$ [18]. In Figure 2.15 the shape of the functions are compared. The B-hadrons, containing beauty are generated with a harder spectrum than the hadrons, containing charm. The most frequent weakly-decaying heavy-flavour hadrons and their properties are summarised in Table 2.2.

2.4.3. Semi-Leptonic Beauty Decay

Due to their short lifetime B-hadrons cannot be detected directly. Their decay products are needed to identify them. The simplest model to describe hadron decays is given by the *spectator model*. As shown in Figure 2.16 the beauty quark decays weakly into a charm quark and a W-boson, which subsequently decays into a muon and a neutrino. In this picture the spectator up quark does not take part in the reaction. The high mass of the beauty quark leads to a suppression of QCD effects like gluon radiation and binding effects which justify the assumption of the model to neglect QCD effects.

Beauty quarks decay predominantly via an intermediate charm quark, as the transition probability is proportional to $|V_{cb}|$ which is one order of magnitude larger than the probability for the process $b \to u$ given by $|V_{ub}|$. The W-boson subsequently

Hadron	Quark Content	Mass [MeV]	$c\tau$ [μm]	$I(J^P)$
B^+	$\bar{b}u$	5279.0 ± 0.5	501	$\frac{1}{2}(0^-)$
B^0	$\bar{b}d,$	5279.4 ± 0.5	460	$\frac{1}{2}(0^-)$
B_s^0	$\bar{b}s$	5369.6 ± 2.4	438	$0(0^-)$
Λ_b	udb	5624 ± 9	368	$0(\frac{1}{2}^+)$
D^+	$c\bar{d}$	1869.4 ± 0.5	311.8	$\frac{1}{2}(0^-)$
D^0	$c\bar{u}$	1864.6 ± 0.5	123.0	$\frac{1}{2}(0^-)$
D_s^+	$c\bar{s}$	1968.3 ± 0.5	147.0	$0(0^-)$
Λ_c^+	cud	2284.9 ± 0.6	59.9	$0(\frac{1}{2}^+)$

Table 2.2: Properties of the most frequently produced beauty hadrons. The former have both a higher mass and a longer lifetime. The higher mass is given by the b quark mass whereas the longer lifetime results mainly from the smaller CKM matrix element $|V_{cb}| = 0.04$ compared with $|V_{cs}| = 0.97$ [4]. The corresponding antiparticle can be obtained by replacing each quark by its antiquark and vicecversa.

decays to a muon and a neutrino with a probability of [4]

$$Br(W \to \mu\nu) = 10.68 \pm 0.12\% \ . \tag{2.38}$$

2.5. Monte Carlo Event Generators

In this thesis a (LO+PS) Monte Carlo is used to determine the efficiencies and acceptances for the cross-section determination and the measurement is compared to results from leading order plus parton shower (LO+PS) event generators. LO+PS event generators make use of Monte Carlo techniques. For a general introduction see e.g. [22]. The results from this thesis are compared to the LO+PS event generator PYTHIA [23]. In the following the main methods used within PYTHIA are discussed.

To generate final-state hadrons all LO+PS event generators use the same scheme, shown explicitly for a BGF event in Figure 2.17. Perturbative matrix elements (ME) are calculated for the hard scatter at leading order. Renormalisation and factorisation scales are both set to the average transverse mass of the outgoing partons given by

$$\mu = \frac{1}{2}\sqrt{m_1^2 + p_{t,1}^2 + m_2^2 + p_{t,2}^2} \ . \tag{2.39}$$

As for BGF events, the heavy quark mass is taken into account, the cross-section stays finite for $p_t^b \to 0$ and the beauty sample can be generated inclusively. In order to take care of higher order effects additional partons are produced in the parton showering process using the DGLAP equations described in Section 2.3.4. For the fragmentation process, PYTHIA uses the LUND string fragmentation scheme described in

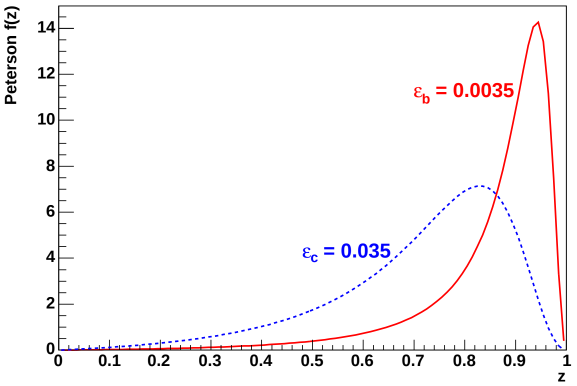

Figure 2.15: Comparison of the shape of the Peterson fragmentation function for typical charm and beauty values of ϵ_q. The curves are normalised to the same area.

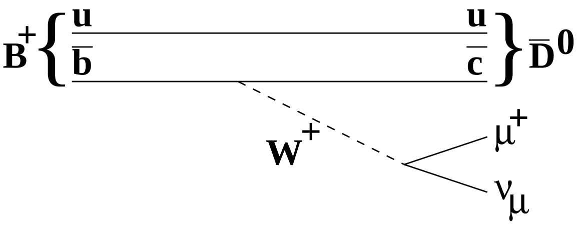

Figure 2.16: Hadron decay $B^+ \to \mu^+ \nu_\mu \bar{D}^0$ in the spectator model.

Section 2.3.4 using the Peterson fragmentation function for the longitudinal component of the $q\bar{q}$ momenta for heavy flavours and the LUND symmetric fragmentation function for light flavours, see Equation 2.35. The transverse momenta of the generated $q\bar{q}$ pairs are Gaussian distributed. The following decay of the unstable hadrons is carried out using experimentally measured decay spectra and probabilities. The decay spectra and branching ratios are general properties of the B-hadrons and therefore not specific to a certain experiment. In Figure 2.18(a) decay spectra measured at Belle [25] and BaBar [26] are compared to PYTHIA and good agreement is seen. In Figure 2.18(b) the momentum spectra of electrons and muons from B meson decays in different production environments are compared, and found to be very similar. The decay spectra of the B-hadrons are hence independent of the centre-of-mass energy and the final-state hadron mixture. It can therefore be assumed that also for HERA, PYTHIA gives a good description of the decay spectra.

The main production processes implemented in PYTHIA are direct, resolved, and excitation from the proton and photon, explained in the following:

- **Direct:** This is the pure BGF process, where the photon interacts directly with a gluon from the proton, see Figure 2.6b.

- **Resolved:** Here the photon has a hadronic substructure and emits a gluon or quark taking part in the calculation of the LO matrix element, see Figure 2.7.

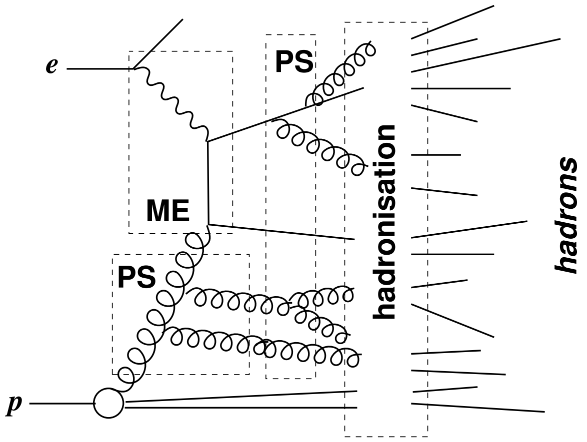

Figure 2.17: Structure of an *ep* event generator in a BGF process. The matrix element of the hard subprocess (ME) is calculated at leading order. Parton showers (PS) are applied for initial and final state radiation and finally the outgoing partons are transformed into hadrons in the hadronisation process. In the end the hadrons decay according to experimentally determined decay probabilities and spectra. From [24].

- **Excitation from the photon/proton:** This is a resolved process, where either the photon or the proton emits a heavy quark, which enters the hard scatter.

After the physics simulation, the final state hadrons have to pass the simulation of the ZEUS detector response. This is realised in a program called Mozart[3] which is based on GEANT [28]. After these steps the simulated events can be compared directly to the data distributions.

2.6. Next-to-Leading-Order Predictions

In heavy-flavour production up to NLO, two main schemes have been proposed. In the *fixed-flavour scheme*, also referred to as the *massive scheme* in the case of charm and beauty, the photon and proton have a hadronic substructure with only the three light quarks as active flavours. Heavy quarks are then produced in a hard scattering subprocess, where the heavy quark is assigned a realistic mass. In the so-called *massless scheme*, the heavy flavours are treated as active flavours in the photon and proton, the so-called excitation processes and the mass of the heavy quarks is set to zero. The optimal scheme for NLO QCD predictions depends on the dominant scale. If the virtuality, Q^2, and the transverse momentum of the heavy quark squared, $(p_T^{hq})^2$, are of the order of the m_{hq}^2, threshold effects due to the heavy quark mass have to be taken into account and the so called massive scheme should be used. If Q^2 or $(p_T^{hq})^2$

---

[3] Monte Carlo for ZEUS Analysis Reconstruction and Tracking.

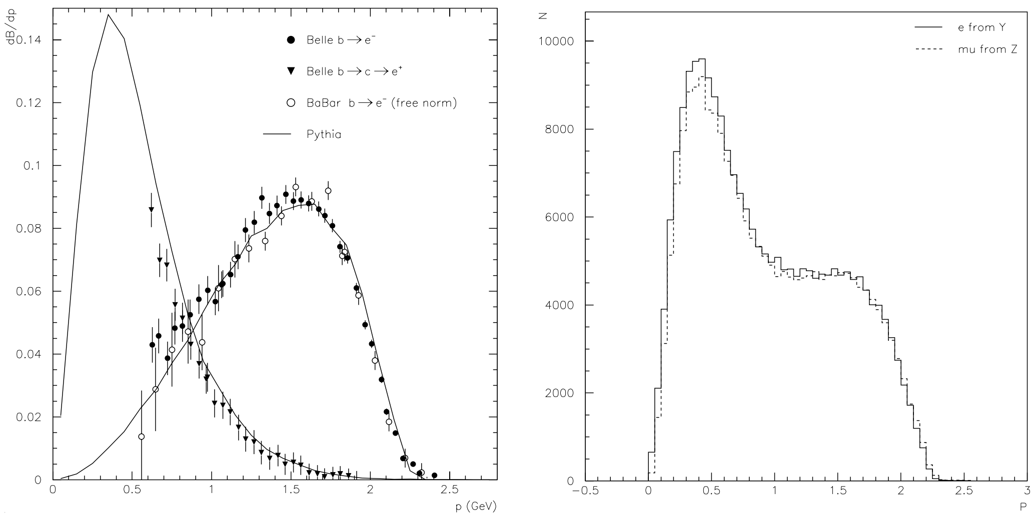

(a) (b)

Figure 2.18: B-hadron momentum spectra: (a) the differential branching ratio dB/dp, of the B hadron with respect to the electron momentum in the B centre-of-mass system measured by Belle and Babar are compared to the PYTHIA prediction (line), separately for direct (circles) and cascade (triangles) processes. (b) the PYTHIA prediction for the electron momentum distribution of the B-hadron mixture at the $\Upsilon(4S)$ resonance (BaBar/Belle centre-of-mass energies) are compared to the B-hadron mixture at LEP centre-of-mass energies. From [27].

are much larger than m^2_{hq}, the massless scheme should be used, as the excitation processes may become important at high energies.

In this thesis NLO calculations in the massive scheme are used. The program used for the NLO predictions in this thesis is FMNR [29]. Soft and collinear divergencies are treated by generating sequences of correlated events, such that cancellation of the sequences occurs. This method [30] removes the need for artificial regularisation, required when a light quark accompanies the heavy quark pair. The scale used was set to

$$\mu = \sqrt{(p_t^b)^2 + m_b^2}\ . \tag{2.40}$$

The parameters used in FMNR for the NLO predictions in this thesis are summarised in Table 9.1. The central values and their variation are given. The factorisation scales and renormalisation scales were varied at the same time and are the main contribution to the uncertainty of the NLO calculation. All other variations lead to cross-section changes at the few percent level. To produce final state muons from the b quarks the following procedure is used. First the b quarks fragment into B hadrons, which then decay into muons using the muon momentum decay spectra used within PYTHIA. The muons are emitted isotropically in the B hadron rest frame.

3. Beauty Production - Experimental Context

3.1. Heavy-Flavour Production in Fixed-Target Experiments

The measurement of $b\bar{b}$ production is a longstanding and important project in the framework of the Standard Model. After the discovery of the Υ resonance in a fixed target experiment, in 1977 the beauty-quark cross-section was measured at different centre-of-mass energies [31]. The focus shifted to production of B-mesons. Figure 3.1 shows some results for the total cross-section from fixed target experiments. The results are in good agreement with QCD next-to-leading-order predictions. The bands around the central value of the prediction represent the uncertainty of the prediction.

3.2. Beauty Production at the $Sp\bar{p}S$

The UA1 collaboration was the first to measure beauty-quark cross-sections in single muon and dimuon events in $p\bar{p}$ collisions [34]. Beauty was identified at the $Sp\bar{p}S$ collider at CERN at a centre-of-mass energy of 630 GeV using the semi-leptonic decay into muons. Muons were required to have a transverse momentum, p_T^μ, of 6 GeV in the single muon case and of 3 GeV in the dimuon analysis.

The measured inclusive single beauty-quark cross-section in an η range[1] of $|\eta| < 1.5$ as well as the differential cross-sections from single muon and dimuon event data is compared to next-to-leading-order predictions and found to be in good agreement, see Figure 3.2 [35].

The importance of higher order contributions to the cross-sections can be observed by measuring the $b\bar{b}$ correlations in $\Delta R_{b\bar{b}} = \sqrt{\Delta\eta^2_{b\bar{b}} + \Delta\phi^2_{b\bar{b}}}$ and $\Delta\phi_{b\bar{b}}$, where $\Delta\phi_{b\bar{b}}$ is the azimuthal angle between the b and the $\bar{b}$ quark. Figure 3.3 shows measurements of the higher p_T beauty quark, in two different transverse momentum ranges $p_{Tb}^{max} > 6(11)$ GeV. In leading order the configuration should be back-to-back ($\Delta\phi_{b\bar{b}} = 180°$), while higher order contributions can lead to lower angles between

---

[1] η is the so-called pseudo-rapidity and defined as $\eta = -\ln\tan(\theta/2)$. Differences in η are Lorentz invariant, and the multiplicity distribution is approximately flat in η, hence pseudo-rapidity is often used instead of θ at hadron colliders.

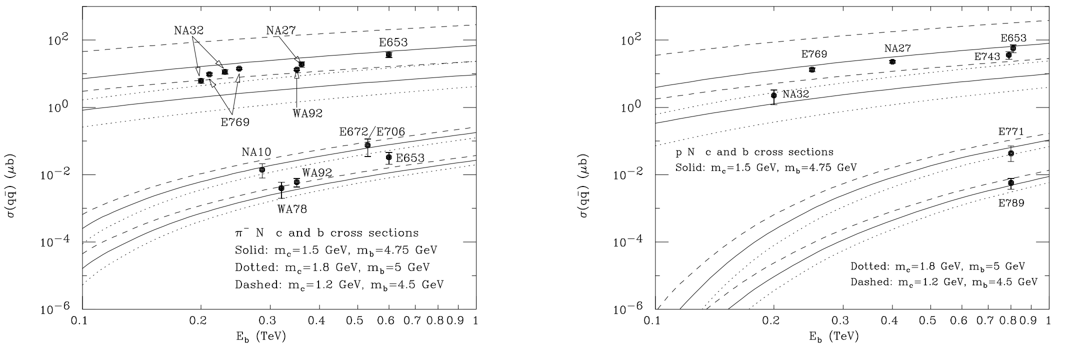

(a) Beauty (lower curves) and charm (upper curves) production in $\pi^- N$ collisions as a function of the beam energy.

(b) Beauty charm production in pN collisions.

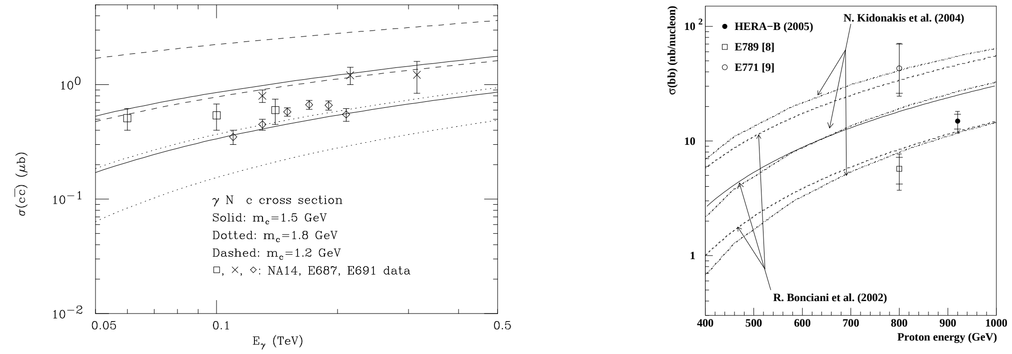

(c) Charm production in γN collisions.

(d) Beauty production in pN collisions.

Figure 3.1: Total cross-sections for beauty and charm production in hadron production and photoproduction observed in fixed-target experiments. The data is in good agreement with the shown NLO QCD predictions. From [32] and [33].

the beauty quarks. The measurements agree well with the NLO predictions and demonstrate the importance of higher order contributions.

3.3. Beauty Production at the Tevatron

Beauty production has also been studied in $p\bar{p}$ collisions at the Tevatron, at a centre-of-mass energy of 1.8 TeV (Run I) and at 1.96 TeV (Run II). The CDF and D0 experiments published early measurements of beauty-quark cross-sections reporting a difference in normalisation between the measurement and the data by a factor of two from CDF and agreement between data and NLO from DO. Further measurements from DO of the Run I data, confirmed the discrepancy seen by CDF [36].

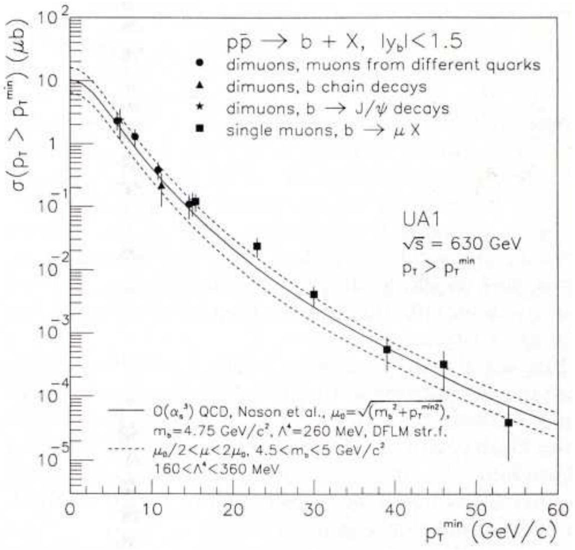

Figure 3.2: Inclusive single beauty-quark cross-section from UA1. Presented are the results extracted from single muon and dimuon events in a range of $|\eta| < 1.5$ and $p_T^\mu > 6\,\text{GeV}$ (single muon) and $p_T^\mu > 3\,\text{GeV}$ (dimuon). The measurements are compared to next-to-leading-order predictions.

Over the last years this long standing difference has been reduced by refining the experimental and theoretical methods. For a review see e.g. [37]. The recent measurements of the total B-hadron production rates at $\sqrt{s} = 1.96\,\text{TeV}$ are in good agreement with NLO QCD. The residual discrepancies are well within the uncertainties. Figure 3.4 shows the results on open beauty production at the Tevatron before and after the experimental and theoretical improvements.

Dijet correlations were measured recently in $\Delta\phi$ of the two tagged beauty jets [38]. The jets were required to have a minimum E_T of 20 GeV and were measured in the central region of the detector, $|\eta| < 1.2$. Beauty tagging was performed using lifetime information. Cross-sections were measured as a function of E_T of the leading jet, the invariant mass of the beauty tagged jets and the azimuthal angle between the two jets. The results were compared to leading order Monte Carlos (PYTHIA and HERWIG) as well as MC@NLO. All measured cross-sections are in good agreement with the next-to-leading-order Monte Carlo. The differential cross-sections as a function of E_T and $\Delta\phi$ are shown in Figure 3.5.

3.4. Heavy-Flavour Production at HERA

The nature of ep collisions should simplify the difficulties for the theory to predict cross-sections. Only one of the incoming particles is a proton with a partonic substructure, while the other is a point-like electron or positron, which is well understood theoretically. However the exchanged photon can have a hadronic structure which

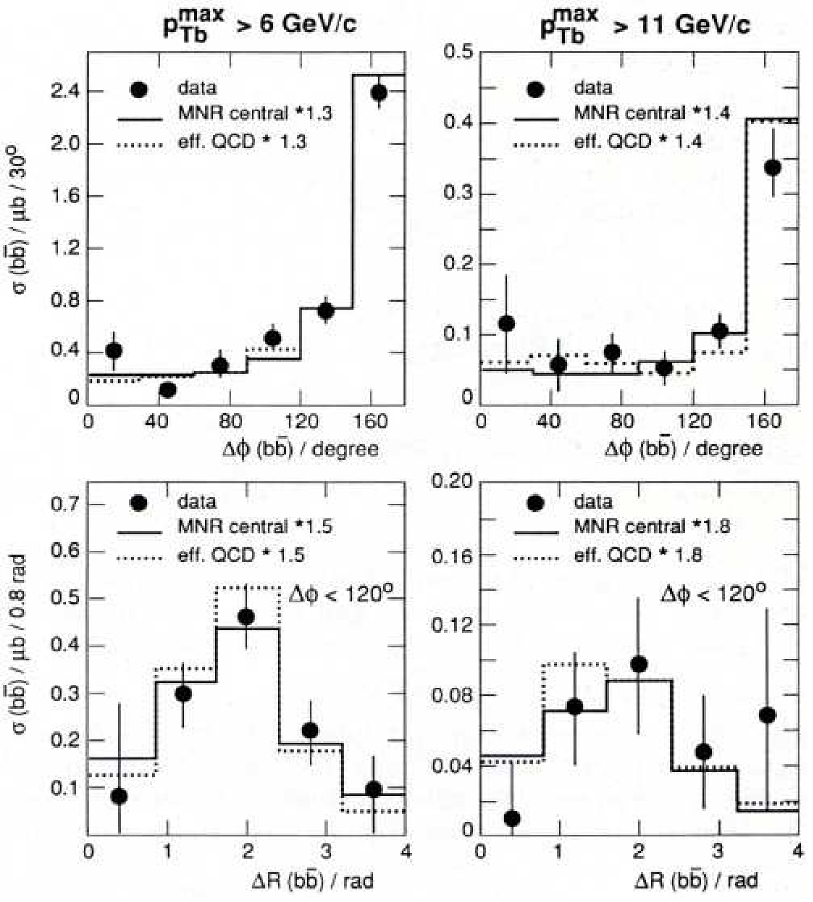

Figure 3.3: Beauty-quark correlation measurements from dimuon events in $\Delta\phi_{b\bar{b}}$ (upper plots) and $\Delta R_{b\bar{b}}$ (lower plots) in two different ranges of the beauty quark higher transverse momentum $p_{Tb}^{max} > 6(11)$ GeV. The measurements are compared to next-to-leading-order predictions.

complicates calculations again. In practice the theoretical treatment of *ep* collisions is almost as complicated as the calculations for pp or $p\bar{p}$ collisions. In the following a selection of the latest beauty-quark cross-section measurements is given followed by results on dijet correlation measurements in charm.

3.4.1. Beauty Production

The previous ZEUS analysis on beauty photoproduction in the semi-leptonic muon decay channel using data taken between 1996 and 2000 data required a muon of $p_T > 2.5$ GeV reconstructed in the muon chambers and two jets of $p_T > 7(6)$ GeV [39]. Beauty was separated from charm and light flavour in a two parameter fit of the transverse momentum of the muon relative to the jet, p_T^{rel}. The cross-section was measured as a function of p_T of the muon, η of the muon, p_T of the jet, η of the jet and x_γ, see Figures 3.6 - 3.8. The measured cross-sections agree well in shape

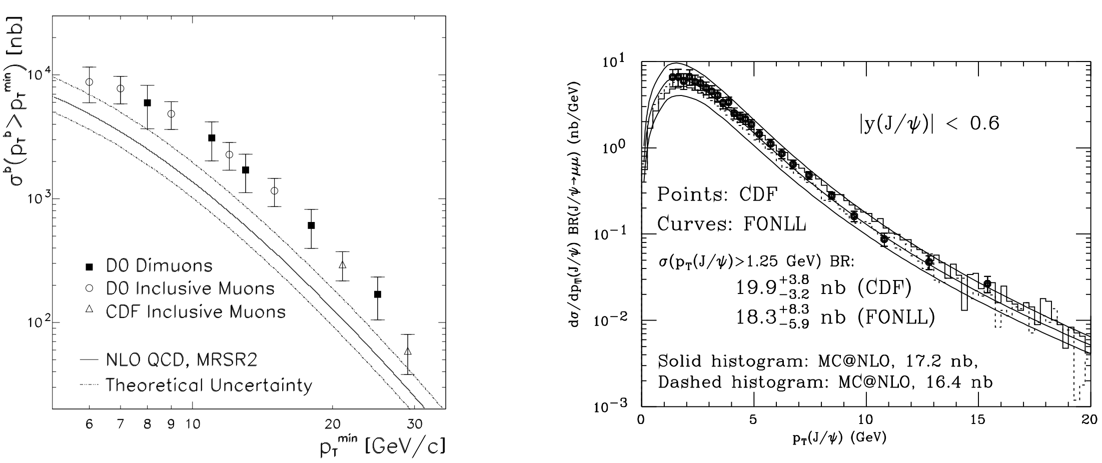

(a) Run I

(b) Run II

Figure 3.4: Open beauty production in $p\bar{p}$ collisions at the Tevatron. In (a) older measurements from the CDF and D0 collaborations are shown. The beauty contribution was determined with the help of muons coming from semi–leptonic B decays. The beauty production cross-sections, shown as function of the transverse b-quark momenta, p_T^b, differ a lot from a QCD next-to-leading-order prediction also shown. The situation is much improved in (b). Here, results of an analysis of J/ψ mesons originating from B decays in Tevatron Run II data are shown with improved NLO calculations, and MC@NLO, a next-to-leading-order QCD Monte Carlo event generator developed recently. Figure taken from [37].

with the leading order Monte Carlo predictions from PYTHIA. The central value of the next-to-leading-order predictions using the FMNR program, is always below the measurement, but agrees within the theoretical uncertainty.

Beauty in photoproduction has also been measured in the 2005 data in the same kinematic range as for the 96-00 data analysis described above [41]. Beauty was measured in this analysis using a combined three parameter fit of the p_T^{rel} and the impact parameter distribution, determining the fractions of beauty, charm, and light flavour events. The new micro-vertex detector was not yet finally calibrated and the simulation incomplete, therefore the errors of the new measurements are large and the old measurement on the HERA I data could not be improved so far. A comparison between the two measurements is given in Figure 3.9.

Beauty has also been measured using semi-leptonic decays into electrons, a muon double tag, as well as inclusive track impact parameter measurements in photoproduction and deep-inelastic scattering. Figure 3.10 summarises all these measurements as a function of the transverse momentum of the beauty quark, p_T^b. The measurements tend to be higher than the NLO predictions.

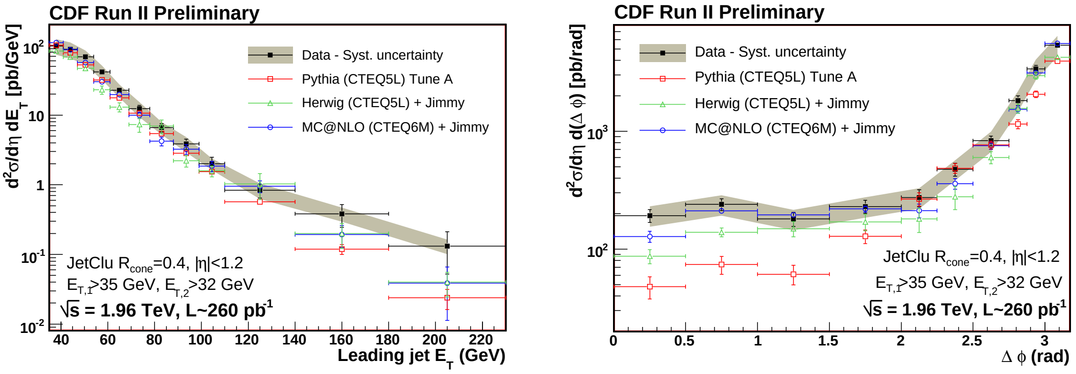

Figure 3.5: Beauty dijet correlation measurement at CDF: The left plot shows the differential cross-section as a function of E_T of the leading jet and the right plot the cross-section as a function of the azimuthal angle between the two tagged beauty jets.

3.4.2. Charm Dijet Correlation Measurements

Dijet correlations are particularly sensitive to higher-order effects and therefore suitable to test the limitations of fixed-order perturbative QCD calculations. Beauty dijet correlations have not been measured so far at ZEUS. The charm cross-section is substantially higher than the beauty cross-section, hence a dijet correlation measurement could already be performed in charm. Two analyses will be presented here measuring charm dijet correlations as a function of $\Delta\phi^{jj}$ of the two highest jets, the dijet transverse momentum, $(p_T^{jj})^2$, the dijet mass, M^{jj}, and the dijet angular distribution, $\cos\theta^*$. The cross-sections are measured separately in the direct-enriched $(x_\gamma > 0.75)$ and the resolved-enriched $(x_\gamma < 0.75)$ regions. Beauty dijet correlations are measured for these variables in this thesis for the first time.

For the measurement of the azimuthal angle of the two highest energy jets, $\Delta\phi^{jj} = |\phi^{jet1} - \phi^{jet2}|$ charm was measured by requiring a $D^{*\pm}$ meson using the decay channel $D^{*+} \rightarrow D^0\pi_s^+ \rightarrow K^-\pi^+\pi_s^+$ or the corresponding anti-particle decay. π_s^+ refers to a low-momentum (”slow”) pion accompanying the D^0. The two jets were required to have a transverse momentum of 7(6) GeV in an η-range of $-1.5 < \eta^{jet1,2} < 2.4$. The measurement was carried out in the photoproduction regime. Figure 3.11 shows a comparison of the differential cross-section measured as a function of $\Delta\phi^{jj}$ with the LO+PS Monte Carlos PYTHIA and HERWIG, as well as NLO predictions using the FMNR program. The agreement between data and the NLO prediction is good at large angles, while at smaller angles the NLO prediction underestimates the data, especially in the resolved-enriched region. Further details on the analysis, as well as cross-section measurements as a function of $(p_T^{jj})^2$, the dijet mass, M^{jj}, are given in [42].

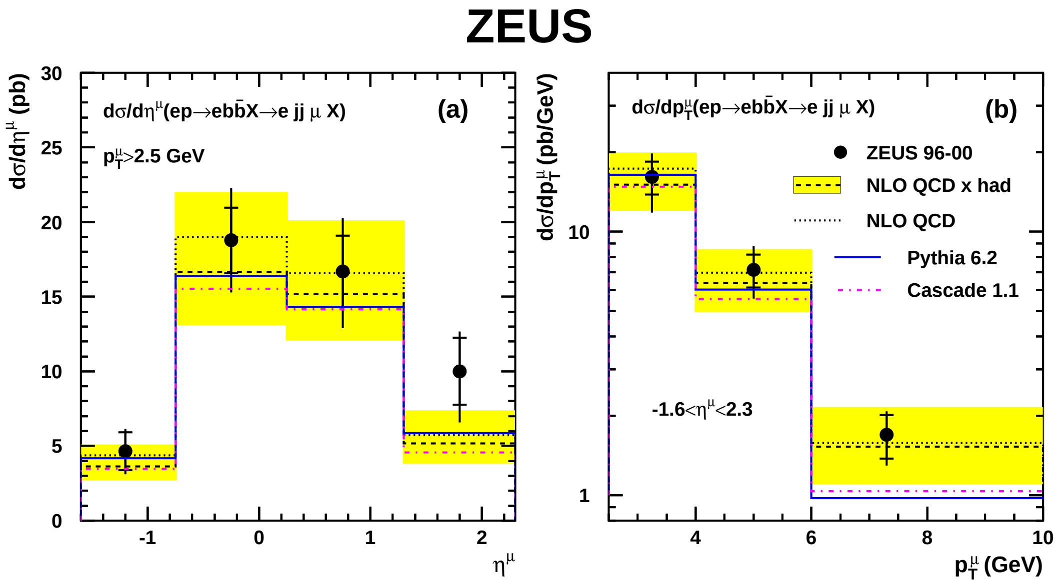

Figure 3.6: Differential beauty-quark cross-section in PhP ep collisions measured by ZEUS as a function of (a) p_T^μ and (b) η^μ for $p_T^\mu > 2.5\,\mathrm{GeV}$, two jets of $p_T^{jet1(2)} > 7(6)\,\mathrm{GeV}$ and $|\eta^{jet1(2)}| < 2.5$ using the transverse momentum of the muon relative to the jet, p_T^{rel}, to tag beauty.

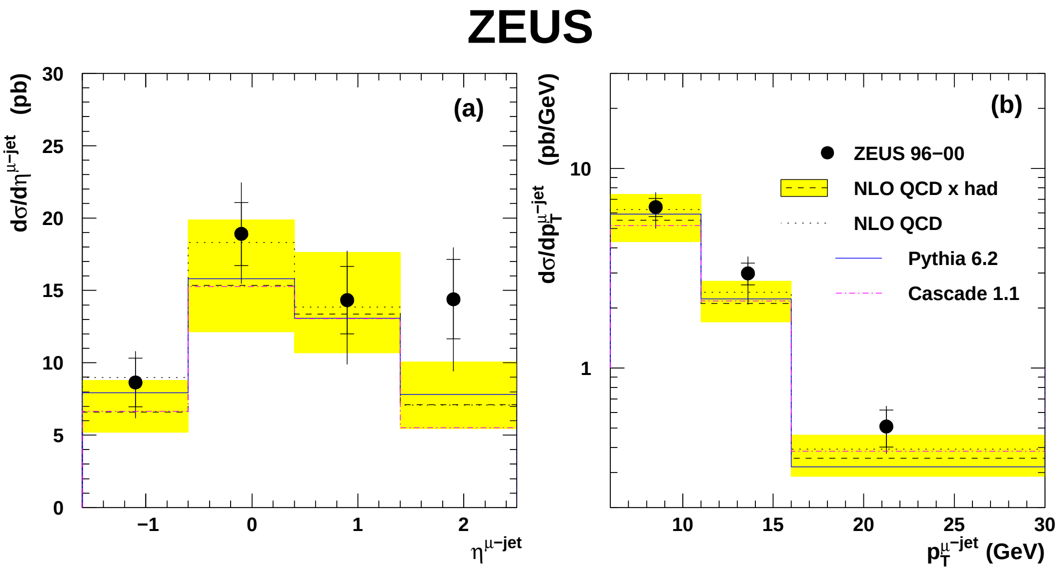

Figure 3.7: Differential beauty-quark cross-section in photoproduction ep collisions measured by ZEUS as a function of (a) $p_T^{\mu-jet}$ and (b) $\eta^{\mu-jet}$. Further details see caption of Figure 3.6.

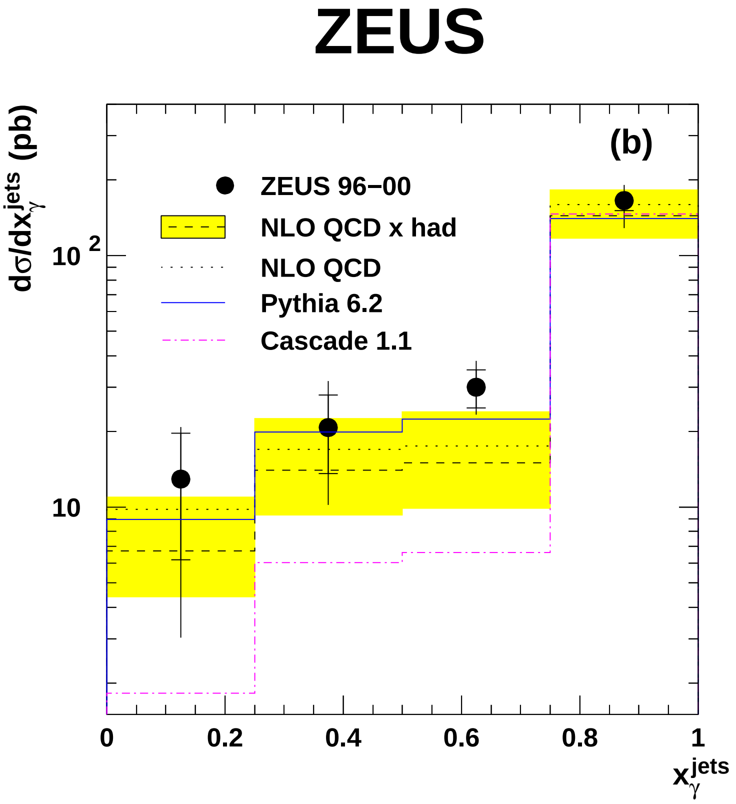

Figure 3.8: Differential beauty-quark cross-section in PhP ep collisions measured by ZEUS as a function of x_γ. Further details see caption of Figure 3.6.

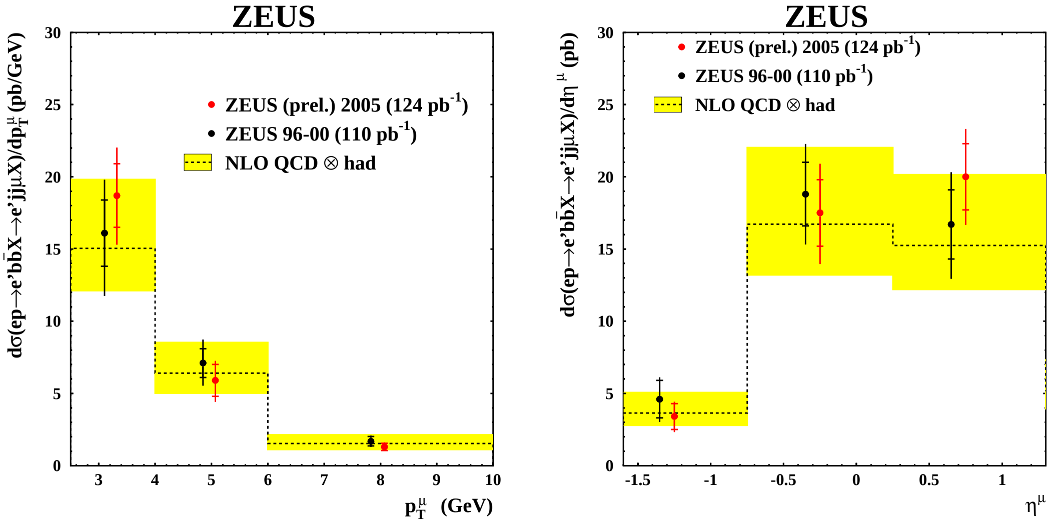

Figure 3.9: Comparison of the differential beauty-quark measurement in p_T^μ and η^μ between 96-00 data and 2005 data. Further details caption of see Figure 3.6.

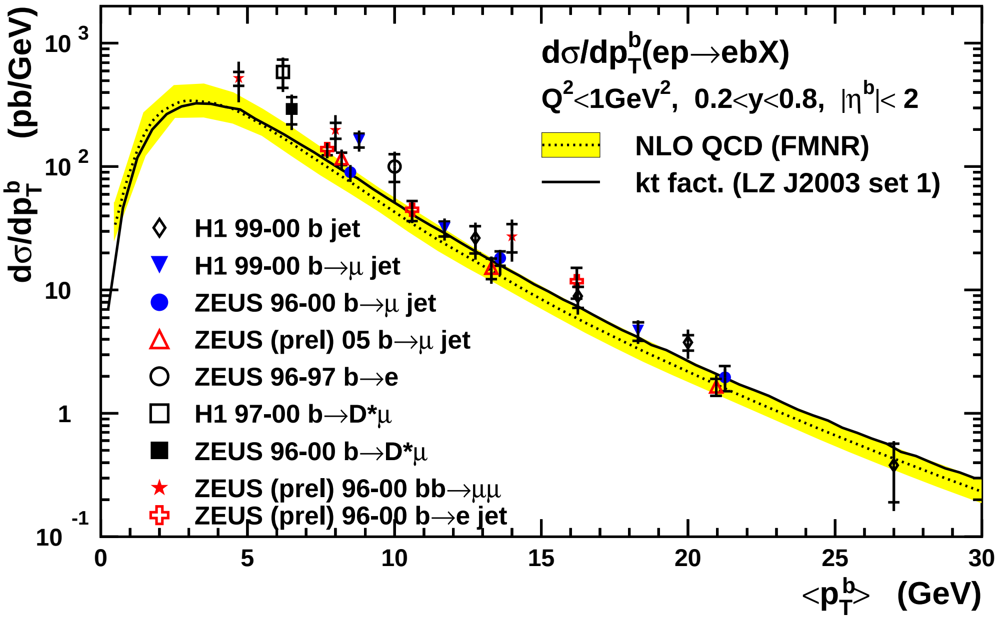

Figure 3.10: Summary of the differential beauty quark measurements in the transverse momentum of the beauty quark, p_T^b. The results are compared to NLO predictions from FMNR. Taken from [40]

Charm dijet correlations have also been measured as a function of the dijet scattering angle with respect to the proton direction in the dijet rest frame, $\cos\theta^*$:

$$\cos\theta^* = \tanh\left(\frac{\eta^{jet1} - \eta^{jet2}}{2}\right) . \tag{3.1}$$

Charm was identified in the same way as in the $\Delta\phi$ cross-section measurement requiring a D^* in the decay channel $D^{*+} \to D^0\pi_s^+ \to K^-\pi^+\pi_s^+$ or the corresponding antiparticle decay. At least two jets were required with a transverse energy of $E_T^{jet} > 5\,\mathrm{GeV}$ in a pseudo-rapidity range of $|\eta^{jet}| < 2.4$. To distinguish between the photon and proton directions the D^* is associated to the closest jet in $\eta - \phi$ space. This is the first jet in the $\cos\theta^*$ calculation. For a given dijet invariant mass, M^{jj}, events with high values of $|\cos\theta^*|$ have lower E_T^{jet}. To get rid of the bias from the E_T^{jet} cut, M^{jj} was required to be above 18 GeV. A cut on the average longitudinal boost $\bar{\eta} = \eta^{jet1} + \eta^{jet2}/2$ of $|\bar{\eta}| < 0.7$ was applied to remove the bias of the explicit cuts on η^{jet}. Figure 3.12 shows the results on the measurement separately for the direct-enriched ($x_\gamma > 0.75$) and resolved-enriched ($x_\gamma < 0.75$) samples. Direct photon events originating from the dominant quark-exchange process $\gamma g \to c\bar{c}$ and are expected to be symmetric in $\cos\theta^*$. The sample is only direct-enriched, hence a slight asymmetry is observed, as expected also from the Monte Carlo. The resolved-enriched sample has a small rise in the proton direction consistent with expectations from quark exchange, while there is a strong rise in photon direction consistent with a dominant contribution from gluon exchange. As the subprocess $gg \rightarrow c\bar{c}$ is symmetric in $\cos\theta^*$, most of the resolved photon events come from charm originating from the photon. The agreement with NLO is good in the case of the direct-enriched sample, while for the resolved-enriched sample the NLO predictions are below the data. The shape of the measured distributions is well reproduced by the NLO calculations. More details are given in [43].

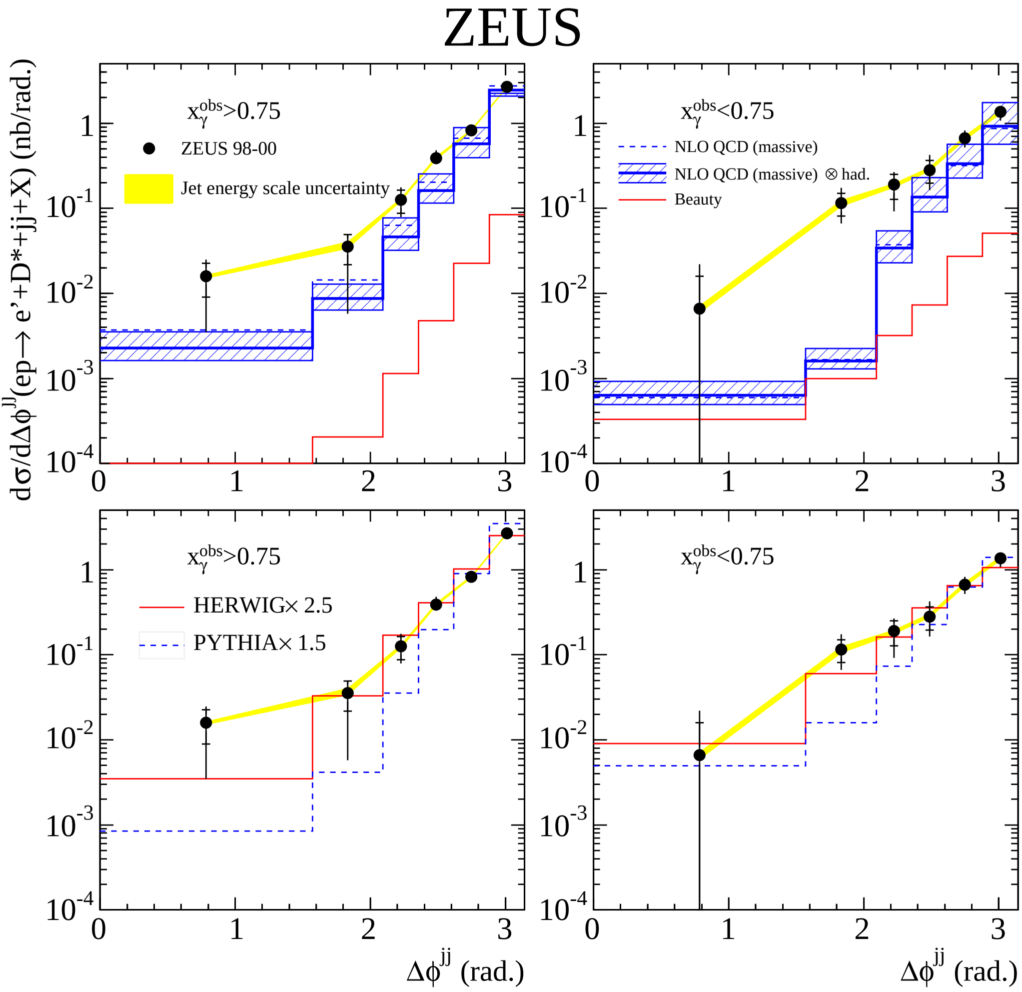

Figure 3.11: Comparison between data and NLO calculations (upper plots) and data and LO+PS Monte Carlo (lower plots) in $\Delta\phi^{jj}$ separately for the direct-enriched (left) and resolved-enriched (left) region. From [42].

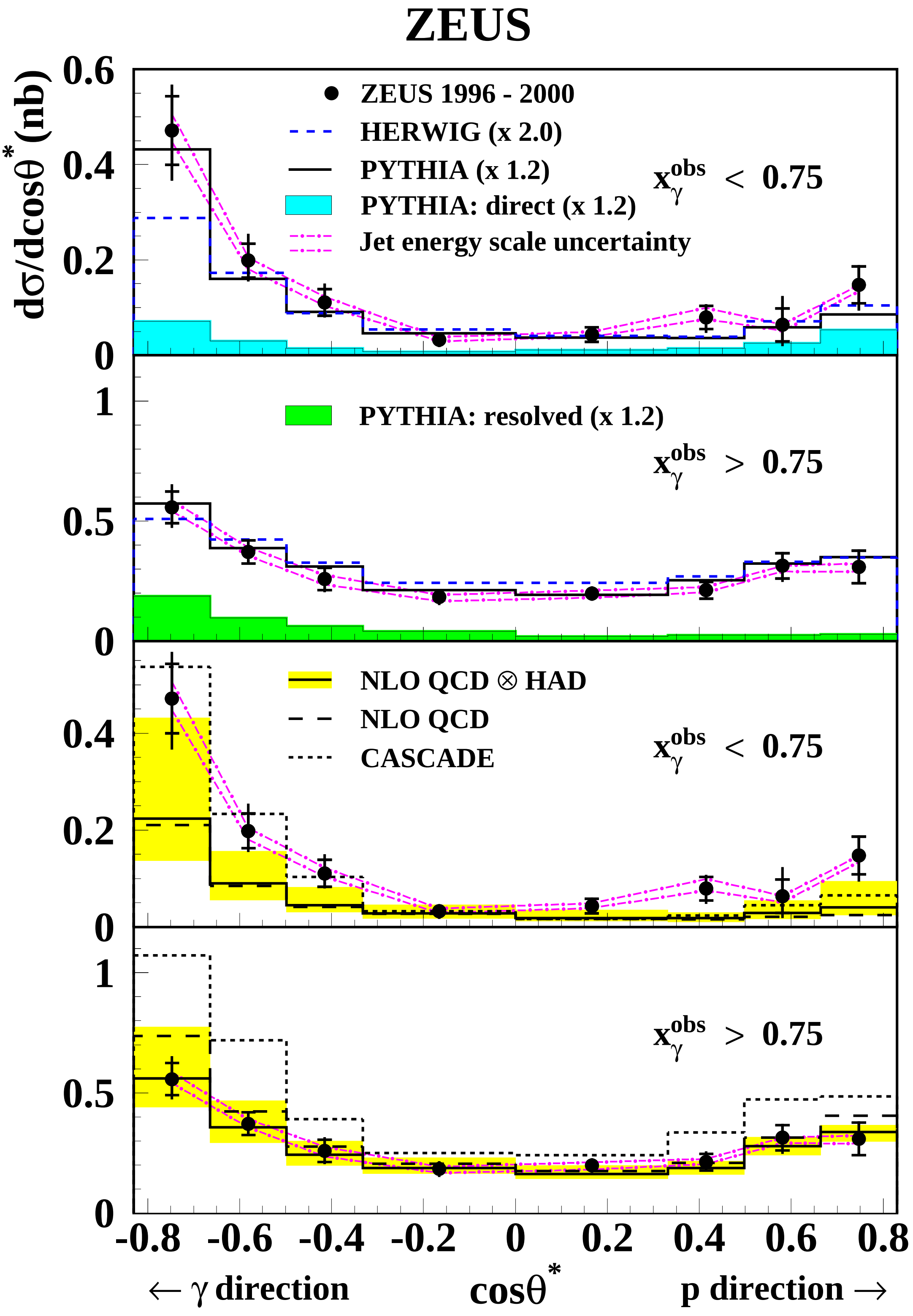

Figure 3.12: Comparison between data and LO+PS Monte Carlo (upper plots) and data and NLO predictions (lower plots) in $\cos\theta^*$ separately for the direct-enriched and resolved-enriched samples, from [43].

4. Experimental Setup

The HERA (Hadron-Elektron Ring-Anlage) accelerator (Figure 4.1) was built at the DESY (Deutsches Elektronen Synchroton) in Hamburg between 1984 and 1991. A tunnel of 6.3 km circumference was constructed 10-20 m below the surface. Electrons (positrons) at 27.5 GeV and protons at 920 GeV are brought to collision at two points yielding a centre-of-mass energy of 318 GeV. The detectors H1 in the North Hall and ZEUS in the South Hall are set up around the collision points. The main purpose of the HERMES experiment in the East Hall is the study of the spin structure of the proton. For this purpose the electron beam is first polarised longitudinally and then collides with a (polarised) gas target. Until 2003 the HERA-B experiment was situated in the West Hall. The original aim was the analysis of CP violation in the $B^0\bar{B}^0$ system using collisions of the proton beam with a wire target.

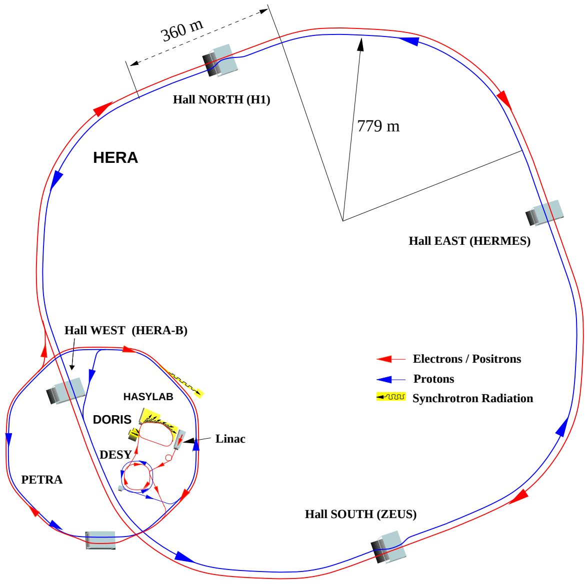

Figure 4.1: The HERA collider. Experiments are situated in each straight section. While H1 and ZEUS use both beams, HERMES and HERA-B use only the electron or proton beam; the pre-accelerators Linac, DESY and PETRA are also shown.

4.1. The HERA Collider

The electrons are injected at a beam energy of 12 GeV after passing the pre-accelerator chain of Linacs, DESY and PETRA and then accelerated to the full energy of 27.5 GeV. Protons follow a similar chain and enter the HERA beam-pipe at the injection energy of 40 GeV and are then accelerated up to 920 GeV (820 GeV until 1998). The electron (positron) and proton beams are accelerated via superconducting and conventional cavities respectively. Most of the time HERA ran with positrons. Electrons were used in 1998-1999 and in 2005-2006. Due to spin-flip synchrotron radiation, the Sokolov-Ternov effect [44], the electron beam is transversely polarised. A series of dipole magnets called spin rotators are installed to turn the polarisation longitudinally at the HERMES interaction point (IP) and since 2001 also at the ZEUS and H1 interaction points. The beam consists of 210 bunches of electrons and protons with a crossing rate of 10.4 MHz. Not all bunches are actually filled. Some bunches are left unpaired, i.e. the corresponding bunch in the other beam is left empty for background studies.

In the shutdown 2000-2002 HERA was upgraded to deliver about a factor five higher specific luminosity. At the same time the experiments upgraded their detectors to achieve higher precision measurements especially in the context of heavy flavour and high Q^2 physics. The main machine parameters are summarised in Table 4.1. The delivered luminosity is shown in Figure 4.2.

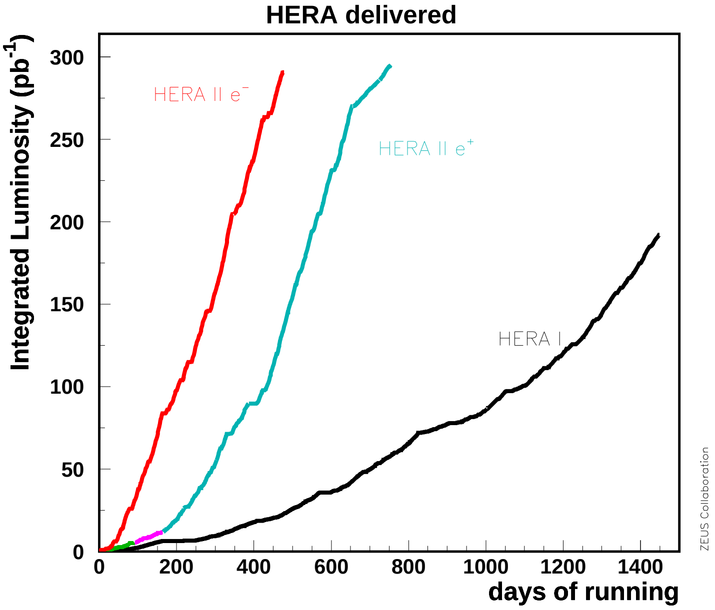

Figure 4.2: HERA delivered integrated luminosity since 1992.

HERA parameters	Design Values		Achieved in 99/00		HERA II design		HERA II achieved	
	$e^{\pm}$	p	$e^{\pm}$	p	$e^{\pm}$	p	$e^{\pm}$	p
Circumference [m]	6336							
Energy [GeV]	30	820	27.5	920	27.5	920	27.5	920
Centre-of-mass energy [GeV]	314		318		318		318	
Maximum current [mA]	58	160	45	100	58	140	40	100
No. of colliding bunches	210	210	180	180	180	180	180	180
Time between bunch crossings [ns]	96							
Horizontal beam size [mm]	0.247	0.247	0.190	0.190	0.118	0.118	0.115	0.115
Vertical beam size [mm]	0.078	0.078	0.050	0.050	0.032	0.032	0.030	0.030
Peak Luminosity [$\mathrm{cm}^{-2}\mathrm{s}^{-1}$]	$1.5 \cdot 10^{31}$		$1.7 \cdot 10^{31}$		$7.0 \cdot 10^{31}$		$5.0 \cdot 10^{31}$	

Table 4.1: HERA parameters.

4.2. The ZEUS Detector

The ZEUS detector is situated in the South Hall of the HERA ring. It has a size and weight of $12\times11\times20\,\mathrm{m}^3$ and 3600 tons, respectively. The detector started operation in 1992 but was upgraded several times since. ZEUS is a multipurpose detector to study a wide range of physics involving electron-proton scattering at HERA. The detector covers the full 4π solid angle with the exception of very small angles close to the beam-line. The detector has the typical design of high energy physics experiments. Most of the components can be seen in Figure 4.3.

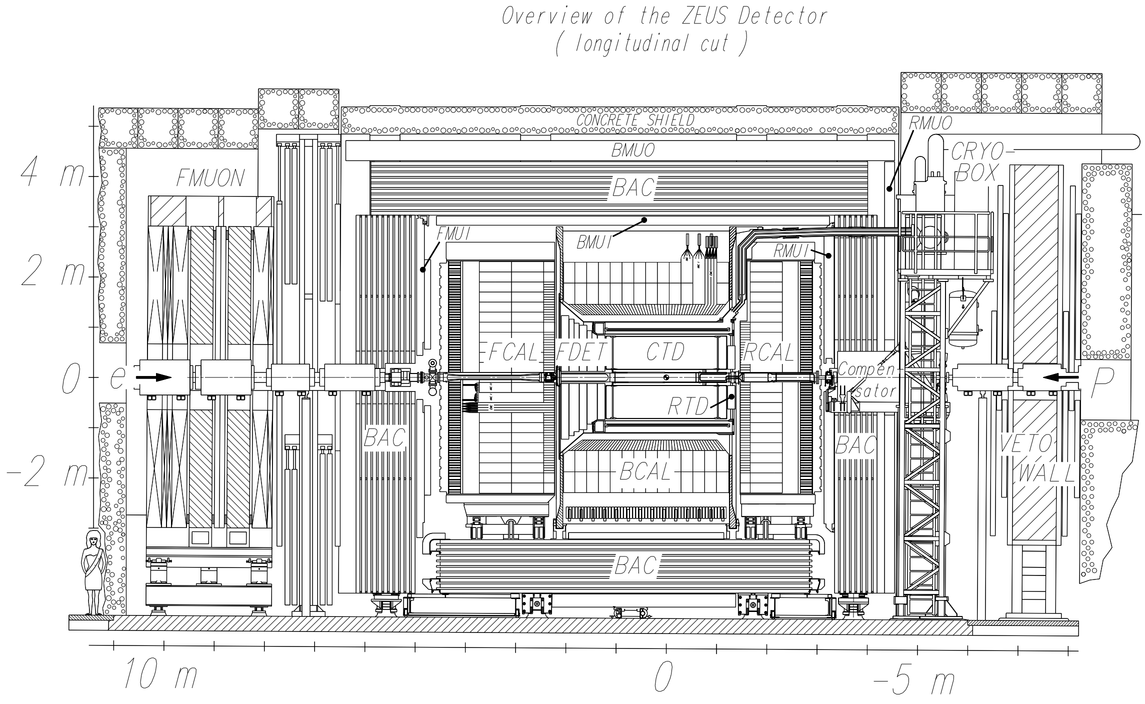

Figure 4.3: The ZEUS detector in an XY-cross-section.

In the core of the detector are the tracking detectors around the beam-pipe to reconstruct vertices and charged particle momenta followed by the calorimetry for the energy measurement. Outside the calorimeter are again tracking chambers for muon identification. The energy difference between electrons and protons leads to a boost in the proton direction. Hence the detector is specially instrumented with additional tracking devices and more material in the calorimeter in the direction of the proton beam, called the forward region.

The ZEUS coordinate system is defined as a right-handed orthogonal system with the origin at the nominal interaction point (IP). The Z-axis points in proton beam direction, the Y-axis points upwards and the X-axis to the centre of the HERA ring. The polar angle θ is measured with respect to the Z-axis and the azimuthal angle ϕ with respect to the X-axis as shown in Figure. 4.4. In general the pseudo-rapidity

$\eta = -\ln\ \tan(\theta/2)$ is used instead of the angle θ, as a difference in η is logitudinally Lorentz-invariant.

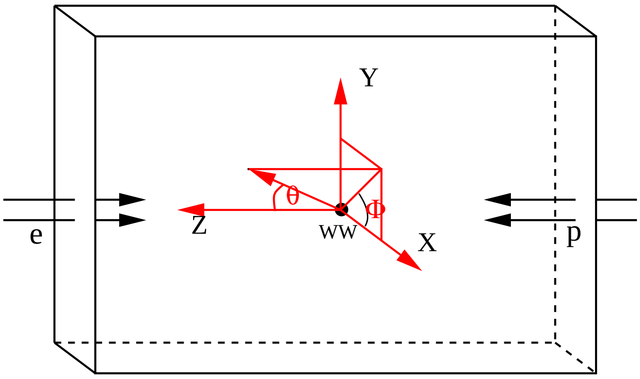

Figure 4.4: The ZEUS coordinate system.

In the following, a short description of the main detector components will be given. Detailed descriptions of the components most relevant to the analysis will follow in later sections. Starting with the innermost part, a vertex detector (VXD) was situated around the beam-pipe. It was removed during the shutdown in 1995/1996 and replaced by a silicon-strip micro-vertex detector (MVD) during the HERA upgrade in 2000/2001 to improve the tracking and especially the vertexing. The MVD is surrounded by the Central Tracking Device (CTD), a wire drift chamber explained in more detail in Section 4.3. The CTD is enclosed by a super-conducting solenoid magnet providing a homogeneous magnetic field of 1.43 T in the CTD. In the forward direction follows the Forward Detector (FDET). It consists of three planar drift chambers (FTDs) and the Straw Tube Tracker (STT). The STT is separated into two modules situated between FTD1 and FTD2 and between FTD2 and FTD3. During the HERA upgrade the STT replaced the Transition Radiation Detector (TRD) to allow a track reconstruction of high multiplicity events in the forward region. In the backward region a fourth (rear) planar drift chamber (RTD) is installed. The tracking detectors are surrounded by a high-resolution compensating uranium-scintillator calorimeter (CAL), see Section 4.4. It is the main detector for the energy measurement at ZEUS and consists of three parts: the forward (FCAL), barrel (BCAL) and rear (RCAL) calorimeters. In addition presampler detectors (FPRES, BPRES, RPRES) are mounted on the front of the calorimeter modules to correct the energy of particles that start to shower before reaching the CAL. The hadron-electron separator (HES) is installed after three radiation lengths inside the FCAL and the RCAL to improve the separation of electromagnetic and hadronic showers. An iron yoke surrounds the CAL to provide a return path for the magnetic field flux. It is instrumented with proportional chambers which allow an energy measurement of the particles passing the CAL and is therefore called the backing calorimeter (BAC) see Section 4.5.3. On the inner and outer surfaces of the BAC a system of muon detection chambers is mounted described further in Section 4.5. Attached to the front face of the RCAL is the small-angle rear tracking detector (SRTD). This scintillator-strip detector covers an area of $68 \times 68\,\mathrm{cm}^2$ around the beam-line and is used to measure the impact point of the scattered electron on the RCAL with high accuracy. In the rear an iron-scintillator detector, the VETO wall, is used to reject background from beam-gas interactions. The C5 detector consists of 2 x 2 scintillator layers interleaved with layers of tungsten. It is positioned 1.2 m from the nominal interaction point in the electron flight direction, in the central cut-out of the RTD. It also provides information on beam-gas interactions and is used as a veto for such events. Additionally its rate gives information on the general background conditions during a fill. Another important component is the luminosity detector. Electromagnetic calorimeters are placed at $Z = -34\,\mathrm{m}$ and $Z = -109\,\mathrm{m}$ to measure photons from the bremsstrahlung process $ep \rightarrow ep\gamma$, which have a well known cross-section and can therefore be used to determine the luminosity, see Section 4.6.

4.3. The Central Tracking Detector

The Central Tracking Detector (CTD) is a cylindrical drift chamber which measures the direction and momentum of charged particles as well as their energy loss, dE/dx, which can be used for particle identification [45]. The active volume ranges from $Z = -100\,\mathrm{cm}$ to $Z = +104\,\mathrm{cm}$ with an inner radius of 18.2 cm and an outer radius of 79.4 cm. It covers the polar angular range $15^\circ < \theta < 164^\circ$ and the whole azimuthal angle. The gas is a mixture of argon (82 %), ethane (13 %) and carbon dioxide (5 %). When a charged particle passes through gas it ionises the gas molecules along the trajectory. The resulting electrons drift along the electrical field lines towards the positively charged sense wires. Close to the wire avalanche-like multiplication of the electrons occurs, which results in a signal pulse which is measured via electronic readout. The CTD consists of 4608 signal wires organized in nine super-layers (SL), with each SL containing cells made up of eight sense signal wires. An octant of the CTD is shown in Figure 4.5. The drift wires of the odd numbered SL are parallel to the beam axis, whereas those of the even numbered SL are inclined by a so-called stereo angle of $\pm 5^\circ$ to achieve a better determination of the Z-position. The hit resolution is about 0.18 mm in the r - ϕ plane which leads to a resolution of about 2 mm in Z. For trigger purposes SL 1, 3 and 5 are equipped with a Z-by-timing system to determine the Z position by the difference in arrival time at both ends of the wire. The achieved resolution of 4 cm is quite poor, but the system allows a track reconstruction already at the first level trigger.

The p_T dependent resolution for vertex fitted tracks of $p_T >$150 MeV with hits in at least 3 SL is given by[1] [46]:

$$\frac{\sigma(p_T)}{p_T} = 0.0058 \cdot p_T \oplus 0.0065 \oplus 0.0014/p_T \ . \qquad (p_T \text{ in GeV}) \tag{4.1}$$

The first term is due to the position resolution, whereas the second and third are due to multiple scattering before and inside the CTD.

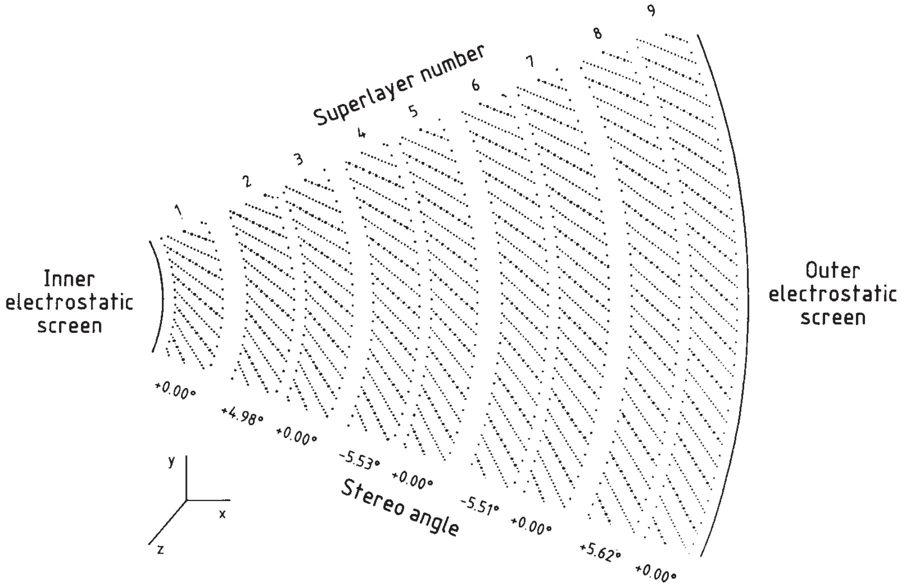

Figure 4.5: Layout of a CTD octant. The stereo angle of each superlayer is indicated.

4.4. The Electromagnetic and Hadronic Calorimeter

The ZEUS calorimeter (CAL) [47–49] is a compensating sampling sandwich calorimeter. The energy is measured via scintillating material, which turns the deposited energy into light that can than be measured via photomultipliers. As the radiation length of scintillators is large, material with a short radiation length is alternated with the scintillators to reduce the size of the calorimeter. The scintillators are "sandwiched" between the absorbers. Therefore only a fraction of the energy is measured and the calorimeter is called "sampling". The absorber layers are made of 3.3 mm thick depleted uranium (98.1% U^{238}, 1.7% Nb, 0.2% U^{235}) and the active layers are made of 2.6 mm thick plastic scintillators.

---

[1] $a \oplus b = \sqrt{a^2 + b^2}$

Electromagnetic and hadronic showers develop differently. The signal from hadronic showers is smaller due to nuclear reactions that don't result in a measurable signal. The signal from electromagnetic showers would thus normally be higher than for hadronic showers. Using uranium as absorber material one can compensate for this effect. Uranium has a high yield of spallation neutrons depositing their energy in the scintillator and photons from subsequent neutron captures in the uranium deposit their energy in the scintillator. Choosing the right thickness for absorber and scintillator one can achieve the same signal for hadronic and electromagnetic showers. In ZEUS compensation of $e/h = 1.00 \pm\ 0.05$ was attained.

An important characteristic of a calorimeter is the energy resolution. It was measured under test-beam conditions for electrons and hadrons to be:

$$\frac{\sigma_e}{E} = \frac{18\%}{\sqrt{E}} \quad \text{and} \quad \frac{\sigma_h}{E} = \frac{35\%}{\sqrt{E}} \,, \tag{4.2}$$

with E in GeV.

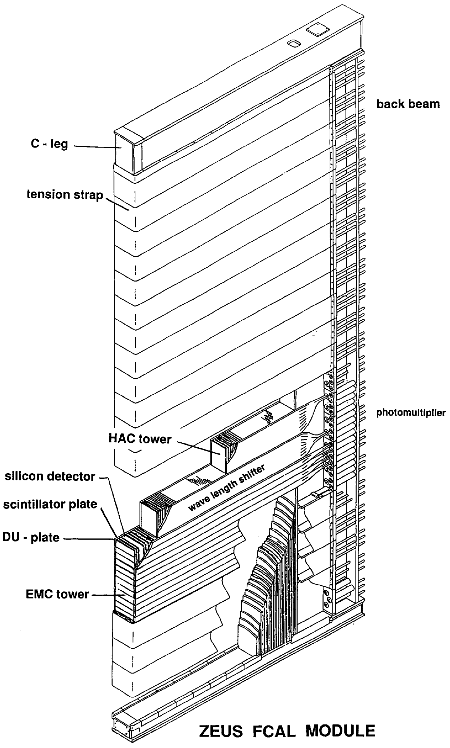

Figure 4.6: View of an FCAL module.

The ZEUS calorimeter is divided into the forward calorimeter (FCAL), the barrel calorimeter (BCAL) and the rear calorimeter (RCAL) covering together 99.8% of the forward and 99.5% of the backward hemisphere solid angle. FCAL and RCAL consist of 23 rectangular modules, see Figure 4.6, which each consist of up to 23 towers of

$20\times20\,\mathrm{cm}^2$. The BCAL has 32 wedge-shaped modules surrounding the CTD. A tower is segmented longitudinally into an electromagnetic (EMC) and two hadronic (HAC) sections (only one HAC for RCAL). The EMC sections are additionally subdivided into four transverse cells of $5\times20\,\mathrm{cm}^2$. Each of the 5918 cells is read out on two sides via wavelength shifters by photomultiplier tubes. The left-to-right signal ratio gives an approximation of the transverse position of the shower in the cell and the measurement becomes less dependent on the impact point of the particle. The time resolution of the CAL of 1-2 ns is used to reject non $e-p$ background already at the trigger level using characteristic timing patterns.

4.5. Muon Chambers

The main aim of the muon detectors is the measurement of minimum ionising particles such as muons, which are produced in the interaction region and cross the whole calorimeter and the iron yoke. The muon detection system is divided into two detectors, namely the forward muon chamber, FMUON, and the barrel and rear muon chambers, BMUON/RMUON. As for the other tracking detectors the forward region is more finely instrumented to account for the Lorentz boost in the proton direction. In addition the instrumented iron yoke (BAC) is used for muon detection. In the following sections these components will be described in more detail.

4.5.1. The Forward Muon Detector

The FMUON [50] is divided into two regions: the inner detector (FMUI) situated between the FCAL and the BAC and the outer detector (FMUO) outside the BAC. A schematic view is given in Figure 4.7. The FMUON consists of:

- a system of four planes of limited streamer tube trigger planes (LST1-4) with digital radial, ρ, and azimuthal, ϕ, readout;
- two larger planes of LSTs with digital (ρ, ϕ) readout and analogue ρ readout in the so-called large polar angle region (LW1,LW2);
- four planes of drift chambers DC1-DC4;
- two large toroidal iron magnets providing a magnetic field of 1.7 T for charge separation and momentum measurement in the angular region of $5^\circ - 16^\circ$.

The Limited Streamer Tube Trigger Planes (LST) have the aim to trigger on the muon. At the same time the azimuthal and radial position of the muon candidate is reconstructed. A trigger plane consists of four LST chambers grouped in two half-planes. A quadrant is made of two layers of LSTs, positioned horizontally inside a plastic sheet. The tubes of the two planes are displaced by half a cell width in order to get a full geometrical acceptance. Each quadrant is contained in an aluminium air-tight box where nitrogen can flow. If a muon passes the chamber a signal is generated

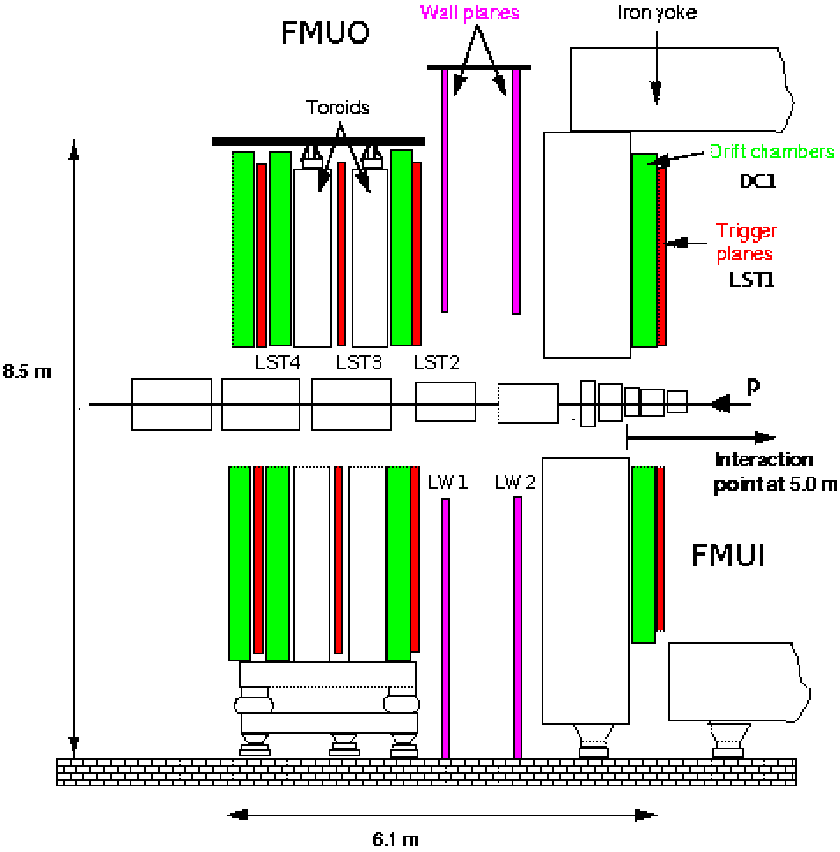

Figure 4.7: The Forward Muon Spectrometer.

on the anode wire which also induces a signal on the copper strips, glued on the plastic sheet which serves as the cathode. There are 132 radial strips each of them 1.9 cm wide divided along the bisector of the quadrant so that the simplest readout unit of the trigger plane is an octant. There are 32 azimuthal strips per octant. Each strip covers 1.4° in ϕ.

The Drift Chambers (DC) are used to improve the momentum resolution of the track. Each DC plane consists of four chambers. The basic element of the chamber cell is a gas volume containing four sense wires and wires to generate an electric field. The sense wires are perpendicular to the beam axis and measure therefore the radial coordinate. The information is then sent to a TDC which converts them into a time value connected to the space distance by a known relationship. The information obtained from the wires within a cell is combined to a segment reproducing the crossing of a particle.

The Large Angle Coverage Planes (LW) increase the geometrical acceptance of the FMUON to the region left uncovered by the toroid magnets ($16^\circ < \theta < 32^\circ$). Each LW contains eight layers of LSTs. The LST signal is induced on copper strips as for the trigger planes. There are 64 ϕ strips corresponding to a spacing of 0.7° and 192 ρ strips corresponding to a distance of 1.8 cm between the strips per octant. The readout is digital for the ϕ-strips, while the ρ-strips have an analogue readout, like the wires of the drift chambers. A resolution of 1mm is achieved in the radial direction using the method of the charge barycentre. A layout of a LW plane can be seen in Figure 4.8.

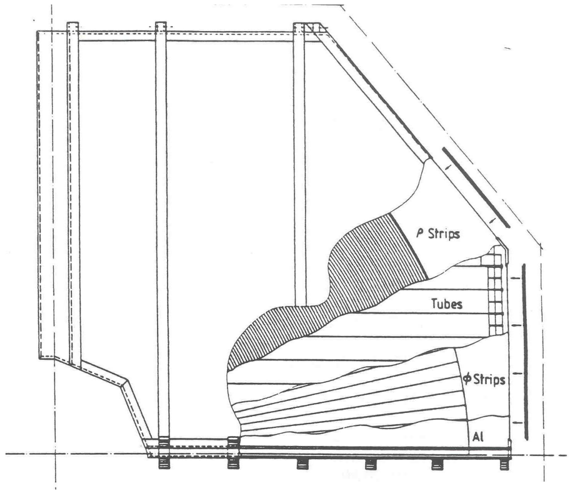

Figure 4.8: Layout of a large-angle coverage plane, LW.

4.5.2. The Barrel and Rear Muon Chambers

The barrel and rear muon chambers [51] consist mainly of LST planes. Together they cover an area of about 2000 m^2. In Figure 4.9 a blow-up view of the chambers is shown. As for the FMUON, the BMUON and the RMUON are also subdivided into an inner part mounted between the CAL and the backing calorimeter, and an outer part outside the BAC. Although of varying shape and dimension the internal chamber structure remains the same: an aluminium honeycomb support structure with a double layer of LST planes on each side. In the BMUON the LSTs are mounted parallel to the beam-line while they are orthogonal in the RMUON.

The determination of the position of a particle is done through readout of the hit wires and the induced charge along the strips. If in the event a trigger signal from the BMUON is available, the readout is analogue, while in the other case it is digital. The spatial resolution achieved with the analogue strip readout is 200 μm orthogonal to the wires and 700 μm parallel to the wires [52].

The structure of the detector allows the position of the track at the exit of the calorimeter to be measured very accurately. Due to the magnetisation of the yoke a momentum reconstruction of the track is also possible. Matching the track in a next step to a compatible track in the inner detector then reduces the background from muons not produced at the interaction point, e.g. decays in flight of kaons and pions.

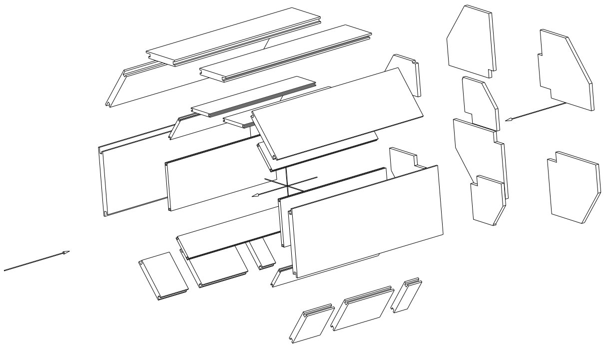

Figure 4.9: Blowup of the BMUON and RMUON.

4.5.3. The Backing Calorimeter (BAC)

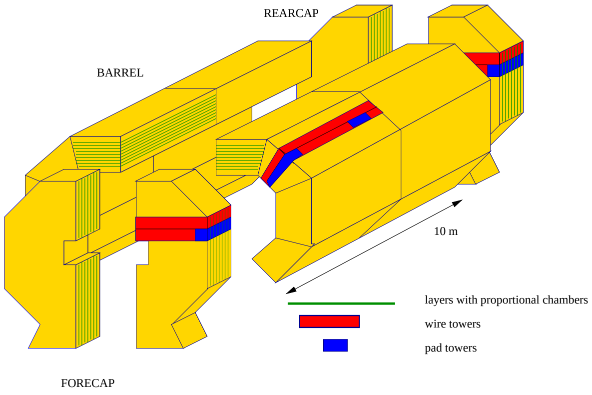

Figure 4.10: Blowup of the BACking Calorimeter.

The iron return yoke between the inner and outer muon chambers is instrumented with aluminium proportional tubes to measure the energy of hadron shower leakages out of the calorimeter and to correct the jet energy measurement; it is therefore called the Backing Calorimeter (BAC). Additionally it is used as a muon detector to improve the tracking of muons between the inner and outer chambers. It is specially useful in regions barely covered by the muon chambers. In HERA II the BAC is also used in the muon triggers.

The BAC modules consist of 7-8 tubes (channels) with a cross section of $11 \times 15\,\text{mm}^2$ and a length from 1.8 to 7.3 m. The signal wires are made of gold-plated tungsten with a diameter of $50\,\mu$m supported every 50 cm. 50 cm long aluminium cathode pads are located on the top of the modules. The wires are read out on one side and provide analogue (for the energy measurement) and digital (for the position measurement) signals, while the pads have analogue readout only.

Energy is measured by summing up the analogue signals from the wires grouped in addition into towers with a width of 25-50 cm (2-4 modules) over the full depth of the BAC. 2-4 neighbouring pads are grouped into pad towers with an area of 50 × $50\,\text{cm}^2$ (4 modules) similar to the wire towers. They provide information on the location of the energy deposit along the wires.

The BAC spatial resolution perpendicular to the wires is ~ 1 mm. Parallel to them it is mainly determined by the pad size, and is thus about 50 cm $/\sqrt{12}$. The energy resolution from test-beam measurements is:

$$\frac{\sigma_E}{E} \sim \frac{110\%}{\sqrt{E}(\text{GeV})} \ . \tag{4.3}$$

4.6. Luminosity Measurement

The time-integrated luminosity is defined as

$$L_{int} = \frac{N_{proc}}{\sigma_{proc}} \ , \tag{4.4}$$

where N_{proc} is the number of events for a specific process and σ_{proc} the cross-section of that process. If the process can be calculated accurately, measured with high precision and has a high rate, it can be used as input for the cross-section determination of other processes.

At ZEUS, the QED bremsstrahlung process $ep \rightarrow e\gamma p$ is used. It has a large cross-section and can be calculated as a function of the photon energy [53, 54]. An overview of the ZEUS LUMI system is shown in Figure 4.11.

There are two methods to measure the photon rate, where the second one is only available in HERA II. The bremsstrahlung photons with $\theta < 0.5\,\text{mrad}$ leave the beam-pipe through a Cu–Be window at $Z = -92\,\text{m}$ from the interaction point. The first method measures the bremsstrahlung photon directly. Photons traversing the exit window without conversion to electrons are detected at $Z = -106\,\text{m}$ in the lead–scintillator calorimeter LUMIG. A position reconstruction with a precision of 0.2 cm is provided by two layers of orthogonal 1 cm wide scintillator strips installed at a depth of $7X_0$ within the LUMIG. In front of the detector, a carbon–lead filter shields it against synchrotron radiation. The largest background arises from electron bremsstrahlung on the residual gas. Measuring the currents in the paired and unpaired electron bunches and the bremsstrahlung rate for the unpaired electron bunches, the beam-gas background can be subtracted. A detailed description of the method can be found in [55]. Monte Carlo simulations have shown that a total systematic error of 2% should be attainable [56].

About 10% of the photons convert into e^+e^- pairs in the exit window and are bent out of the photon direction by a spectrometer dipole magnet. The second method measures now the photon rate indirectly by counting e^+e^- coincidences in two small tungsten-scintillator calorimeters. The spectrometer has small acceptance in coincidence ($\approx$ 3%) and no acceptance for low energy photons. Therefore the probability of pile-up and synchrotron radiation (SR) photon coincidences is small. The main error of this method comes from the uncertainty in the acceptance. Monte Carlo simulations have shown that a total systematic error of 1.4 % should be attainable [57]. A sketch of the lumi spectrometer is given in Figure 4.12

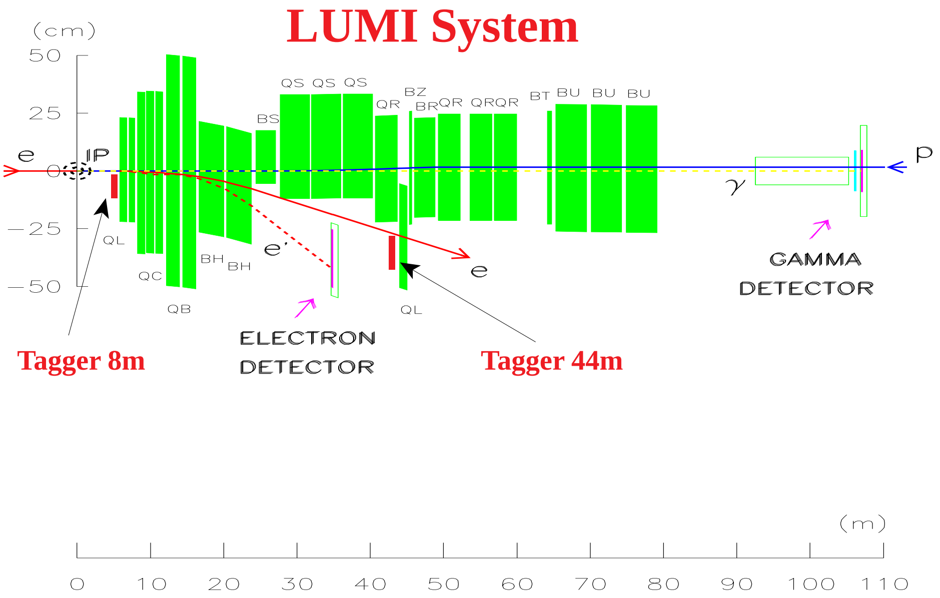

Figure 4.11: Layout of the luminosity measuring devices: The blocks indicate bending and quadrupole magnets. The detectors at -35 m and -44 m measure electrons that are scattered under very small angles and are used for tagging γp events. The photon detector and spectrometer are situated at $Z = -106$ m.

4.7. Trigger and Data Acquisition

The bunch-crossing rate at HERA is 10.4 MHz, while the rate of interesting physics events varies between 0.05 Hz for NC DIS events with $Q^2 > 100\,\mathrm{GeV}^2$ and 250 Hz for soft PhP events (for an instantaneous luminosity of $2 \cdot 10^{31}\,\mathrm{cm}^{-2}\mathrm{s}^{-1}$) [50]. The rate of background events due to interactions with the residual gas nuclei or elements from the beam-line (beam-gas events) is about 10 kHz and additional background is given by cosmic ray muons passing through the detector. The total data size per event is typically $\mathcal{O}(10^5)$ bytes while the writing speed is limited to $\mathcal{O}(10^6)$ bytes/s. Hence a significant reduction of the data rate and size is needed.

A three level trigger system is used to select events online as shown in Figure 4.13. The complexity of the trigger decisions rises from level to level, while the data is reduced:

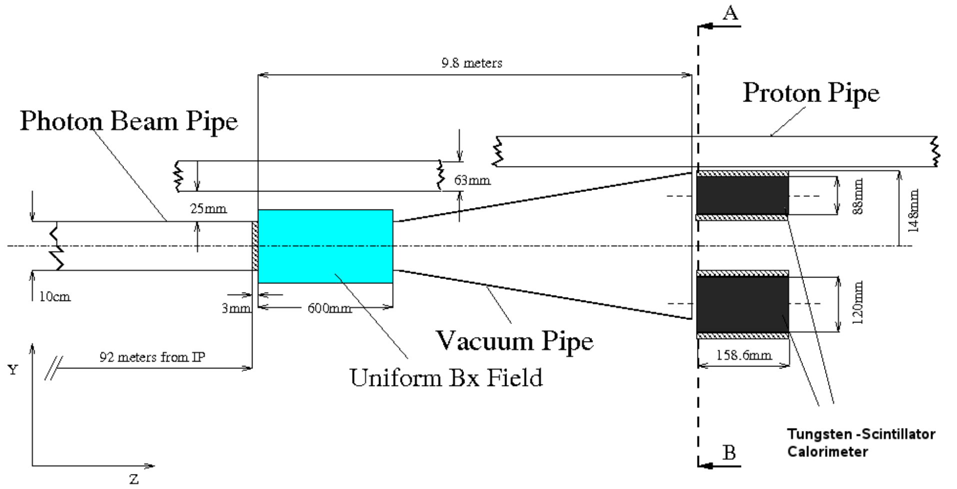

Figure 4.12: Layout of the HERA II luminosity spectrometer: The photons are converted into e^+e^- pairs in the exit window, a uniform magnetic field then separates the e^+e^- pairs, which are then registered by two small calorimeters.

First-Level Trigger (FLT): The first level trigger decision is mainly taken by the CAL and the tracking detectors. Each component's FLT is implemented in hard-wired logic circuits and takes its decision on the basis of energy sums, thresholds or timing information, while the data is stored in pipelines to keep the dead time low. This decision is sent to the global first level trigger (GFLT) which combines the information from the different detector components so that the final decision to pass the event to the second level trigger is taken after $4.4\,\mu$s. The typical output rate of the GFLT is below 1 kHz.

Second-Level Trigger (SLT): The second-level trigger uses a network of programmable transputer CPUs, optimised for parallel processing. It has to reduce the output rate to less than 100 Hz. For the SLT each component recalculates quantities with higher precision, e.g. beam-gas background is rejected on the basis of CAL timing information, which is now available. The information is sent to the GSLT and a decision is made after about 7 ms. For GSLT accepted events, the data from all components is combined into a single record of ADAMO [58] database tables by the *event builder* and passed to the third level trigger. The GSLT was complemented in 2001 by an additional tracking trigger called the global-tracking trigger (GTT).

Third-Level Trigger (TLT): The TLT fully reconstructs the event on a computer farm. The decision is now based on kinematic variables, muon, electron finding algorithms, hadronic final state topologies etc. Accepted events are written to tape at a rate of 5-10 Hz and are then reconstructed offline with more sophisticated algorithms.

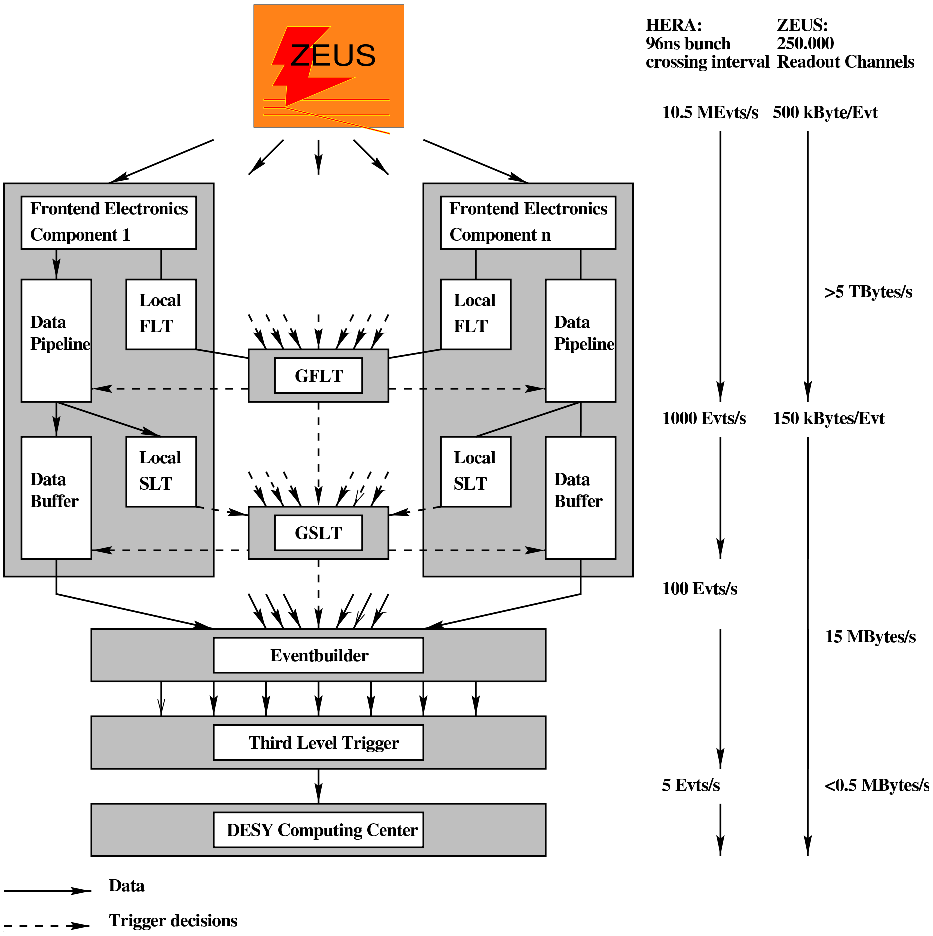

Figure 4.13: The ZEUS trigger and data acquisition system.

5. Event Reconstruction

The reconstruction of the event properties needed to identify semi-leptonic beauty decays into muons consists of the reconstruction of the hadronic system and the muon reconstruction. The reconstruction of the hadronic system is based on track and energy information combined into energy flow objects (EFOs). These are the input for the jet algorithm.

For the identification of the muons a set of muon finder algorithms using information from the inner tracking chambers, the calorimeters and the muon chambers is used. These finders are combined into a general muon finder, to improve the efficiency and to benefit from redundancies.

In this chapter the different ingredients of the event reconstruction are presented. Starting with the inner tracking, followed by the calorimeter energy measurement, the combination of the tracking and calorimeter information and the description of the jet algorithm and coming finally to the muon reconstruction.

5.1. Track Reconstruction

The track reconstruction combines hit information from the inner tracking detectors to reconstruct charged particle trajectories, taking into account the errors on the hit measurements, the dead material distribution, the resulting expected multiple scattering and the magnetic field. The detector used in HERA I is the CTD, described in Section 4.3. A micro-vertex detector (MVD) has been installed in ZEUS in 2001 and is used for the track reconstruction together with the CTD for the HERA II data.

The track model used in all running periods is a five parameter helix [59, 60], designed to describe particle tracks in an axial magnetic field parallel to the beam axis. Relative to an arbitrarily chosen reference point in the XY plane, e.g. $X_{ref}, Y_{ref} = (0, 0)$, the origin of the coordinate system, the helix is defined in the following way (see Figure 5.1):

1. Φ_H: angle of the tangent of the helix w.r.t. the X-axis;

2. Q/R: Q is the charge and R the radius of curvature;

3. QD_H : D_H connects the helix to the reference point at the distance of closest approach of the helix relative to the reference point;

4. Z_H gives the Z coordinate at the point of distance of closest approach;

5. $\cot\theta = \tan\lambda, \lambda = \pi/2 - \theta$ is the dip angle of the dip with respect to the XY plane. Any point on the helix is expressible as a function of the trajectory's outbound path-length in the XY plane: $s(\phi) = -QR(\phi - \phi_H)$

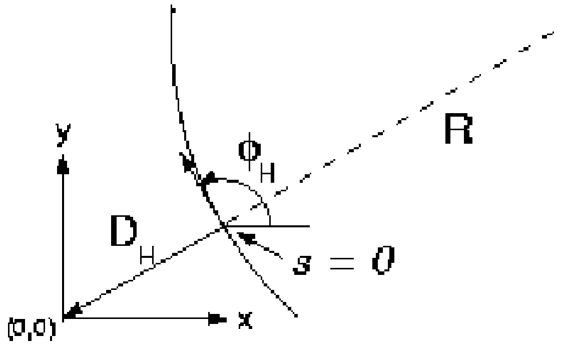

Figure 5.1: Helix in XY view for a positively charged track.

5.1.1. Track Reconstruction in the CTD

For the 96-00 running period two types of track reconstruction exist: the regular tracking, using CTD hits and if they match a 3D track segment in the first Forward Tracking Detector (FTD1), or a track segment from the Rear Tracking Detector (RTD); the second tracking mode uses only the CTD information regardless of whether there is a matching FTD or RTD segment. In this thesis the *CTD-only* mode, is used.

The first step of the track reconstruction is the *pattern recognition*. Starting from the outside, each track candidate begins as a track seed consisting of three CTD hits from an axial superlayer. The track seed is then extrapolated inwards, gathering additional hits with increasing precision as the trajectory parameters are updated. In the next step each track candidate is fit to the five parameter helix model.

In order to determine the primary vertex a simple initial fit determines the weighted centre-of-gravity for all tracks extrapolated to the beam-line. Tracks with high contribution to the χ^2 of the fit are discarded. The full vertex fit is carried out in an iterative procedure. In each iteration step the tracks associated with the vertex candidate are refitted, using the obtained vertex position from the previous iteration as an additional measurement of the tracks, until the vertex position converges.

Since 2001 the MVD supplements the CTD measurement along the particle track with high precision measurements between the vertex and the innermost CTD hit. This should improve the track and vertex resolution substantially.

5.2. Reconstruction of Calorimeter Variables

The CAL (Section 4.4) photomultiplier signals have to be converted into particle energy measurements during the event reconstruction. To translate the photomultiplier measurement into energy values, calibration factors determined in test-beam measurements are used. Further corrections for noise and detector effects have to be applied.

The main sources of noise are sparks in the photomultipliers and cells with temporarily badly behaving photomultipliers or readout electronics, so-called hot cells. Hot cells can be determined in offline CAL data quality monitoring, resulting in a list of bad channels. Noise due to sparks in the photomultipliers can be suppressed by setting cell energy thresholds for isolated cells. If no signal in neighbouring cells is detected and the cell itself has a signal corresponding to less than 80 MeV in the electromagnetic and 140 MeV in the hadronic calorimeter, the cell information is discarded. Bigger sparks can be suppressed using the two independent photomultipliers of each CAL cell.

For remaining differences to the test beam measurement, energy scale correction values are calculated [61] and applied to the data. The correction factors used in the 96-00 data period are summarised in Table 5.1. Additional corrections for incompletely modeled dead material are applied in the offline analysis. From the corrected CAL information, the total transverse energy, E_T^{CAL}, is calculated as the scalar sum of the transverse energy of each cells:

$$E_T^{\mathrm{CAL}} = \sum_{i=1}^{N_{\mathrm{cells}}} E_i \cdot \sin(\theta_i) \ . \tag{5.1}$$

CAL section	Cell Type	Correction 96-97	Correction 98-00
FCAL	electromagnetic	4.0 %	2.4 %
	hadronic	-5.0 %	-5.9 %
BCAL	electromagnetic	4.0 %	5.3 %
	hadronic	8.2 %	9.6 %
RCAL	electromagnetic	2.2 %	2.2 %
	hadronic	2.2 %	2.2 %

Table 5.1: Energy correction factors for the electromagnetic and hadronic parts of the FCAL, BCAL and RCAL for the running periods 1996-1997 and 1998-2000.

5.3. Reconstruction of the Hadronic System

The energy measurement of particles is an important ingredient to the reconstruction of the event properties. For the calorimeter energy measurement the resolution improves with increasing energy of the particles ($\sigma_E/E \sim 1/\sqrt{E}$), while for the momentum measurement in the CTD it is the other way around. To benefit from the best measurement in all energy ranges the track momentum measurement and the

CAL energy measurement are combined to *energy flow objects*, (EFOs). The resolution dependence on the electromagnetic energy and the transverse momentum of the track is shown in Figure 5.2 with the typical resolutions used in the tuning of the combination algorithm. The track information is mainly used below 10-15 GeV and the calorimeter energy measurement for higher energies. In the following this combination process is described.

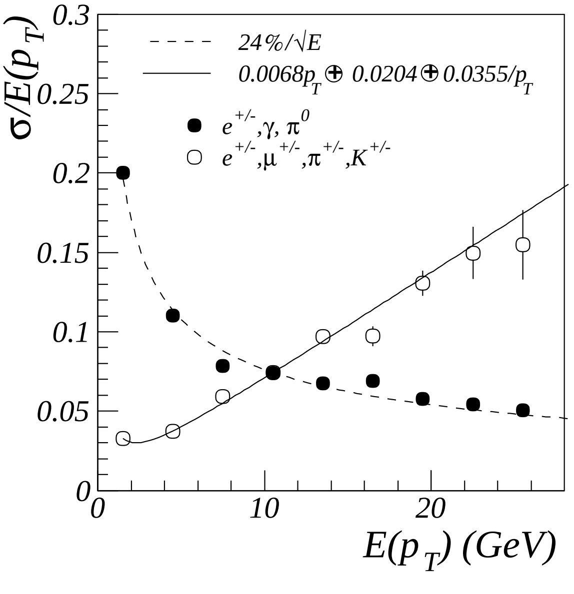

Figure 5.2: Resolution from single particle Monte Carlo simulation for the electromagnetic energy in the EMC (closed points) and for the transverse momentum in the CTD used in the tuning of this combination algorithm, taken from [62].

5.3.1. Reconstruction of Energy Flow Objects

The first stage of the reconstruction procedure [62] clusters the cell energy measurements separately in each of the calorimeters (FCAL, BCAL, RCAL) for each calorimeter layer (EMC, HAC1, HAC2) into so-called islands. To form islands all neighbouring cells with an energy deposit above the noise level are grouped together, starting from the cell with the largest signal. The procedure can be improved by forming so-called *cone islands*, combining islands in cones of ϕ and θ, oriented towards the interaction point. Here one starts at the HAC2 and combines cell islands across the different calorimeter layers. The grouping is based on a probability function, which depends on the angle between the cell-islands [63]. The position of the cone island is determined from the logarithmic centre of gravity of the shower[1]. The

---

[1] Using logarithmic weights instead of linear weights takes into account the exponential fall-off of the shower energy distribution from the shower maximum and avoids systematic biases due to varying cells solid-angle as seen by the vertex.

result is an island with three coordinates and a radius defined as the distance of the island on the plane perpendicular to a ray drawn from the vertex to the island. At low energies ($\lesssim 10\,\mathrm{GeV}$) the cone island method has a poor resolution and some low energy particles are not measured at all. Here the CTD track measurement comes into play.

For the track reconstruction vertex-fitted tracks which pass at least 4 superlayers in the transverse momentum range $0.1 < p_T^{\mathrm{track}} < 20\,\mathrm{GeV}$ are taken. If the track has hits in more than seven superlayers the track information is preferred up to $p_T^{\mathrm{track}} = 25\,\mathrm{GeV}$. The tracks are extrapolated to the front-face of the CAL taking the magnetic field into account and further into the CAL by a linear approximation using the momentum vector at the CAL surface. The matching criterion used for the track-island matching is the distance of closest approach (DCA) of the track and the position of the island. A track is matched to the island, if the DCA is smaller than the island radius or lower than 20 cm, see Figure 5.3.

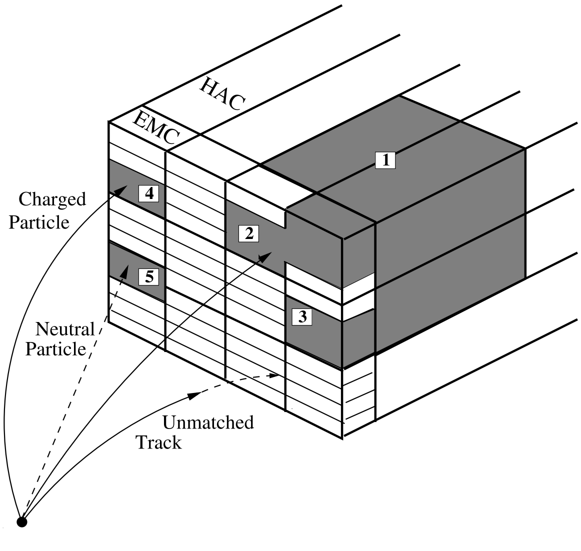

Figure 5.3: Reconstruction of EFOs by a match between CAL cells clustered into islands and tracks. EMC cell islands 2 and 3 are joined with HAC cell island 1 to form a cone island. In the next step, the cone islands are matched to tracks [62].

The track information is used in the following cases:

- the relative uncertainty on the momentum measurement is smaller than the relative uncertainty of the calorimeter measurement, see Figure 5.2:

$$\sigma_p/p < \sigma_{E_{\mathrm{CAL}}}/E_{\mathrm{CAL}} \;, \tag{5.2}$$

  where σ_p and $\sigma_{E_{\mathrm{CAL}}}$ are the measured resolutions of the track momentum and the CAL energy respectively.

- the track momentum exceeds the energy measurement in the CAL within the resolution on the measured ratio E_{CAL}/p:

$$E_{\mathrm{CAL}}/p < 1.0 + 1.2 \cdot \sigma_{E_{\mathrm{CAL}}/p} \ , \tag{5.3}$$

  where the uncertainty $\sigma_{E_{\mathrm{CAL}}/p}$ is calculated using $\sigma_{E_{\mathrm{CAL}}/p} = (E_{\mathrm{CAL}}/p^2)\sigma_p \oplus (1/p)\,\sigma_{E_{\mathrm{CAL}}}$.

As muons are minimum ionising particles (MIP) they lose only part of their energy in the calorimeter, hence the value E/p is small. Objects with the properties of muons are therefore treated separately, i.e. the tracking information is favoured if the following requirements are fulfilled:

- $E_{\mathrm{CAL}} < 5\,\mathrm{GeV}$;
- $E_{\mathrm{CAL}}/p < 0.25$;
- $p_T < 30\,\mathrm{GeV}$.

In addition to the clean matches of one track to one island, the following three categories exist:

- good tracks which are not associated with any calorimeter object are counted as charged energy. The CTD information is used under the assumption that the particle is a pion;
- calorimeter objects not associated with any track are counted as neutral energy and the calorimeter information is used for the four-vector reconstruction;
- calorimeter objects associated with more than three tracks, the calorimeter information is used.

The more complicated 1-to-2, 1-to-3, 2-to-1 and 2-to-2 track-island matches are treated in the same way as the 1-to-1 matches, with the following replacements:

- $E_{\mathrm{CAL}} \to \sum_i E_{i,\mathrm{CAL}}$ and i runs over the calorimeter islands;
- $p \to \sum_j p_j$ and j runs over the matched tracks;
- $\sigma_{E_{\mathrm{CAL}}} \to \sqrt{\sum_i (\sigma_{E_{i,\mathrm{CAL}}})^2}$;
- $\sigma_p \to \sqrt{\sum_j (\sigma_{p_j})^2}$.

5.3.2. Cone Island Correction

Further energy corrections are applied to the cone islands and EFOs:

- **Dead material correction:** Corrections for energy loss due to dead material on the detector have to be applied. A detailed dead material map (Figure 5.4) is used to correct the contributions to the energy loss in front of the inner CAL surface.
- **Calorimeter cr** are not very well
- **Energy overest** with momenta b hadronic interact 0.6. This causes has to be correct

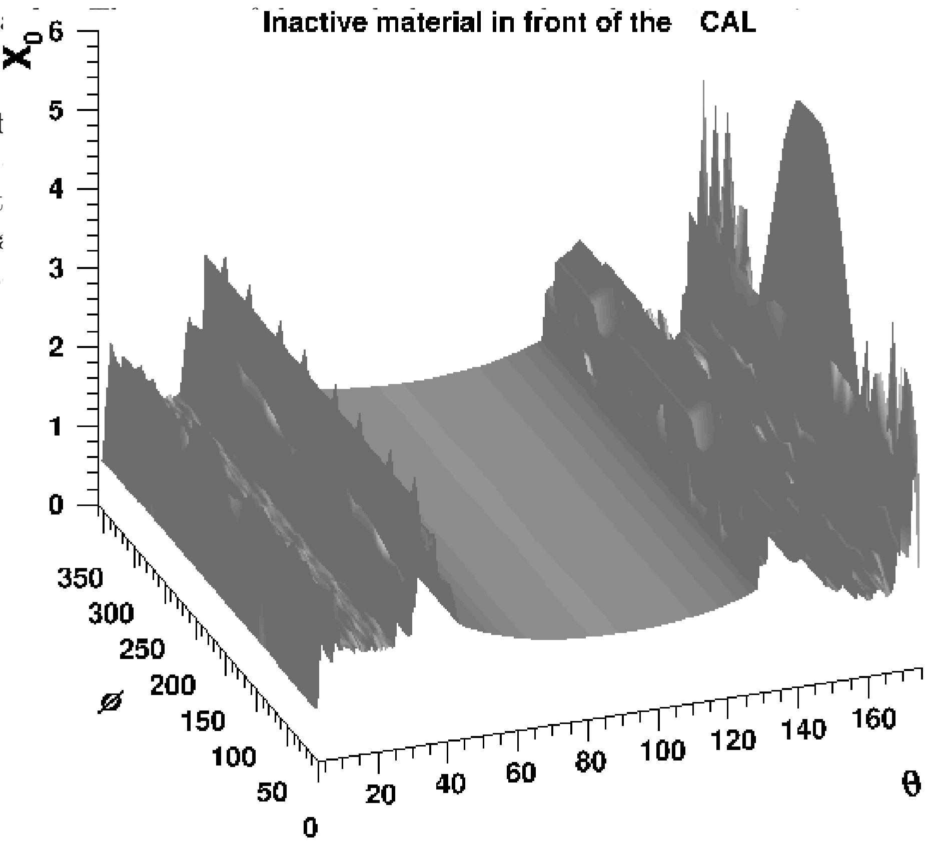

Figure 5.4: Map of the dead material distribution between the interaction region and the calorimeter as a function of θ and ϕ. The contribution varies between one and three radiation lengths, X_0.

5.3.3. Correction for the Presence of a Muon

The reconstruction of the hadronic system of an event only from the calorimeter would underestimate the energy in the presence of a muon. In the case of identified muons[2] (see Section 5.5), the energy is corrected to the full energy using the track

---

[2] The muons are associated to the EFOS using the muon track information in the CTD.

momentum of the muon. Isolated muons are corrected using the track information rather than the CAL MIP cluster, as described in Section 5.3.1. For non-isolated muons this cannot be done, as there is also hadronic activity in the EFO. The EFO is then corrected by subtracting the typical muon energy loss and adding the muon momentum measured in the CTD. The typical energy deposit of a muon in the CAL calculated as a function of the polar angle θ from a single muon MC is shown in Figure 5.5.

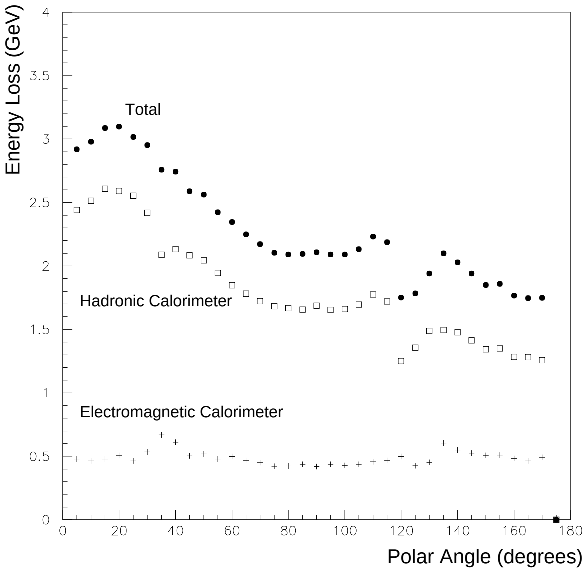

Figure 5.5: Typical energy loss of a muon in the CAL as a function of the polar angle θ. The crosses represent the energy loss in the electromagnetic, the open circles the energy loss in the hadronic calorimeter and the full points the total energy loss [64]. The differences in the energy loss for different polar regions are due to the different amount of material the muon has to pass. At about $\theta = 20^\circ$ and $\theta = 120^\circ$ are the so-called super cracks, the regions between the different calorimeter sections and hence less material.

The following classes of muons are corrected:

- if the EFO already uses the track information for the energy determination no correction is needed, as the muon properties are already taken into account;
- if the EFO uses the CAL information for the four-vector determination and the energy is less than 150% of the typical energy loss of a muon, $E_{\mathrm{EFO}} \leq 1.5 E_{\mathrm{MIP}}$, the four-vector is determined from the measured muon momentum;
- if the EFO uses the CAL for the four-vector determination and the energy deposit is larger than 150% of the typical energy loss of a muon, $E_{\mathrm{EFO}} > 1.5 E_{\mathrm{MIP}}$, a MIP is subtracted and the reconstructed muon vector added to the initial EFO.

5.4. Jet Reconstruction

The properties of the partons in the hard interaction are strongly correlated with the hadronic system originating from the hadronisation/fragmentation process. This system is represented by a large amount of energy deposited in a small angular region, also called a jet of hadrons. In this analysis the jets are reconstructed from the EFOs defined in Section 5.3.

As jets are complex objects not uniquely defined in QCD and their definition relies on the implementation of the jet algorithm, the Snowmass workshop in 1990 fixed criteria to define standards for jet finders [65] to guarantee their universal applicability.

A jet finder especially suited for *ep* collisions should fulfill the subsequent requirements:

- **Collinear safety:** The results should be independent of the fact that a parton can split into two partons moving collinearly. This dependence would cause collinear divergencies in the theoretical calculations, which disappear if no distinction is made between two particles having the energy $E_1 + E_2 = E$ and a single particle of energy E; this means experimentally that the jet algorithm should not depend on the detector granularity;

- **Infrared safety:** The results should be independent of the emission of low energy particles, which would lead to infrared divergencies in the theoretical calculations; this means for the experimentalists that small energy deposits, related to noise have to be removed;

- **Beam remnant:** The first two points are common to all experimental environments. In *ep* photoproduction one has to treat in addition the remnants from the proton and the photon, which have to be separated from the jets and should not influence them;

- **Lorentz invariance:** The frames of physical interest are usually Lorentz boosted along the beam direction. Therefore the jet algorithm should be independent such transformations, realised by running the jet algorithm in the $\eta - \phi$ plane.

k_t Clustering Algorithm

In this analysis a k_t-type clustering algorithm [66, 67] is used. The clustering algorithm has the advantage of unambiguously assigning the EFOs to a jet, i.e. the treatment of overlapping jets is clear, and the assignment of hadrons to jets can be done in the same way in theoretical calculations and experiments. The separation depends on the relative transverse momentum of the combined objects. By this an effective jet radius is defined depending on the energy of the jet. Three things have to be specified for the clustering procedure:

- a test variable (energy-angle resolution), d_{kl}, has to be defined in order to decide if two hadrons belong to the same cluster or not;

- a recombination scheme, which defines the iterative formation of jets from single particle entries in the EFO list;
- a hard scattering scale, d_{cut}, to separate hard and soft processes.

The KTCLUS algorithm used here, uses the following procedure for jet formation:

1. The resolution variables d_{kl} and d_k, d_l are calculated for all pairs of EFOs e_k and e_l:

$$\begin{aligned} d_k &= (p_T^k)^2 \ , & (5.4) \\ d_{kl} &= \min((p_T^k)^2, (p_T^l)^2)\Delta R_{kl}^2 \ , & (5.5) \end{aligned}$$

   where $\Delta R_{kl}^2 = \frac{(\eta_k - \eta_l)^2 + (\phi_k - \phi_l)^2}{R^2}$ guarantees the longitudinal boost invariance. R is a measure of the distance between two candidates and set to 1 in this thesis.

2. The smallest value for each of the resolution variables d_k, d_{kl} is determined:

   - If d_{kl} has the smallest value, the two EFOs e_k and e_l are combined into a *pseudo-particle* using the *E recombination scheme*. In this scheme the hadrons are treated as massive particles, assuming a pion mass. Their four-momenta are added as: $p_{(kl)} = p_k + p_l$. The new resolution variables for this pseudo particle are:

$$\begin{aligned} d_{(kl)} &= (p_{T,(kl)})^2 \ , & (5.6) \\ d_{(kl)i} &= \min((p_{T,(kl)})^2, (p_{T,i})^2)\Delta R_{(kl)i}^2 \ . & (5.7) \end{aligned}$$

   - If d_k has the smallest value, the EFO e_k is removed from the EFO list and included in a so-called *remnant jet*. The decision if the particle is part of the proton or photon remnant jet is based on the resolution variables $d_{kp} = (p_T^k)^2 \Delta R_{kp}^2$ and $d_{k\gamma} = d_{k\gamma} = (p_T^k)^2 \Delta R_{k\gamma}^2$.

3. The combination procedure continues until all particles and pseudo-particles not included in the remnant jet have a separation larger than the cut-off scale, d_{cut}. In this analysis, a cut-off scale of $d_{cut} = 1\,\mathrm{GeV}$ was chosen.

The result of this procedure are final-state jets and remnant jets. The E recombination scheme is chosen as the mass of beauty quarks is not negligible.

5.5. Muon Reconstruction

The muon reconstruction system is especially important for this analysis, as the decay muon from the beauty quark is used to tag beauty events. A highly efficient muon reconstruction with a good signal to background ratio has been achieved due to the redundancy of the muon signature measured in several components of the ZEUS detector. First the main features of muon signatures are described, then the different muon reconstruction algorithms are presented. In the last part the method used to combine them into a general muon finder, is described. For more details see the description of the GMUON package [68].

5.5.1. Muon Signature

The main characteristic of a muon relevant for its detection is that it is a charged minimum ionising particle with high penetration power. A rough rule of thumb for this penetration power is

$$\text{range of muon in iron} \sim 1\,\text{m/GeV}.$$

Four main features are used in ZEUS to identify muons from semi-leptonic beauty decays:

1. As muons are charged particles a track can be reconstructed and its momentum determined, using the tracking devices.
2. Muons from beauty decays are produced very close to the primary vertex of the *ep* collision. Given the resolution of the CTD, they are associated to the primary vertex. This requirement reduces the background from kaon and pion decays in flight.[3]
3. Due to the minimum ionising property, high-energy muons are not stopped in the CAL. They leave a relatively small amount of energy along their trajectory in the CAL and reach the muon chambers where they can be identified as charged tracks.
4. Muons from heavy-flavour decays are accompanied by hadrons and are thus non-isolated.

5.5.2. Muon Reconstruction Algorithms

MUONFIND

The MUONFIND [69] algorithm (also referred to as MIP in GMUON) is a simple algorithm matching CTD tracks to calorimeter islands, which are compatible with a MIP signature. It is only used for high momentum tracks ($p_t > 2\,\text{GeV}$).

MV

The MV muon finder [70] is a CAL based muon finder, like MUONFIND. The difference from MUONFIND is a more sophisticated algorithm, based on a neural network to check the compatibility of the clusters with a MIP cluster. It assigns a MIP probability to the cluster, which also includes matching information. The muon candidate is then matched to a CTD track. For very forward muons the possibility to run the algorithm without track matching exists. MV is the best purely CAL-based muon finding algorithm and suited for isolated muons down to $p > 1\,\text{GeV}$.

---

[3] In HERA II the MVD enables the possibility to determine the secondary vertex from the B meson decay. Muons could then be associated to this secondary vertex.

GLOMU

The GLOMU algorithm [71] provides simple matches based on distance and angle between CTD tracks and inner, outer or inner+outer muon chamber tracks (BRMUON tracks). It also provides a match to MIP clusters, but less sophisticated than the MV algorithm. Several versions of this algorithm exist, on trigger level and offline. This algorithm is also more suited for low background environments. It can almost always be replaced by the BREMAT algorithm, which has a better background rejection.

BREMAT

The BREMAT muon finder [72] reconstructs muons by matching track candidates from the inner, outer or inner+outer barrel and rear muon chambers with CTD tracks. The tracks are extrapolated to the inner muon chamber plane using GEANE [73] taking into account the full error matrix for the matching χ^2 to evaluate a true matching probability. The matching is done in position and angle in two projections (4 degrees of freedom). If also the outer muon chambers are considered the muon momentum can be estimated, as the muon is bent due to the magnetic field in the iron yoke. The muon momentum is then also taken into account for the matching, yielding an additional degree of freedom. The final muon momentum is taken from the more precise inner tracker information only. The CTD tracks used in the BREMAT algorithm have to pass a preselection, the most important requirements are:

- momentum, $p > 1\,\text{GeV}$;
- track starting from CTD super-layer 1 and extending to at least super-layer 3, polar angle, $\theta > 20\,^{\circ}$;
- χ^2 per number of degrees of freedom, $\chi^2_{ndf} < 5$;
- distance, Δ, between the central point of the muon chamber segment and a straight line extrapolation of the CTD track to the muon chambers $\Delta \leq 150\,\text{cm}$.

The BREMAT algorithm is particularly suited for non-isolated muon studies and hence is one of the main muon finders used in this analysis.

MUBAC

The MUBAC algorithm [74] reconstructs muon segments from the BAC pad and strip information, (see Section 4.5.3). In the context of GMUON (see section 5.5.3) the central tracks are extrapolated from the vertex using a straight line into the BAC and a distance-based matching requiring as distance of closest approach of 50 or 120 cm.

Due to large geometrical coverage of the BAC the muon finding efficiency is substantially increased. The MUBAC algorithm is a valuable supplement to other muon finders for analyses which aim for maximal efficiency rather than maximal background rejection, such as a semi-leptonic muon analysis.

MAMMA

The MAMMA algorithm [68] matches isolated muons with a MIP signature to an inner forward muon chamber segment. Since the background is very high in the forward region, this finder is only useful for low background analyses with well-isolated muons.

MCTS

MCTS segments are obtained by combining a simplified curved spline fit in the FMUON system with a straight line fit through the CAL and the CTD towards the primary vertex, including an estimation of the muon energy loss. Thus a rough momentum estimation at the vertex using FMUON information only can be done. This algorithm has a high FMUON efficiency for very forward muons, but produces at the same time many fake candidates. This muon finder is more intended for technical studies than for physics analysis, but nevertheless it can reduce the background in the MV or MUBAC muon finders.

MPMATCH

The MPMATCH algorithm [75, 76] is one of the most sophisticated muon finding algorithms available. It provides a combined Kalman filter fit [77] of an FMUON segment with a CTD track coming from the primary vertex. The tracks are extrapolated, as for the BREMAT algorithm, using the GEANE package. The muon momentum is determined from the combined track measurement. The requirement on the CTD tracks are minimal and no CAL or BAC information is used within MPMATCH.

MPMATCH has a very good background rejection and therefore no requirements on the muon isolation. Thus it is very well suited for a semi-leptonic beauty analysis. Unfortunately the geometrical coverage is small and the efficiency only moderate.

MUFO

The MUFO algorithm [78] is an algorithm similar to MPMATCH and has been developed in parallel. It has two main options for the muon finding:

- The first possibility is essentially identical to MPMATCH: it provides a Kalman filter fit between an FMUON segment, a central track and the primary vertex. It produces almost the same muon candidates as MPMATCH.

- In the second mode it matches a FMUON segment with the primary vertex without requiring a CTD track. This mode yields additional muon candidates in the very forward region, but produces also a higher background than MPMATCH, as no central track is required.

5.5.3. A General Muon Finder

For the best reconstruction of muons with the highest possible efficiency and the lowest background, all information on muon candidates from the different detector components should be combined into just one muon object. This is the aim of the general muon finder package, GMUON [68]. It combines all finders described in the previous section. As each finder described above is only applicable for a certain type of muon candidate, e.g. isolated muons, forward muons, high or low p_T muons etc. the combination of all finders reduces these limitations substantially. Due to the redundancy and the larger geometrical coverage, either the number of muon candidates can be increased by a large factor, or the background can be reduced, depending on the aim of the physics analysis.

GMUON can either be used as a front-end to the different muon finders or, in addition, one can take advantage of the redundancy and can improve the signal-to-noise ratio (S/N). Therefore a quality factor for the muon candidates, ranging from 0 (worst S/N) to six (best S/N), has been evaluated using a beauty and a light flavour MC sample, such that the signal-to-background ratio increases approximately by a factor of two for each unit of quality. For each muon candidate in GMUON, the information from all individual finders and the muon quality evaluated from the finder combination is stored. An overview of the muon quality used in this analysis (quality 4 to 6) from the different finder combinations is given in Table 5.3. The complete Table can be found in Appendix A.

Muon Quality Modification

The muon quality flag was evaluated using a beauty and a light flavour MC sample. Hence for the optimisation, the signal refers to semi-leptonic beauty decays and the background refers to background muons (see Section 8.1) in beauty events. This definition is appropriate for a semi-leptonic muon analysis. However the standard muon quality can only serve as a first indication and the muon selection has to be checked individually for every class of analysis.

For the semi-leptonic beauty analysis some corrections to the muon quality were necessary. Studies on real data for muon finder combinations with a quality of 4 or higher showed that, especially in the forward region, the background level in real data was higher than assumed from the MC studies, due to secondary particles from the proton remnant entering the muon chambers and beam-induced detector noise. To take this into account, the default quality is reduced depending on the finder combination used. The probability to create fake muon tracks apparently pointing to the vertex increases with a decreasing number of FMUON planes used for the muon reconstruction. For less than five planes the quality is therefore reduced. Due to detector inefficiencies not all FMUON tracks start at the innermost FMUON plane. For these tracks the fake contamination is found to be substantially higher and the quality was reduced for these muons.

A large fraction of the additional background is not correlated with measurements in other detectors. Hence an independent confirmation of the muon in a different detector component reduces substantially the additional background and the quality is raised again, if in addition to the FMUON the muon was reconstructed by another component (CAL or BAC). Also the forward part of the BAC detector was found to be much more affected by background than assumed from the MC. Consequently the quality is reduced, if in the forward region the muon was found by the BAC but not by the FMUON. The exact numbers of the quality changes are summarised in Table 5.2. The final quality is not allowed to exceed the original quality from the standard definition, as these quality changes are only meant to account for additional background sources.

Quality Modification	Finder Conditions
± 0	number of FMUON planes used > 4
-2	number of FMUON planes used $= 4$
-4	number of FMUON planes used < 4
-1	no hit in innermost FMUON chamber
$+1$	muon also reconstructed by MUBAC
$+2$	muon also reconstructed by MV
-1	muon only found by MUBAC

Table 5.2: Modifications to the default muon quality. If the resulting value exceeds the default quality, it is set back to its old value.

Muon Efficiency Corrections

The muon chamber efficiency in the MC simulation differs quite a lot from the efficiency in real data. As the efficiency is essential for the precise measurement of the cross-section, these differences have to be evaluated and the MC distributions have to be corrected to correspond to the data efficiency. The efficiency correction procedure follows the approach [79] used for the efficiency corrections in analyses using BREMAT and MPMATCH only.

The muon efficiencies in the different detector components BAC, FMUON and BMUON have to be measured in data and MC. This is done by selecting dimuons coming from the Bethe-Heitler (BH) process $ep \rightarrow ep\mu^+\mu-$ and from J/Ψ decays into muons, see Figure 5.6.

These processes have a simple and easy topology of two isolated muons. This assures that the muon chamber and BAC efficiencies do not depend on the production process, while accounting for detector (in)efficiencies. The difference in the track matching probability for isolated and non-isolated muons usually changes only the GMUON quality within the cut range of 4 to 6. Details about the selection and the samples used for the determination are given in [80].

The MV finder is dedicated to isolated muons and uses only the CTD and CAL. The CAL is well simulated and is independent of the muon chambers and the BAC.

Qual.	Finder Combination	CTD match	Match DCA cut	Vtx ass.	MIP prob.	Mom.[GeV] or rap.
6	BREMAT 5dof	yes	> 0.01	yes	-	-
	MPMATCH or	yes	> 0.05	-	-	-
	MUFO	yes	> 0.05	-	-	-
	MPMATCH +MV	yes	> 0.01	-	> 0.6	$p > 1$
	MUFO + MV	yes	< 0.05	-	> 0.6	$p > 1$
5	BREMAT 4dof + MV	yes	> 0.01	yes	> 0.6	$\|\eta\| > 0.6$
	MUBAC + MV	yes	-	yes	> 0.6	$\|\eta\| > 0.6$
	MUBAC+BREMAT 4dof+MV	yes	> 0.01	yes	> 0.6	$\|\eta\| < 0.6$
	MUBAC+BREMAT 5dof+MV	yes	> 0.01	no	> 0.6	-
	MPMATCH or	yes	> 0.01,	-	-	-
	MUFO	yes	< 0.05	-	-	-
	MAMMA+CTD	yes	-	-	impl.	-
4	BREMAT 4dof	yes	> 0.01	yes	-	-
	MUBAC	yes	50 cm	yes	-	-
	MUBAC+MV	yes	120 cm	yes	> 0.6	$\|\eta\| < 0.6$
	MUBAC+MIP	yes	120 cm	-	impl.	-
	MUFO other vtx	no	-	yes	-	-
	MCTS + MV	no	-	no	-	-
	MAMMA + vtx	no	-	yes	impl.	-

Table 5.3: Definition of the standard GMUON quality. A matching probability cut is applied in the case of the muon chambers and a DCA cut in cm in the case of the BAC. The column Vtx ass. indicates, whether the the CTD track has to be assigned to the primary vertex.

The MV finder is therefore used as the reference for the efficiency determination. The efficiency is determined in bins of p_T^μ and η^μ. To eliminate a bias from the event trigger, events that are triggered only by muon triggers receive a special treatment:

- if only one muon triggered the event, it is excluded from the efficiency calculation and only the second muon is used;
- if both muons triggered the event, both muons enter the efficiency calculation;
- if none of the muons triggered, both are used for the efficiency determination.

As indicated in Table 5.3, within GMUON the algorithms MUBAC, BREMAT and MPMATCH are used in two different configurations, therefore the efficiencies have to be determined for both configurations separately. The configurations are denoted as *loose* and *tight*, depending on whether the muon was also found by MV or not. They are defined by:

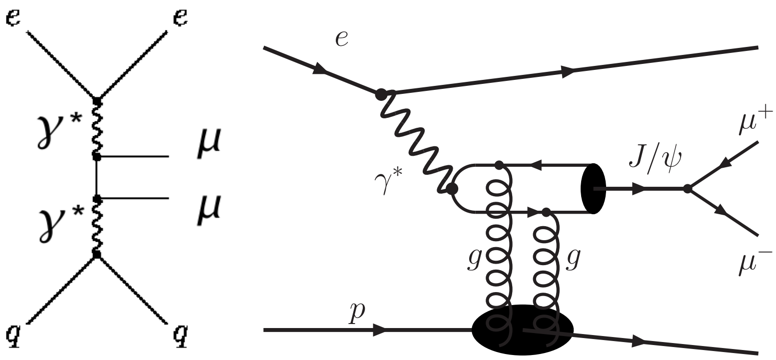

Figure 5.6: Feynman diagrams for dimuon production coming from the Bethe-Heitler (BH) process (left) and J/Ψ decays (right)

- MUBAC: DCA cut of MUBAC hit to the extrapolated track $\leq 50\,\text{cm}$ for the tight configuration and $\leq 120\,\text{cm}$ for the loose;
- BREMAT: matching probability ≥ 0.01 for the tight, no cut for the loose;
- MPMATCH: matching probability ≥ 0.05 for the tight, ≥ 0.01 for the loose.

The two-dimensional histograms of the correction factors for the different finders used in this analysis are shown in Appendix B.

Application of the muon efficiency correction factors

For the application of the correction factors, the result from each finder is corrected for each muon candidate. If the candidate still fulfills the muon quality requirements it is kept. For this, each single finder correction factor is interpreted as a survival probability rather than an event weight. Practically this means that a random number is generated following a flat distribution between 0 and 1 and the event is kept if that random number is below the value of the correction factor.

The advantage of this procedure compared to a weight-based correction is that it does not depend on the finder combination used to identify the muon and it does not depend on the number of muon candidates per event. It should automatically yield the correct fraction of any particular finder combination. The resulting finder combination can therefore be compared directly to the data. The disadvantage of this method is that it relies on random numbers, which can lead to different results from the same MC sample. Furthermore, this method can only be applied to correction factors lower than 1, as it is not possible to create additional muons. Additional muons could be found, if the corrections already applied on reconstruction level, are on average correct, but overcorrect in some regions of phase-space and undercorrect in others. To avoid this problem, all available corrections were not applied on the intermediate reconstruction level, but instead were taken into account by the efficiency corrections evaluated after the reconstruction.

6. Event Selection

In this analysis beauty production is measured in photoproduction in the semi-leptonic muon decay channel by requiring the presence of a muon and at least two high p_T jets. The data and MC samples are introduced and then the event selection is described in detail. The chapter finishes with a summary of the applied offline cuts.

6.1. Data Samples

The available data samples for the different running periods are summarised in Table 6.1. The integrated luminosities from the ZEUS luminosity measurement and the colliding particles are given for each running period. The lepton beam energy was always 27.5 GeV, while the proton beam energy was raised from 820 to 920 GeV in 1998. As the muons are an important ingredient for this analysis, runs with bad barrel/rear muon chamber conditions have been identified and removed from the list of available runs. For the FMUON, the runs with bad FMUON chamber conditions have been identified as well, the FMUON information is not considered in these runs instead of removing the run. This is corrected for in the muon efficiency corrections, explained in Section 5.5.3.

Running Period	Hadron	Lepton	CMS Energy [GeV]	Int. Lumi. [pb^{-1}]
1996-1997	p	e^+	300	37.6
1998-1999	p	e^-	318	15.9
1999-2000	p	e^+	318	60.2

Table 6.1: Overview of the data samples for the different running periods.

For the event simulation, needed to unfold the cross-section, the PYTHIA6.2 event generator described in Section 2.5 is used. The number of events simulated and the corresponding QCD processes are summarised in Table 6.2. The simulation was done separately for the beauty signal, for charm and for the light flavour (u, d, s) background. The beauty and the charm samples are split further into direct, resolved and excitation in photon/proton processes. For the light flavour, only the direct and resolved processes were generated separately, the excitation processes are in this case part of the resolved sample. An overview of the processes contained in each subsample is given in Appendix C. For all samples the proton structure function CTEQ-4L [81] and the photon structure function GRV-LO [82] were used. For the signal Monte Carlo samples the beauty and charm quark mass parameters were set to

$m_b = 4.75\,\mathrm{GeV}$ and $m_c = 1.35\,\mathrm{GeV}$, while the masses in the inclusive sample used for light flavour were set to $m_q = 0\,\mathrm{GeV}$. The time and disk space consumed by the event simulation is not negligible. Care has to be taken to reduce the samples to manageable numbers of events by preselection cuts on the generated hadronic final state. While the beauty signal MC is totally inclusive, the charm sample has a considerably higher cross-section. Therefore a preselection of one muon with $p_T > 1.5\,\mathrm{GeV}$ has been applied. Due to the preselection on muons, the hadronic background coming from charm is not included in the sample. It is assumed to be indistinguishable from the light flavour background. For the fake muon background coming from light flavour, in the inclusive sample two jets with $E_t > 4\,\mathrm{GeV}$ are required.

Flavour	Process	σ[nb]	Luminosity[pb^{-1}]
b	direct γp	4.08	693.5
b	resolved γp	0.82	716.0
b	excitation in γ	1.50	674.5
b	excitation in p	0.31	792.8
c	direct γp	48.95	645.4
c	resolved γp	2.76	686.4
c	excitation in γ	87.85	641.7
c	excitation in p	15.06	675.1
u, d, s, c, b	direct γp	87.41	385.6
u, d, s, c, b	resolved γp	443.40	333.3

Table 6.2: Monte Carlo Samples. The samples for light flavours were taken from a large inclusive sample containing all flavours, using only light flavour events. The events are simulated in blocks for different trigger and detector configurations and vertex distributions according to the situation in real data taking.

6.2. Trigger

The data samples have been selected using a three-level trigger system (see Section 4.7) to record mostly physics interactions and to reduce the number of background events. The trigger system is also simulated in the detector simulation. The trigger selections can therefore be applied to data and Monte Carlo in the offline analysis, in order to emulate the online trigger. A summary of the trigger selection is given in Table 6.3 and the details of the different trigger slots are given in Appendix D. Figure 6.1 shows a comparison between the data and MC for the selected events.

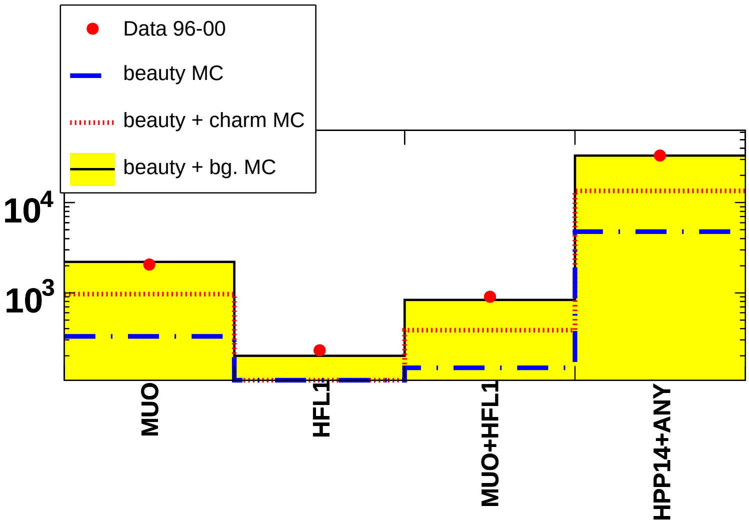

Figure 6.1: Comparison of data and MC of the different trigger combinations used in the analysis. The agreement is very good and no corrections on analysis level have to be applied. MUO means here the sum of the muon triggers MUO3, EXO11, EXO12. “bg” is background from charm and light flavour.

6.3. Kinematics of Photoproduction Events

Photoproduction events are characterised by a very small scattering angle of the photon. One possibility to select photoproduction events is therefore to require that no scattered electron is reconstructed in the main detector. This has the advantage of much more statistics to compensate for the small beauty cross-section compared to tagged photoproduction using the electron taggers along the beam-line with a small geometric coverage. The average Q^2 of such events is $Q^2 = 10^{-3}\,\mathrm{GeV}^2$ with a maximal virtuality of $Q^2 = 4\,\mathrm{GeV}^2$ [83]. As the scattered electron is not detected, the photon energy can not be derived from the scattered electron energy, but has to be calculated from the final state hadrons, which on reconstruction level are the energy flow objects (EFOs) introduced in Section 5.3. This method is referred to as the “Jacquet-Blondel method” [84]:

$$y = \frac{1}{2E_e} \sum_{i\epsilon EFOs} (E_i - P_{z,i}) \ , \tag{6.1}$$

where E_e is the energy of the incoming electron. As explained in Section 5.3 many corrections have already been applied to the EFOs. The correlation between the true and the reconstructed value of y see Figure 6.2 is good, and no further correction is applied.

To reconstruct electron candidates, the SINISTRA electron finder is used [85]. SINISTRA analyses energy deposits in the electromagnetic and hadronic parts of the CAL and distinguishes between electromanetic and hadronic clusters. In the first part of the algorithm, a neural network determines the probability for a cluster to be electromagnetic, while the second part selects the scattered electron from a

Running Period	Description	Summary of Requirements
96-99	low E_T dijet trigger (HPP14)	at least two jets with $E_T \geq 4\,\text{GeV}$ and $\|\eta\| < 2.5$
99-00	low E_T dijet trigger (HPP14)	at least two jets with $E_T \geq 4.5\,\text{GeV}$ and $\|\eta\| < 2.5$
96-00	barrel/rear muon trigger (EXO 11/12)	at least one barrel or rear muon reconstructed with the GLOMU algorithm (see Section 5.5.2)
96-00	semi-isolated muon trigger (MUO3)	at least one semi-isolated muon found in the barrel and rear muon chambers
99-00	muon plus dijet trigger (HFL1)	at least one muon found by GLOMU and two jets with $E_T \geq 3.5\,\text{GeV}$ and $\|\eta\| < 2.5$

Table 6.3: Third level trigger selection. Details are given in Appendix D.

list of electromagnetic clusters. SINISTRA gives as output the probability, P, the energy of the scattered electron determined by the CAL measurement, E_{cand}, and the inelasticity calculated using the electron method:

$$y_{el} = 1 - \frac{E_{cand}}{2E_e}(1 - \cos\theta_{cand}) \ , \tag{6.2}$$

where θ_{cand} the polar angle of the electron candidate. The event is rejected if the candidate with the highest probability fulfills:

$$\begin{aligned} P &> 0.9 \ ; \\ E_{cand} &> 5\,\text{GeV} \ ; \\ y_{el} &< 0.9 \ . \end{aligned} \tag{6.3}$$

The latter two cuts prevent the electron veto from rejecting photoproduction events, if another particle was misidentified as a DIS electron. This can be the case for final state pions, electrons or photons and typically results in a large electron method inelasticity, which does not correspond to the inelasticity of the event. Hence, events with a high electron candidate inelasticity and a considerable amount of energy deposited in the electromagnetic CAL are not excluded from the selection.

Further suppression of the residual DIS events is achieved by a cut on the inelasticity reconstructed with the Jacquet-Blondel-Method, Equation 6.1. For DIS events the longitudinal momentum $\sum_i(E_i - P_{z,i})$ is conserved and expected to be around two times the energy of the incoming electron. Therefore a y_{JB} of 1 is expected for DIS events and a cut $y_{JB} < 0.8$ applied to clean further the sample. For proton-induced beam-gas events the produced particles have a small polar angle so that

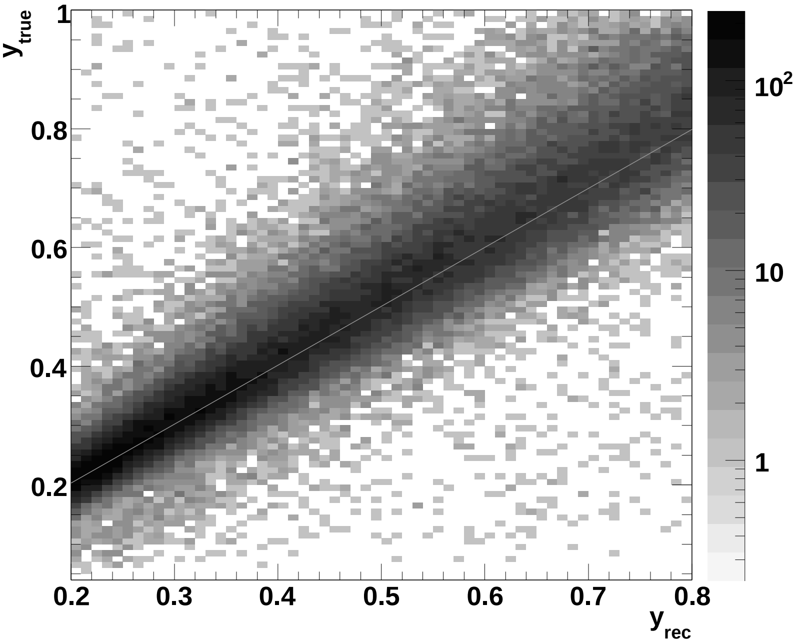

Figure 6.2: Comparison of y reconstructed with the Jacquet-Blondel method, y_{rec}, and the true inelasticity, y_{true}, in $b\bar{b}$ direct photoproduction. The light-grey line represents the bisecting line.

$\sum_i(E_i - P_{z,i}) \rightarrow 0$. Hence a minimal y_{JB} of 0.2 is required in the selection. Further cleaning is done with a cut on the Z-position of the primary vertex $|\mathrm{Z}_{Vtx}| < 40\,\mathrm{cm}$, which is about 4 times the width of the vertex distribution.

The true Q^2 distribution before and after all selection cuts summarised in Section 6.8 in the different MC samples for signal and background is shown in Figure 6.3. The contamination with events from the DIS regime is about 1.2% for beauty, 3.3% for charm and 0.4% for light flavour.

6.4. Muon Selection

The muon selection is done using the general muon finder GMUON described in Section 5.5.3. Due to the redundancy from the different finders it was possible to lower the muon p_T cut compared to previous analyses from $p_T^\mu = 2.5\,\mathrm{GeV}$ to $p_T^\mu = 1.5\,\mathrm{GeV}$. To reach the outer muon chambers a minimum p_T^μ of $2.5\,\mathrm{GeV}$ is necessary, which was required in the previous analysis of 96-00 data, where only BREMAT and MPMATCH were used for the muon identification. Together with the larger geometrical coverage using the BAC the number of selected events has been increased by a factor 10 and the number of selected beauty events by a factor of 7.5.

Applying the complete selection, given at the end of this Chapter, on an isolated

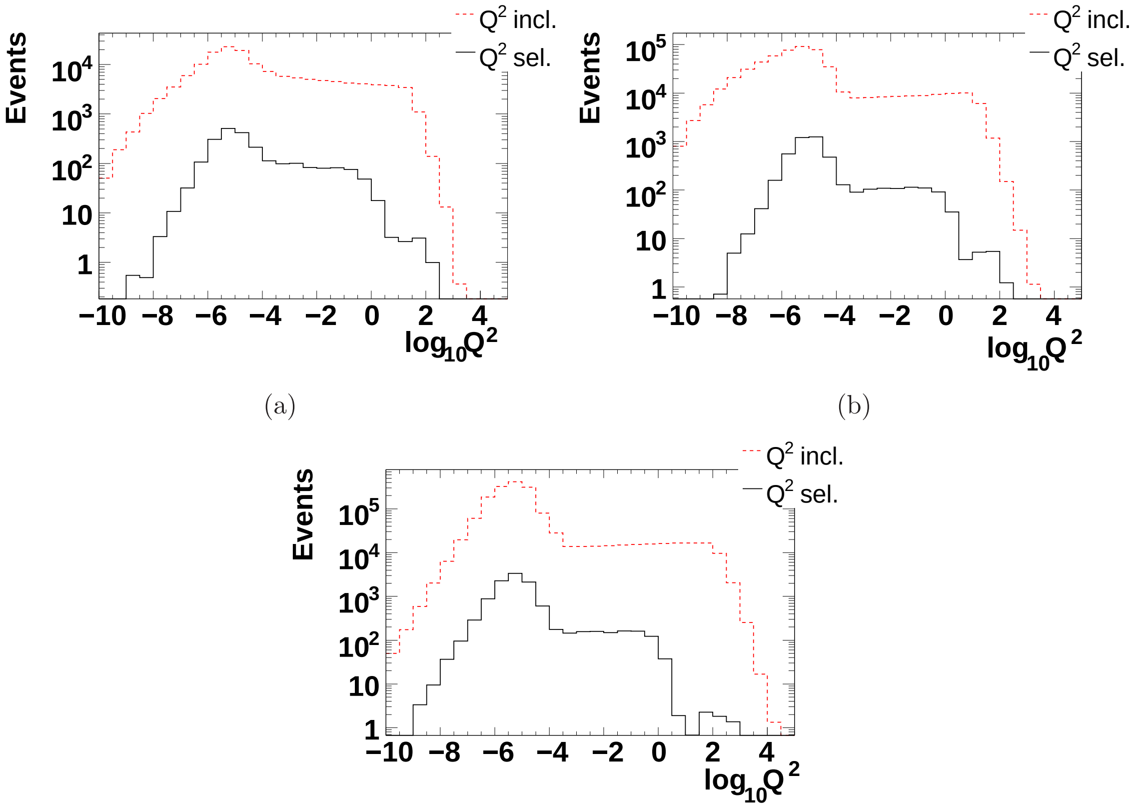

(a)

(b)

(c)

Figure 6.3: True Q^2 distribution in the different MC samples, (a) beauty, (b) charm and (c) light flavour before and after the selection.

dimuon and a Bethe-Heitler MC sample many events with a very high unphysical transverse momentum with respect to the jet (p_T^{rel}, see Section 7.1) survived the selection. Therefore an anti-isolation cut has been applied, summing up the EFO transverse momentum in a cone of
$\Delta R = \sqrt{(\phi^{EFO} - \phi^{\mu})^2 + (\eta^{EFO} - \eta^{\mu})^2} = 1$ around the muon, subtracting the muon EFO. Good muons are required to pass the following cuts:

$$\text{GMUON quality} \geq 4\ ; \tag{6.4}$$

$$p_T^{\mu} \geq 1.5\,\text{GeV}\ ; \tag{6.5}$$

$$-2.0 < \eta^{\mu} < 2.5\ ; \tag{6.6}$$

$$p_{T,\Delta R=1}^{EFOs} > 0.5\,\text{GeV}\ . \tag{6.7}$$

All muons are required to have a vertex-track association due to the implicit requirement on the EFO association, see Section 6.5. For the muon quality, the quality modifications described in Section 5.5.3 are applied as well as the muon efficiency correction described in the same Section. The muons are classified as forward, rear and barrel muons following the geometrical structure of the detector:

$$\begin{aligned} &\text{rear} & -2.0 < \ & \eta^{\mu} & \leq -0.9\ ; \qquad (6.8)\\ &\text{barrel} & -0.9 < \ & \eta^{\mu} & \leq 1.2\ ; \qquad (6.9)\\ &\text{forward} & 1.2 < \ & \eta^{\mu} & \leq 2.5\ . \qquad (6.10) \end{aligned}$$

Figure 6.4 shows the comparison between data and MC for every possible finder combination. As a result of the efficiency correction the agreement is satisfying. The remaining differences are treated in the systematic error for the muon efficiency calculation.

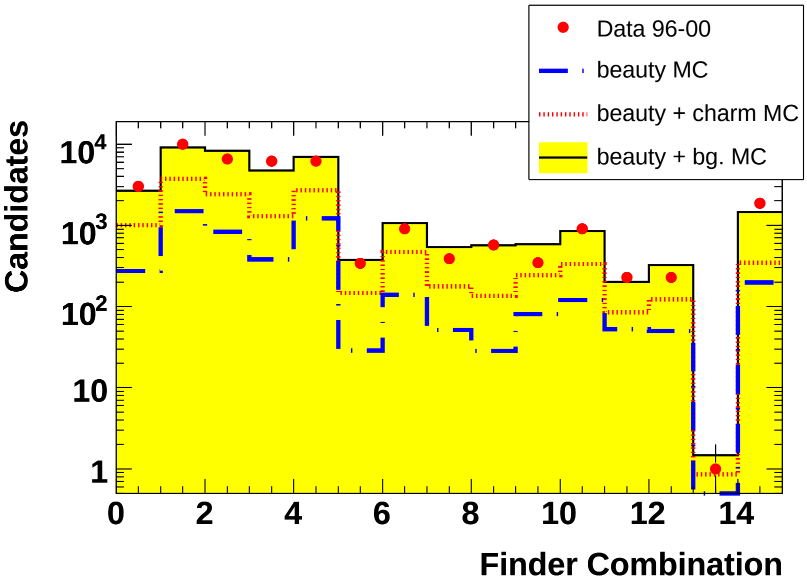

Figure 6.4: Comparison of data and MC for the different muon finders. Bins 0 to 4 are the combinations for the Barrel: BREMAT+MUBAC (0), BREMAT+MUBAC+MV(1), BREMAT only(2), MUBAC only (3), MUBAC+MV (4), bins 5 to 9 are the same combinations for the rear and bins 10 to 14 describe the finder combinations for the forward region, replacing BREMAT by MPMATCH or MUFO.

The kinematic distributions of the muon: its transverse momentum, p_T^{μ}, and the pseudo-rapidity, η^{μ}, are shown in Figure 6.5. p_T^{μ} is well described and the gain of events due to lowering the p_T^{μ} cut can be seen. In the η^{μ} distribution a systematic shift of the data versus the MC is observed. This shift has been seen in all heavy-flavour analyses using semi-leptonic decays into muons to tag the heavy flavour at ZEUS. This could happen, if the non-direct processes are underestimated in the Monte Carlo, see also Section 6.6.

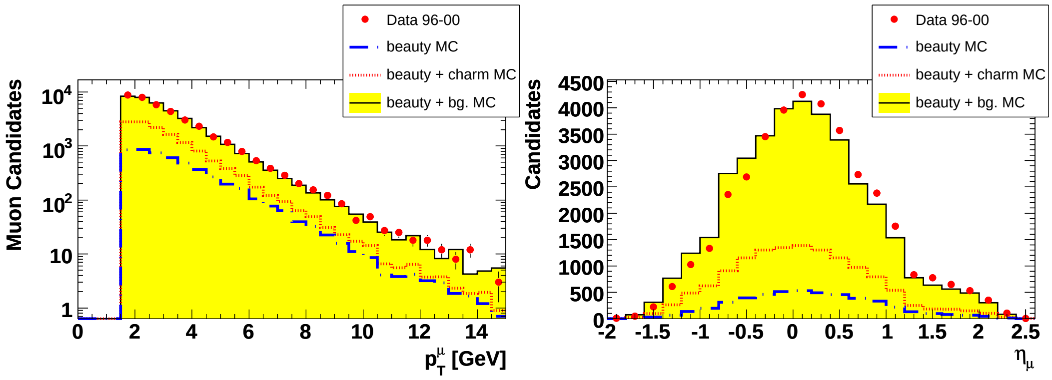

Figure 6.5: Comparison of data and MC for the muon transverse momentum, p_T^μ, on the left and η^μ on the right. p_T^μ is well described by the Monte Carlo, while a shift in the η^μ distribution is observed.

6.5. Jet Selection

Jets are reconstructed using the KTCLUS algorithm (see Section 5.4) in the longitudinal boost-invariant mode using the E recombination scheme and are required to fulfill the following cuts:

- $p_T^{\mathrm{jet1}} \geq 7\,\mathrm{GeV}$;
- $p_T^{\mathrm{jet2}} \geq 6\,\mathrm{GeV}$;
- $|\eta^{\mathrm{jet}}| < 2.5$.

The values of the jet cuts are chosen to ensure that the jets are well reconstructed and understood at both calorimetric and hadronic level. They depend mainly on the trigger cuts applied on the reconstructed transverse energy.

Muon-Jet Association

Only events with at least one valid jet-muon association of a jet passing the jet cuts and a muon passing the muon cuts are selected. A jet is associated to a muon if it includes the muon EFO object identified during the EFO reconstruction (see Section 5.3). The jet of the associated muon has to have a minimal transverse momentum of

$$p_T^{\mathrm{jet}} \geq 6\,\mathrm{GeV}\ . \tag{6.11}$$

A non-negligible background to muon plus dijet events arises from cosmic muons, where a cosmic muon traverses the detector and the muon track is misidentified as two jets containing a muon. These events can be rejected by the requirement:

$$p_T^{\mathrm{jet}} - p_T^\mu \geq 2\,\mathrm{GeV}\ . \tag{6.12}$$

Jet Control Plots

MC true jets are formed using the MC true final states at the generator level, applying the KTCLUS algorithm to the stable final-state particles. For the MC true jets, B-hadrons are defined as stable particles.

The difference between the kinematics of the reconstructed jets including the muons and true MC jets is shown in Figure 6.6. The comparison shows a slight residual shift between the true and the reconstructed level as expected from previous studies [86]. One possible explanation is the absence of neutrinos in the reconstructed jets, as they are built from reconstructed EFOs, which depend on tracking and energy measurement information, while the true MC jets are built at B-hadron level, before they decay into a muon and a neutrino.

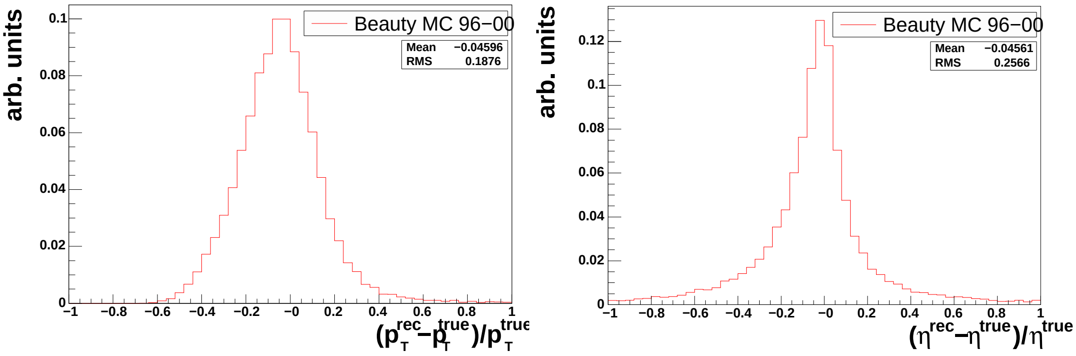

Figure 6.6: Comparison of true and reconstructed values for the transverse momentum of the muon jet $p_T^{\mu\text{-jet}}$ and $\eta^{\mu\text{-jet}}$ for the beauty MC sample applying a dijet+muon selection.

The comparison of the transverse momentum and the pseudo-rapidity of the jet associated to a selected muon and the same distributions for the jet without a muon associated are shown in Figure 6.7. The description of the p_T spectrum of the muon jet is very good, while the η^{jet} distribution shows the same shift as for the η^{μ} of the muon (Figure 6.5). As the muon has to be associated to the jet, the pseudo-rapidities of the muon and the jet are correlated and the shift has most probably the same origin, see Section 6.6. The shift is also visible in the distribution of the other jet, not associated to the muon.

The jets are clustered from EFOs using the KTCLUS algorithm in the massive scheme, taking into account the mass of the particles forming the jet. The control distribution of the mass of the jet associated to a muon, shown in Figure 6.8(a), confirms the compatibility of the data and the simulation for the jet reconstruction.

Another interesting variable is the ratio of the transverse momentum of the muon to the transverse energy of the jet associated to it. p_T^{μ}/E_t^{jet} represents the fraction of the transverse energy of the jet taken by the muon. It gives an idea of the agreement of the description of the hadronic part of the jet. From Figure 6.8(b) one can see, that the agreement is acceptable but the MC seems to be slightly shifted with respect

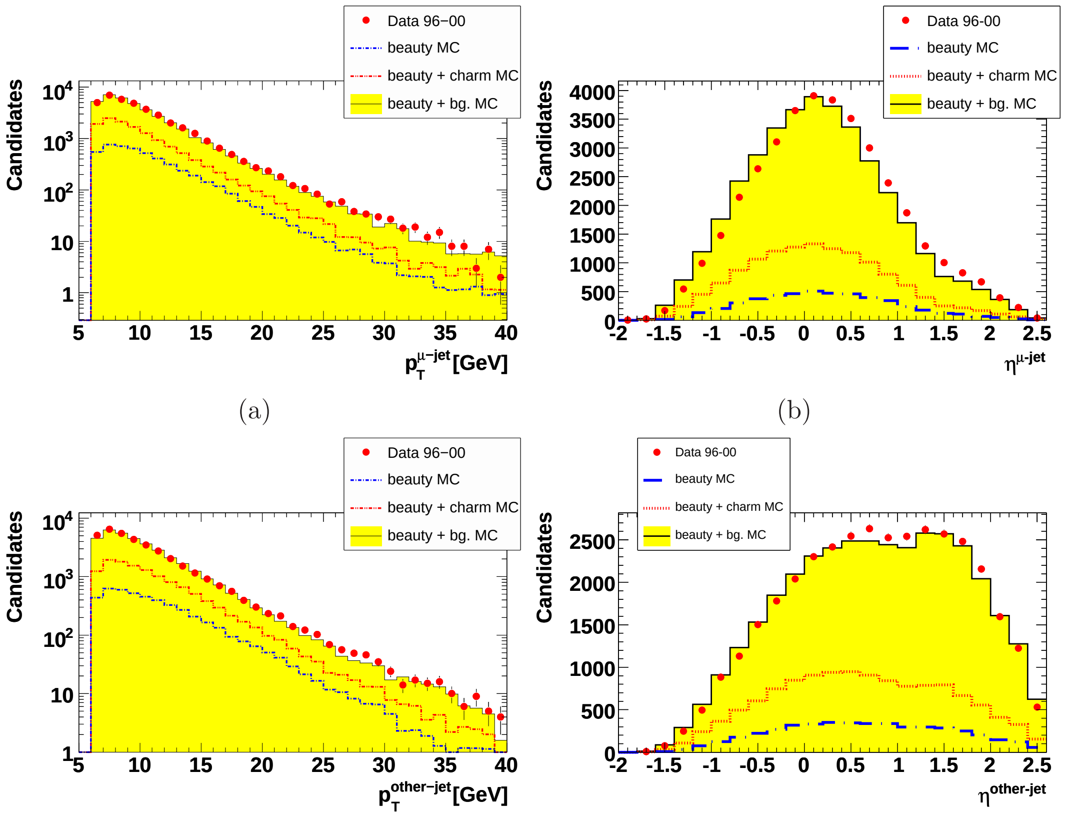

(a)

(b)

(c)

(d)

Figure 6.7: Comparison of data and MC for the jet transverse momentum (a) $p_T^{\mu\text{-jet}}$, (b) $\eta^{\mu\text{-jet}}$, (c) $p_T^{\text{other-jet}}$ and (d) $\eta^{\text{other-jet}}$ of the other jet.

to the data.

6.6. The x_γ distribution

A separation between direct and non-direct photon processes was achieved in the early stages at HERA via the observation of large energy deposits in the rear calorimeter consistent with a photon remnant [87]. This separation of the direct and non-direct processes can be expressed using the fraction of the photon's momentum, x_γ, taking part in the hard interaction. Energy and momentum conservation in a $2 \longrightarrow 2$ parton scattering yield:

$$x_\gamma^{LO} = \frac{\sum_{\text{partons}}(E - p_z)_{\text{parton}}}{2E_\gamma} \, , \tag{6.13}$$

where E_γ is the initial photon momentum and the sum is over the two final state partons. For direct processes, $x_\gamma = 1$ and for non-direct processes it is smaller.

Translating this to the measurement, the jet energies and momenta may be used to estimate the energies and momenta of the final state partons. Using for the photon

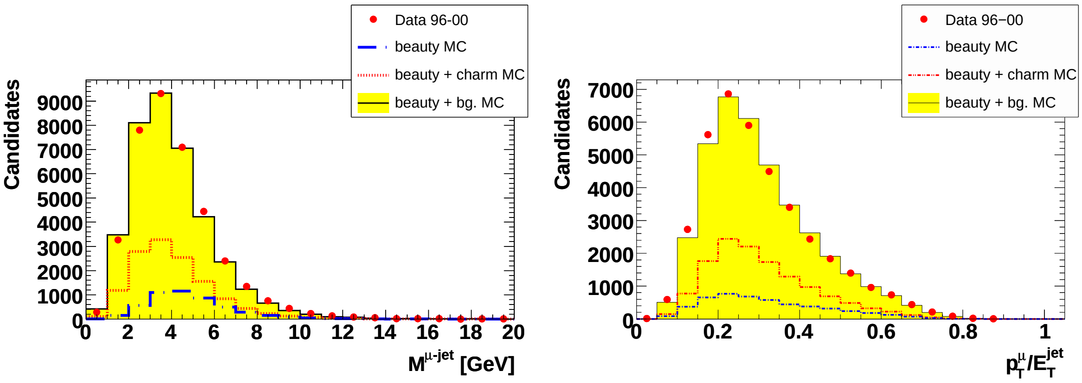

(a) (b)

Figure 6.8: Comparison of data and MC for the mass of the jet associated to the muon and the ratio p_T^μ/E_T^{jet}.

energy $E_\gamma \approx E_e y \approx E_e y_{JB}$ we can approximate x_γ as

$$x_\gamma^{meas} = \frac{\sum_{jets}(E-p_z)_{jet}}{\sum_i (E-p_z)_i} \ , \tag{6.14}$$

where the sum in the denominator runs over all EFOs. If the jets are massless, Equation 6.14 is equivalent to the definition:

$$x_\gamma^{obs} = \frac{\sum_{jets}(E_T^{jet} e^{-\eta^{jet}})}{2yE_e} \ . \tag{6.15}$$

To measure the cross-section separately for the direct-enriched and the non-direct enriched regions a separation cut on x_γ^{meas} is applied and the cross-sections are measured separately for $x_\gamma^{meas} < 0.75$ (non-direct enriched) and $x_\gamma^{meas} \geq 0.75$ (direct enriched). Figure 6.9 shows the x_γ distribution for the selected events. The shaded area on the left plot shows the direct contribution in the Monte Carlo: The vertical line represents the separation cut at $x_\gamma^{meas} = 0.75$ which separates very well the direct and non-direct contributions. Comparing the data to the sum of the Monte Carlo it seems that the direct contribution is overestimated and the non-direct contribution underestimated in the Monte Carlo, which can also be a reason for the observed shifts in the distributions of $\eta^{\mu\text{-jet}}$ (Figure 6.7) and η^μ (Figure 6.5). As part of the systematic studies the x_γ distribution will be reweighted to the data, to see the effect on the cross-sections.

6.7. Additional Cuts

To reduce the contamination of cosmic muon events, a cut on the ratio of the total transverse momentum and the total energy deposited in the CAL, p_T/E_T, is applied. This also reduces the contamination from charged current interactions. A cut on the minimal total transverse energy deducting the energy deposited in a cone of 10°

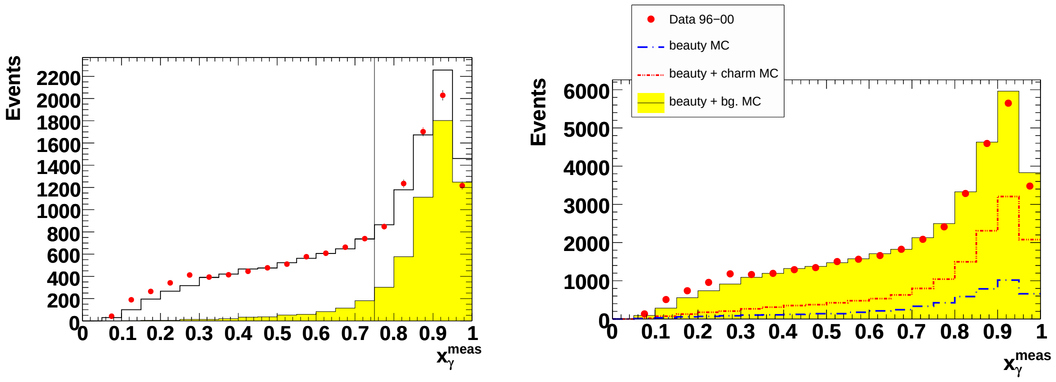

Figure 6.9: Comparison of data and MC as a function of x_γ. In the left plot the direct component of the MC is drawn as the shaded area, the vertical line at $x_\gamma = 0.75$ shows the cut used to separate the data into direct and non-direct regions for the 99-00 running period. On the right side the standard control plot with the different contributions from beauty, beauty+charm and beauty+background is shown.

around the proton beam direction in the FCAL is also applied. This second cut enriches the data with beauty, as the beauty mass is $2 \cdot m_b \approx 10\,\mathrm{GeV}$:

$$\begin{aligned} p_T/E_T &< 0.5\ , & (6.16)\\ E_{T\text{−FCAL-cone}} &\geq 7.5\,\mathrm{GeV}\ . & (6.17) \end{aligned}$$

To reduce further the number of beam-gas and cosmic muon events, cuts on the number of tracks in the event are applied:

$$\begin{aligned} n_{\text{vertex-fitted}} &> 2\ , & (6.18)\\ \frac{n_{\text{tracks}}}{n_{\text{vertex-fitted}}} &\leq 10.0\ . & (6.19) \end{aligned}$$

Applying this selection to a charged current MC many events survived. For this reason a cut on the total missing hadronic transverse momentum calculated from EFOs $p_{T,\text{had}}$ has been applied:

$$p_{T,\text{had}} \leq 10\,\mathrm{GeV}\ . \qquad (6.20)$$

6.8. Summary of Offline Cuts

To summarise the selection explained in detail in this chapter, the events have to pass the following selection criteria:

Trigger:

The events have to pass one of the following third-level trigger slots:
HPP14, EXO11, EXO12, MUO3, HFL1.

Photoproduction Selection:

- reject the event if an electron is reconstructed with
  - $P_{el} > 0.9$,
  - $E_{el} > 5\,\mathrm{GeV}$ and
  - $y_{el} < 0.9$;
- cut on y using the Jacquet-Blondel method: $0.2 < y_{JB} < 0.8$;
- $|z_{\mathrm{vertex}}| < 40\,\mathrm{cm}$.

Muon selection:

- at least one muon is reconstructed fulfilling the following requirements
  - GMUON quality ≥ 4 ;
  - $p_T^{\mu} \geq 1.5\,\mathrm{GeV}$;
  - $-2.0 < \eta^{\mu} < 2.5$;
  - $p_{T,\Delta R=1}^{EFOs} > 0.5\,\mathrm{GeV}$.

Jet Selection

- at least two jets fulfilling the following requirements:
  - $p_T^{\mathrm{jet}\ 1} \geq 7\,\mathrm{GeV}$;
  - $p_T^{\mathrm{jet}\ 2} \geq 6\,\mathrm{GeV}$;
  - $|\eta^{\mathrm{jet}}| < 2.5$.
- at least one jet associated to a selected muon fulfilling:
  - $p_T^{\mathrm{jet}} \geq 6\,\mathrm{GeV}$;
  - $p_T^{\mathrm{jet}} - p_T^{\mu} \geq 2\,\mathrm{GeV}$.

Additional Cuts:

- **Tracks:**
  - $n_{\text{vertex-fitted}} > 2$;
  - $\frac{n_{\text{tracks}}}{n_{\text{vertex-fitted}}} \leq 10.0$.
- **Calorimeter/EFOs:**
  - $p_T/E_T < 0.5$;
  - $E_{T-\text{FCAL-cone}} \geq 7.5\,\mathrm{GeV}$;

- $p_{T,\mathrm{had}} \leq 10\,\mathrm{GeV}$.

The number of events selected for the different running periods is summarised in Table 6.4. In some events more than one muon-jet association is found. Therefore the number of selected events is smaller than the number of selected muon-jet associations. The distributions of quantities of the muon-jet system are hence filled per muon-jet match, while the distributions of the general event properties are filled only once per event.

Running Period	Number of Events	Number of Muon-Jet Associations
96-97	11904	12299
98-99	5483	5614
99-00	19149	19797
96-00	36536	37710

Table 6.4: Number of selected events and muon-jet associations for the different running periods.

The number of events passing each group of cuts if it is applied only and in the consecutive order in the data sample and in the signal Monte Carlo are summarised in Table 6.5.

	Data		Beauty MC sample	
Cut	Events passed cut	Events passed cut consec. [%]	Events passed cut	Events passed cut consec. [%]
Preselection - Inclusive MC	11024867	281.9	199226	288.0
Trigger	4101096	100.0	69190	100.0
Vertex	10057693	94.8	187973	97.0
DIS Electron	8701290	82.8	186711	89.4
Calorimeter (p_T/E_T, $E_{T-\text{FCAL-cone}}$)	7341058	57.3	170829	85.7
EFO (Y_{JB},$p_{T,\text{had}}$)	5316273	45.0	113532	66.0
Tracks ($n_{\text{vertex-fitted}}$, $\frac{n_{\text{tracks}}}{n_{\text{vertex-fitted}}}$)	9182945	9.2	194072	18.8
Jets	896237	9.2	22384	18.8
Muons	907659	1.1	36835	5.5
Muon-Jet Association	91849	1.0	5514	4.8

Table 6.5: Number of events surviving each cut on data and signal MC, if the cut applied only and sequentially, starting from a muon preselection requiring one muon candidate of quality ≥ 4, or a muon transverse momentum of $p_T^\mu > 5\,\text{GeV}$ or more than one muon candidate in the event. The MC selection starts from the inclusive sample. For comparison, the number of events after trigger cuts is set to 100%.

7. Beauty Identification

After the event reconstruction and the data selection, the identification of beauty quarks is the last step towards a measurement of the beauty-quark cross-sections.

This chapter describes how the amount of beauty semi-leptonic decays into muons is determined in the selected dijet+muon data sample. The different MC samples, beauty, charm and light flavour are used to model the contributions of signal and background. The shape of a suitable variable is used to discriminate the contributions of signal and background. First the discriminating variable is described followed by the fitting method used to extract the beauty fraction in the data.

7.1. p_T^{rel} calculation

Beauty quarks are significantly heavier than charm and light flavour quarks. This is reflected in their decay kinematics.

A suitable observable sensitive to the quark masses in semi-leptonic decays into muons is the transverse momentum of the muon relative to its parent quark, p_T^{rel}. Due to the large beauty-quark mass the p_T^{rel} spectrum of muons originating from beauty quarks is harder than the p_T^{rel} spectrum from charm and light flavour quarks.

As quarks are not experimentally observable, jets are reconstructed to represent the momentum of the quarks and to define the reference for the calculation of the p_T^{rel} of the muon. A sketch of the variable is given in Figure 7.1.

Two definitions of the transverse momentum of the muon relative to its associated jet are possible. In the first definition the muon momentum is part of the jet momentum:

$$p_T^{rel-injet} = |\overrightarrow{p}_T^{\mu}| \cdot \sin\left(\mathrm{acos}\left(\frac{\overrightarrow{p}_T^{\mu} \cdot \overrightarrow{p}_T^{jet}}{|\overrightarrow{p}_T^{\mu}| \cdot |\overrightarrow{p}_T^{jet}|}\right)\right) \quad . \tag{7.1}$$

The shape of the p_T^{rel} variable in the data and in the different Monte Carlo samples is shown in Figure 7.2. The comparison of the shape of in the different Monte Carlo samples shows a harder p_T^{rel} spectrum from beauty quarks, while the shapes in the charm and light flavour Monte Carlo samples are quite similar to each other. The second definition subtracts the muon momentum from the jet and calculates the transverse momentum of the muon relative to the new jet axis according to the following equation:

$$p_T^{rel} = |\overrightarrow{p}_T^{\mu}| \cdot \sin\left(\mathrm{acos}\left(\frac{\overrightarrow{p}_T^{\mu} \cdot (\overrightarrow{p}_T^{jet} - \overrightarrow{p}_T^{\mu})}{|\overrightarrow{p}_T^{\mu}| \cdot |(\overrightarrow{p}_T^{jet} - \overrightarrow{p}_T^{\mu})|}\right)\right) \quad . \tag{7.2}$$

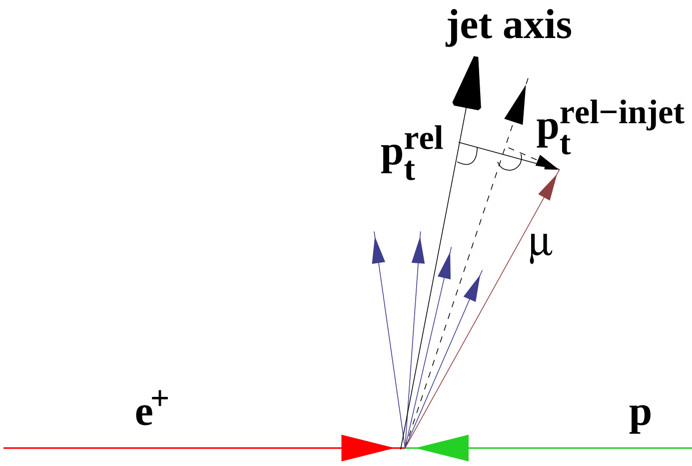

Figure 7.1: Definition of the transverse momentum of the muon relative to its associated jet, p_T^{rel}.

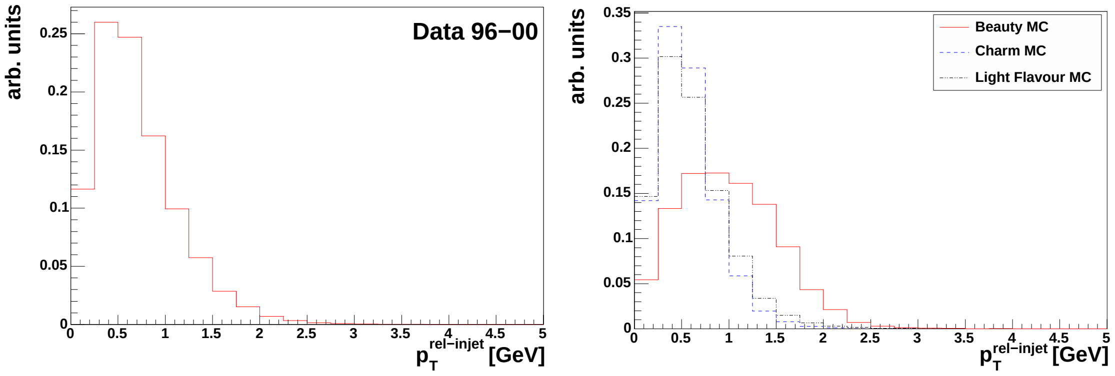

Figure 7.2: $p_T^{rel-injet}$ distribution in the data sample(left) and the MC samples (right) area normalised, including the muon momentum in the jet for the $p_T^{rel-injet}$ definition.

By subtracting the muon transverse momentum from the jet the calculated p_T^{rel} spectrum is shifted to larger values compared to the first p_T^{rel} definition, see Figure 7.3. To be consistent with previous analyses [88] the second definition was used for the cross-section determination.

7.1.1. p_T^{rel} shape correction

In order to use the shape of the p_T^{rel} variable to extract the number of beauty events in the data, a good description of the background shapes in the MC simulation is necessary. This has been analysed by comparing the background distributions in data and MC.

In order to produce a data sample including mainly background, a data sample

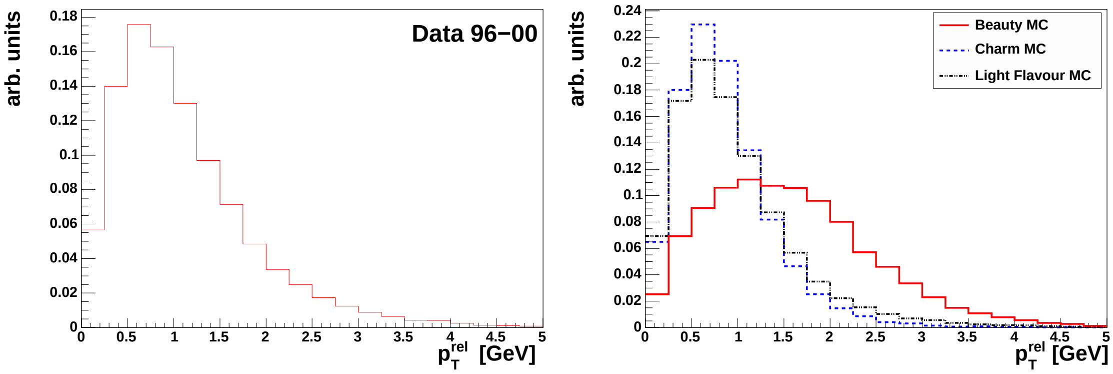

Figure 7.3: p_T^{rel} distribution in the data sample (left) and the MC samples area normalised (right) subtracting the muon momentum from the jet momentum for the p_T^{rel} definition.

applying the event selection without muon requirement has been used. The muon requirement has been replaced by a single track requirement in the same kinematic region as the muon. The track is associated to a jet using a ΔR cut:

$$\Delta R = \sqrt{\Delta\eta^2 + \Delta\phi^2} < 1.0 \ . \tag{7.3}$$

The p_T^{rel} variable is then calculated for each track which passes the event selection criteria except for the GMUON quality.

The same procedure is applied to the light flavour MC sample and the shape of the two distributions are compared. The background distribution in the data is harder than the background in the Monte Carlo; hence, a correction factor is determined bin by bin for every p_T^{rel} distribution used for the cross-section determination. As the light flavour Monte Carlo contains only background from fake muons, the shape of the p_T^{rel} distribution is corrected using these factors. The main uncertainty of the p_T^{rel} distribution is due to the quark mass, which is much better measured for beauty than for charm and light flavour, hence no corrections are applied to the beauty MC. Figure 7.4(a) shows the light flavour Monte Carlo before and after the corrections. The correction factors are between 0.7 and 1.2 for the global fit.

The treatment for the charm MC sample is more complicated. As it is not possible to obtain a pure charm sample from the data, the p_T^{rel} shape for charm cannot be directly determined as in the light flavour case. Therefore it was decided to apply an intermediate value of 50% of the light flavour correction, taking then into account a large variation of this estimate in the systematic uncertainties. Figure 7.4(b) shows the charm Monte Carlo before and after the corrections.

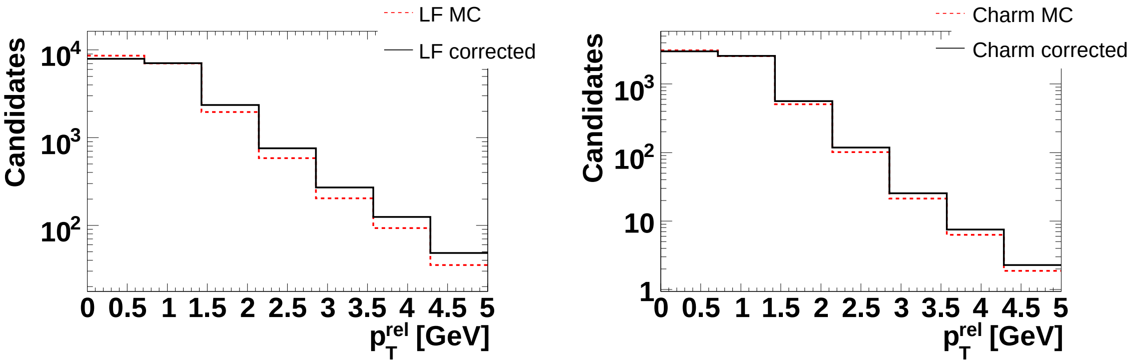

(a) (b)

Figure 7.4: Comparison of the p_T^{rel} shape before and after the corrections for (a) charm and (b) light flavour.

7.2. Beauty Fraction Determination

The extraction of the relative contributions of the signal and background in the data sample is carried out by a χ^2 fit of the MC p_T^{rel} distributions to the data. As the difference between the charm and light flavour p_T^{rel} shapes is small, a 3 parameter fit to the p_T^{rel} distribution is not sensitive to the different contributions from charm and light flavour. Therefore the relative contributions from charm and light flavour are fixed and for the systematic uncertainties studies varied around the central value. The fit function to determine the contributions from signal and background determines two scaling factors P_{signal} and $P_{\text{background}}$. The total number of events in the data is given by:

$$N_{\text{data}}^{\text{total}} = P_{\text{signal}} \cdot N_{\text{signal}}^{\text{total}} + P_{\text{background}} \cdot N_{\text{background}}^{\text{total}} , \tag{7.4}$$

where $N_{\text{signal}}^{\text{total}}$ and $N_{\text{background}}^{\text{total}}$ are the total number of events in the signal and the background Monte Carlo respectively. The statistics are high enough in each bin of the p_T^{rel} distribution, the parameters P_{signal} and $P_{\text{background}}$ can hence be determined by the minimisation of the following test distribution:

$$\chi^2 = \sum_i \frac{(N_{\text{data}}^i - (P_{\text{signal}} \cdot N_{\text{signal}}^i + P_{\text{background}} \cdot N_{\text{background}}^i))^2}{\sigma_{i,\text{data}}^2 + \sigma_{i,\text{signal}}^2 + \sigma_{i,\text{background}}^2} . \tag{7.5}$$

i is the sum over all bins in the p_T^{rel} distribution and $\sigma_{i,\text{data}}^2$, $\sigma_{i,\text{signal}}^2$ and $\sigma_{i,\text{background}}^2$ are the statistical errors on the entries in each bin.

The fraction of beauty events in the data can be calculated from the fitted parameters using the following relation:

$$f_{\text{beauty}} = \frac{N_{\text{data}}^{\text{beauty}}}{N_{\text{data}}^{\text{total}}} = \frac{P_{\text{signal}} \cdot N_{\text{signal}}^{\text{total}}}{P_{\text{signal}} \cdot N_{\text{signal}}^{\text{total}} + P_{\text{background}} \cdot N_{\text{background}}^{\text{total}}} , \tag{7.6}$$

where $N_{\text{background}}^{\text{total}}$ and $N_{\text{signal}}^{\text{total}}$ are the total number of signal and background events selected in the MC samples.

The errors on the fit parameters are determined using the Minuit package [89]. For the determination of the beauty-quark cross-section only the number of events containing beauty quarks are relevant. This can be obtained using:

$$N_{\text{data}}^{\text{beauty}} = f_{\text{beauty}} \cdot N_{\text{data}}^{\text{total}} \,. \tag{7.7}$$

and for the error:

$$\sigma_{N_{\text{data}}^{\text{beauty}}} = \sigma_{f_{\text{beauty}}} \cdot N_{\text{data}}^{\text{total}} \,. \tag{7.8}$$

The error of the background scale factor, $P_{\text{background}}$, is negligible compared to the error on P_{signal}. The error on on the beauty fraction can therefore be approximated by:

$$\sigma_{f_{\text{beauty}}} = \frac{\sigma_{P_{\text{signal}}} \cdot N_{\text{signal}}^{\text{total}}}{P_{\text{signal}} \cdot N_{\text{signal}}^{\text{total}} + P_{\text{background}} \cdot N_{\text{background}}^{\text{total}}} \,. \tag{7.9}$$

The result of the global p_T^{rel} fit is shown in Figure 7.5. The resulting beauty fraction is $13.09 \pm 0.75\%$ and the $\chi^2/ndf = 2.9/5$

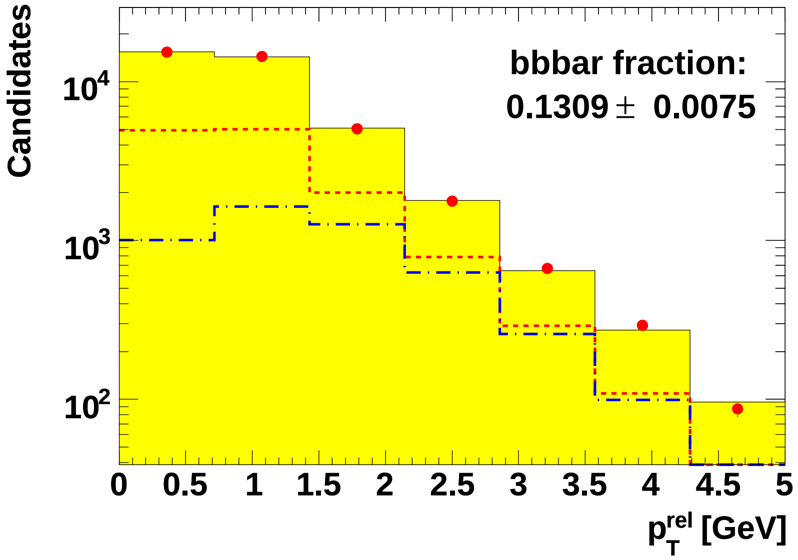

Figure 7.5: p_T^{rel} distribution in the data sample compared to MC. The signal and background Monte Carlo is scaled using the scaling factors P_{signal} and $P_{\text{background}}$ from the global p_T^{rel} fit. The lower line represents the beauty content, the middle line beauty and charm and the upper line is the sum of beauty charm and light flavour.

8. Fake-Muon Background

The extraction of the signal from b-quark decays requires the correct evaluation of the background processes surviving the selection cuts. Due to the large cross-section the background coming from light flavour quarks can only be simulated using preselection cuts e.g. on the jet energy. For the event selection described in Chapter 6 about 20 Mio. events have to be generated to obtain the equivalent of the data luminosity, while only 10000 events would pass the analysis cuts. A requirement of two jets with $E_T > 4\,\mathrm{GeV}$ reduces the amount of simulated events by a factor of five for the direct component and a factor of ten for resolved processes. An alternative to a huge MC generation is the extraction of fake-muon probabilities from Monte Carlo with a preselection on the jets and to use these probabilities to determine the fake-muon background directly from the data during the analysis. The fake muon probability should be independent of the jet cuts. The idea is hence to produce fake-muon probabilities from a Monte Carlo sample with a jet preselection and to apply these probabilities on different event selections, with and without cuts on the jets. The study of the feasibility of this method and its implementation in two different analyses is the topic of this chapter.

8.1. Classification of Fake Muons

For the classification of fake muons one has to distinguish between ‘real’ fake muons, i.e. hadrons penetrating through to the muon chambers, so-called punch-throughs, and decays from light flavour hadrons i.e. kaons and pions into muons.

The different sources are listed in the following:

- **Sail-through:** Hadrons have a probability to traverse the material in front of the muon detection system without interaction. The probability for this process is given by
$$P(d) = \exp^{-d/\lambda} \ , \tag{8.1}$$
where λ is the interaction length and d is the traversed distance. At ZEUS, the material in front of the muon chambers varies between 4 λ (RCAL) and 5 λ (BCAL) with leads to a sail-through probability of $\sim 1\%$. In the region between the calorimeters at $\eta = -0.7$ and $\eta = 1.0$, the so-called super-cracks, the probability for a hadron to reach the muon chambers is substantially higher.

- **Hadronic-shower leakage:** Hadronic particles escaping the calorimeter can traverse the inner and outer muon chambers. This contribution is partially removed by the muon reconstruction algorithm and a cut based on the quality of the matching between tracks and muon segments.

For hadronic-shower leakage and sail-throughs the detected muon is actually a hadron, hence these sources are treated together and called **punch-through**[1].

- **In-flight hadron decays:** Pions are the most frequent hadrons created in ep collisions at HERA. They can decay via the process $\pi^{\pm} \rightarrow \mu^{\pm}\nu_{\mu}$ with a lifetime of $\tau = 2.6 \cdot 10^{-8}\,\mathrm{s}$ corresponding to a proper decay length of $c\tau = 7.8\,\mathrm{m}$. Charged kaons are also frequently produced and can also decay into muons. Their decay length is $c\tau = 3.7\,\mathrm{m}$.

- **Track-Muon Mismatches:** The last source of fake muons come from mismatches between a track at the entrance of the calorimeter whose position corresponds closely to the position of the muon candidate extrapolated to the CAL front-face. This can happen if the track is very close to the track of the reconstructed muon candidate. These mismatches happen mainly between muon and electron tracks. After the selection of 'good' muon candidates (GMUON quality > 4, see Section 5.5) this contribution is about 2-3% of the fakes.

8.2. Fake-Muon Background Determination Method

8.2.1. Fake-Muon Probabilities

The fake-muon probability is defined track-wise as the probability for a track to be misidentified as a muon. Different dependencies of the fake-muon probabilities were analysed for the different kinds of fake muons. The most important variables are the p_T and the η of the track. The fake-muon probability is therefore binned in p_T and η. The binning is a compromise between available statistics and the structure of the fake-muon probabilities, with larger bins where the statistic is very low, to keep the influence of statistical fluctuations low, and finer bins, especially in the central, low p_T region, where the fake probability changes most.

$$\text{fake-muon probability} = \frac{\#\text{ fakes }(p_T, \eta)}{\#\text{ tracks }(p_T, \eta)}\ . \tag{8.2}$$

For the calculation of the fake-muon probabilities, light flavour direct and resolved PYTHIA Monte Carlo samples have been used for the different data taking periods with a preselection on dijet events with $E_T > 4\,\mathrm{GeV}$. These Monte Carlo samples are subsamples of the light flavour PYTHIA samples described in Section 6.1 and Appendix C. As the light flavour sample with jet preselection is still very large, not the whole set of MC could be stored in ntuples without further cuts. Therefore for a part of Monte Carlo a muon preselection was applied, reducing the amount of

---

[1] After the application of cuts to select good muon candidates the contamination from hadronic-shower leakage is negligible.

stored events substantially. For the determination of the fake muon probabilities a MC sample without preselection on the muon is needed, as this would otherwise bias the fake muon probabilities. The number of events and luminosities of the samples used for the fake-muon probability determination are summarised in Table 8.1. The muon candidates used for the fake-muon-probability calculation have to pass the same quality cuts as in the analysis. Therefore all probabilities shown here are calculated for a GMUON quality ≥ 4 which is the typical requirement for a good muon candidate in a semileptonic beauty to muon analysis (see Section 5.5.3).

Running Period	Process	Number of Events	Int.Luminosity [pb^{-1}]
1996-1997	dir	232186	19.7
1996-1997	res	1195199	32.9
1999-2000	dir	958617	76.4
1999-2000	res	2700239	68.7

Table 8.1: Overview of the MC samples used for the fake-muon probability determination.

8.2.2. Application of the fake-muon probabilities

After the determination of the probabilities, they have to be applied to the analysis. The easiest way is to run the analysis on an inclusive data sample, where inclusive means that one muon less than in the analysis selection is required in the data sample. E.g. for an analysis requiring two muons (dimuon analysis) a data sample with one muon preselected is needed and for a single muon analysis a sample without muon preselection is needed.

If the muon does not have to be associated to a jet, a muon or another object, each track of the event is treated as muon candidate, weighted with the probability to be a fake-muon. This would be the case in a single muon analysis, without jet-association.

If the muon has to be associated to a jet, or a dimuon object has to be built, one track per event has to be chosen as the fake muon candidate per event[2].

The method used is the following: the fake-muon track probabilities of all tracks in the event fulfilling the muon p_T and η cuts are summed up to a fake-muon event probability. In a next step a track is chosen randomly, according to its probability to be a fake-muon, declared as a muon candidate and added to the muon list. This muon candidate gets a flag to pass the muon quality cuts and is associated to the nearest jet with $E_T > 4\,\text{GeV}$ in a cone of $\Delta R = \sqrt{(\phi_{jet} - \phi_\mu)^2 + (\eta_{jet} - \eta_\mu)^2} = 1$. Finally each distribution is filled once per event weighted with the appropriate fake-event weight. As the fake muon is added to the list of reconstructed muons, the number of muon

---

[2] If every track in the event is associated to a jet, each jet would be filled several times in the jet distributions, depending on the number of tracks associated to it.

candidates is approximately correct[3].

In the case of a dimuon analysis presented below further corrections are needed, as muon triggers are used in the preselection of the single muon sample, which could bias the results and combinations of a fake muon and a signal muon are possible. This will be explained in Section 8.3.2.

8.3. Tests of Fake-Muon Probability Method

The probabilities should only depend on the muon detection system and the kinematics of the kaons and pions and not on the production process of the particles. This is important if one is going to use the fake-muon probabilities in different kinematic ranges where the production mechanism, and therefore the kaon and pion mixture, may be different. This has been tested by evaluating the fake-muon probabilities separately for different Monte Carlo samples (direct/resolved). The probabilities have been calculated separately for the different fake-muon sources. While the total number of fake-muons from decays is about 55% and from the rest about 45%, the probability to find a fake-muon from in-flight decays is more equally distributed while the punch-throughs concentrate in the central region at high p_T see Figure 8.1. The probability for fake-muons from punch-throughs and mismatches is concentrated in the high p_T region of the central and rear part of the detector, while it is flat for in-flight decays. As the statistics in the high pt region are low, the statistical error of the probabilities goes up to $\sim 30\%$ in the high p_T region, while it is around 4% in the central low p_T region.

The contamination with track-muon mismatches contributes with only 3% to the fake muons and is therefore not analysed separately.

It is implicit to the method that the mixture of fake muons is assumed to be the same in the data and Monte Carlo. For the muon algorithms using the barrel muon chambers this has been analysed by selecting a very pure hadron sample in data and Monte Carlo. It turned out that the assumption is reasonably good [90].

The next assumption is that the muon-efficiency correction is also valid for fake muons. This is certainly true for in-flight hadron decays, as they are real muons but not necessarily for punch-throughs, there the inefficiencies could be different. This has not been further tested.

8.3.1. Test on a Muon+Dijet Selection

After the general tests of the fake-muon probabilities discussed above, the application to a beauty analysis using semi-leptonic decays into muons is tested. The first test is done on the muon+dijet analysis, requiring one muon of $p_T > 1.5\,\mathrm{GeV}$ in the pseudo-rapidity range $-2 < \eta_\mu < 2.5$ with a GMUON quality ≥ 4 and two jets with $p_T^{\mathrm{jet1}} > 7\,\mathrm{GeV}$ and $p_T^{\mathrm{jet2}} > 6\,\mathrm{GeV}$. The jet associated to the muon has to have a

---

[3] If the chosen track belongs to a reconstructed muon it is stored only once, the reconstructed muon is deleted from the list

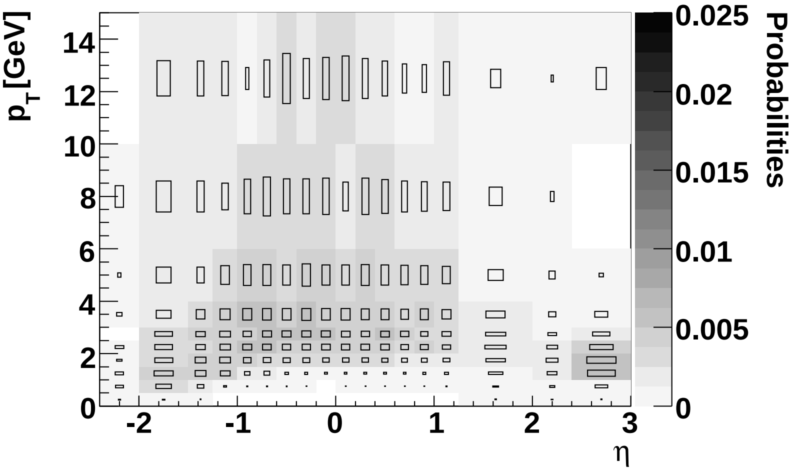

(a) In-flight decays

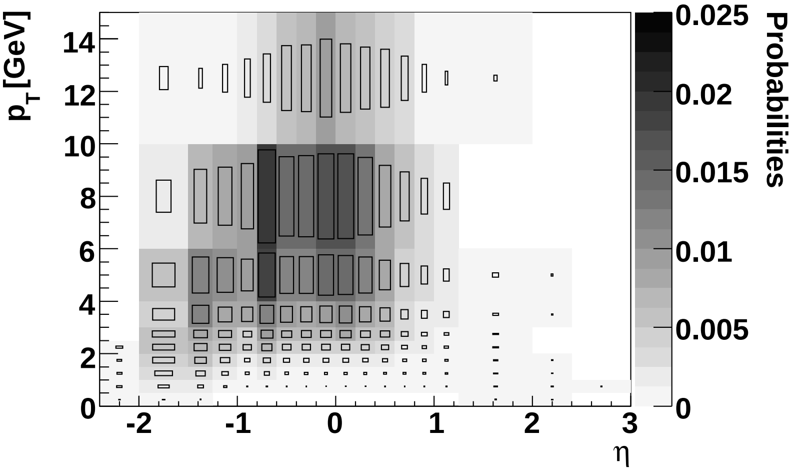

(b) Punch-through

Figure 8.1: Fake-muon probability separately for in-flight decays and punch-through+mismatches. The area of the rectangles is proportional to the fake-muon probability.

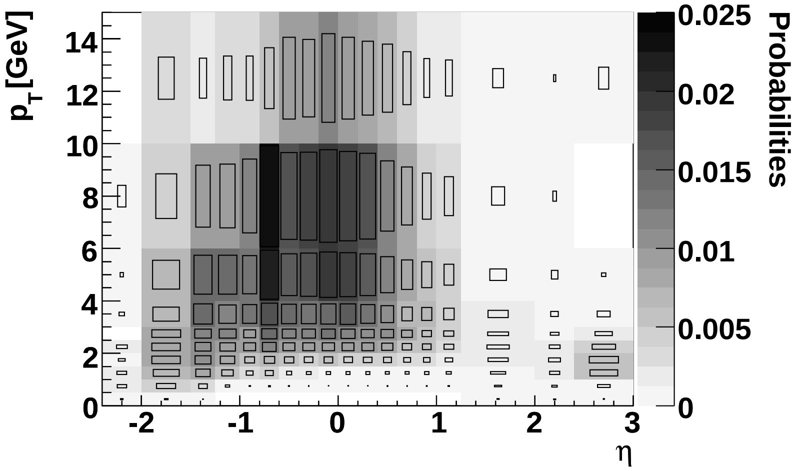

Figure 8.2: Final fake-muon probability used for the tests of the method calculated from 96-00 direct and resolved light flavour PYTHIA Monte Carlo.

$p_T > 6$ GeV. For this test only the dijet trigger (HPP14, see Section 6.2) is used. Details of the event selection are given in Chapter 6. The probability used for this test is shown in Figure 8.2. As the jet-muon association is required the second method explained in Section 8.2.2 is used.

If the fake muon probabilities are calculated from a set of Monte Carlo files and applied to the same Monte Carlo with the same cuts as for the production the agreement is perfect, which means that the method technically works.

In the first set of plots the fake-muon probabilities determined from 96-00 direct and resolved Monte Carlo are applied separately to a 99-00 direct Monte Carlo and a 99-00 resolved Monte Carlo sample. The predictions are compared with the reconstructed muons in the same Monte Carlo samples, see Figures 8.4 and 8.5. The agreement is not necessarily perfect as the fake-muon probabilities are determined from a different set of Monte Carlo, a muon-jet association is now required and the muon candidates from the muon algorithm are stored in addition to the fake-muon candidate and weighted with the fake-muon event weight to reproduce the distribution of the number of muons in the event. The normalisation of the Monte Carlo distribution is now no longer the same as for the fake-muon method applied on the Monte Carlo sample, the fake-muon method histograms have to be scaled down by a factor of 1.4. But this is not very important as the fraction of the signal and background Monte Carlo are determined in a fit. The transverse momentum of the muon with respect to the jet, p_T^{rel}, and the ΔR distribution are described very well, which is important as the p_T^{rel} variable is used to discriminate between beauty, charm and light flavour (see Section 7.1), while there are systematic differences in the μ-jet distributions. The μ-jet p_T is shifted to higher values. Different effects play a role:

- Comparing the jet p_T distribution of fake muons from decays and from punch-throughs, see Figure 8.3, one can see that the distribution of the punch-throughs is shifted to the right with respect to the distribution of muons from in-flight decays. In jets with fake muons from decays, the neutrino energy is missing in the jet, while in jets with fake muons from punch-throughs all particles are detected. Consequently the fake-muon method distribution is shifted to the right.

- A second effect is the jet-muon correction, see Section 5.3.3, subtracting a MIP and adding the momentum of the track of the muon candidate to the jet energy. This is of course wrong in the case of punch-throughs, which are not minimum ionising. In general hadrons leave all their energy in the calorimeter. Even if they reach the muon chambers, as in the case of punch-throughs, they still lose a large fraction of energy in the calorimeter. The jet-muon correction will therefore shift the punch-through muon distribution to the right with respect to the decay muons in Figure 8.3.

For the application of the fake-muon probabilities, an inclusive data sample without muon preselection is used, hence almost all jets are pure hadron jets and the first effect will shift the p_T-jet distribution using the fake-muon probabilities to the right with respect to the MC distributions. The jet-muon correction is only applied to jets with a reconstructed muon. For the application of the fake-muon method nearly all jets are pure hadron jets, hence the correction is not applied, which is correct, but results in a small shift to the left of the p_T-jet distribution with respect to the Monte Carlo, where the correction is wrongly applied for punch-throughs. The global effect is a shift to the right by the same amount for all different test samples, see Figures 8.4, 8.5.

In the next step the fake-muon probabilities are applied on 99 positron data and compared to 99-00 direct and resolved light flavour Monte Carlo, see Figure 8.6. The jet and muon distributions show the same differences as for the application on Monte Carlo, while there are additional differences in the p_T^{rel} and ΔR distribution. These differences are due to different track distributions in data and Monte Carlo, which means that using fake-muon probabilities a background shape correction as described in Section 7.1 is no longer needed. The differences in the other distributions are similar to the differences in the Monte Carlo distributions. The systematic effects can hence be estimated from Monte Carlo.

After these tests the complete beauty dijet analysis was run using the fake-muon probabilities applied on the 96-00 data. The data, beauty and charm distributions are the same as in Chapter 6. For the determination of the beauty fraction the p_T^{rel} method described in Section 7.1 was used. The global fit results in a beauty fraction of $14.5 \pm 0.7\%$ instead of $14.4 \pm 0.7\%$ as in the normal analysis[4]. The fits of the differential distributions all agree within errors and fluctuate statistically around each other, see Figure 8.7 and Appendix E.

---

[4] The data sample differs from the selection used in the fit in Chapter 7; only the dijet trigger is used here and a earlier version of the muon efficiency correction.

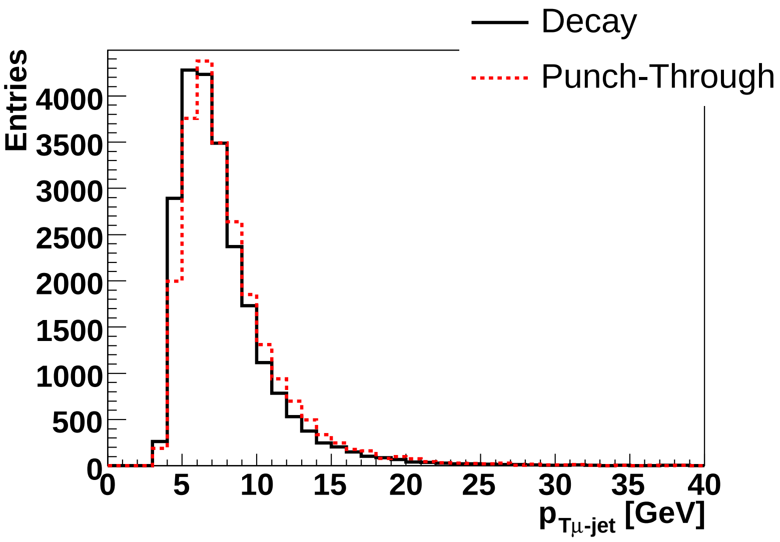

Figure 8.3: Comparison of the p_T-jet distributions for fake muons from decays and fake muons from punch-throughs. The distribution for punch-throughs is shifted to the right as there is no neutrino taking part of the jet energy and a muon correction is applied, subtracting a MIP and adding the track momentum to the jet energy.

8.3.2. Test on a Dimuon Analysis

The beauty analysis using a muon double tag to identify beauty [91] has not been described in this thesis so far. Therefore after a short introduction, the event selection and the strategy to extract the beauty and charm fractions and the background coming from J/Ψ, Ψ', Υ, Bethe-Heitler (BH) and light flavour will be explained, before coming to the alternative method to determine the light flavour background using fake-muon probabilities.

In this analysis beauty production is measured via the reaction $ep \rightarrow b\bar{b}X \rightarrow \mu\mu X'$. Using a muon double tag yields a data sample enriched in beauty, with strongly suppressed backgrounds from other processes. Therefore a very low p_T^μ threshold can be applied without requirements on jets. This leads to a sensitivity to a larger region of phase space, especially towards lower transverse momenta of the beauty quark, which minimises the extrapolation to the total beauty production cross-section. In contrast to the dijet+muon analysis no distinction is made between the photoproduction and the DIS regimes.

Event Selection

Trigger: The following triggers are used:

- hadronic triggers: dijet(HPP14), dijet+muon(HFL1), charm meson(HFL10/11);
- DIS triggers: general DIS(DIS3), DIS+muon(DIS27);

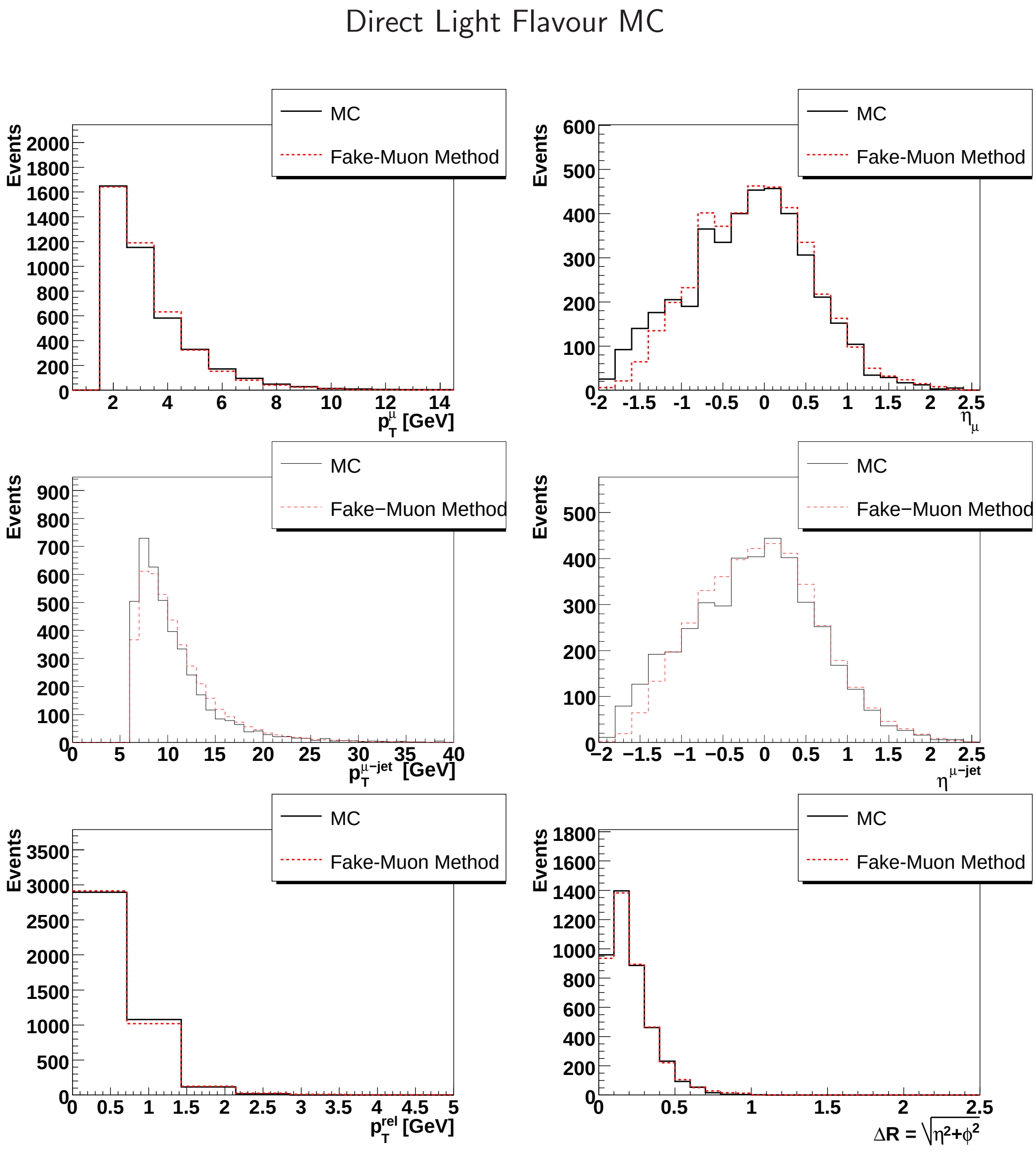

Figure 8.4: Test of the fake-muon method on a direct light flavour MC sample. The lines are the distributions directly taken from the Monte Carlo, while the dashed lines are the distributions from the fake-muon method applied on the same Monte Carlo. The agreement is perfect in p_T^{rel} and ΔR while there are systematic differences in the muon-jet distributions which are intrinsic to the method.

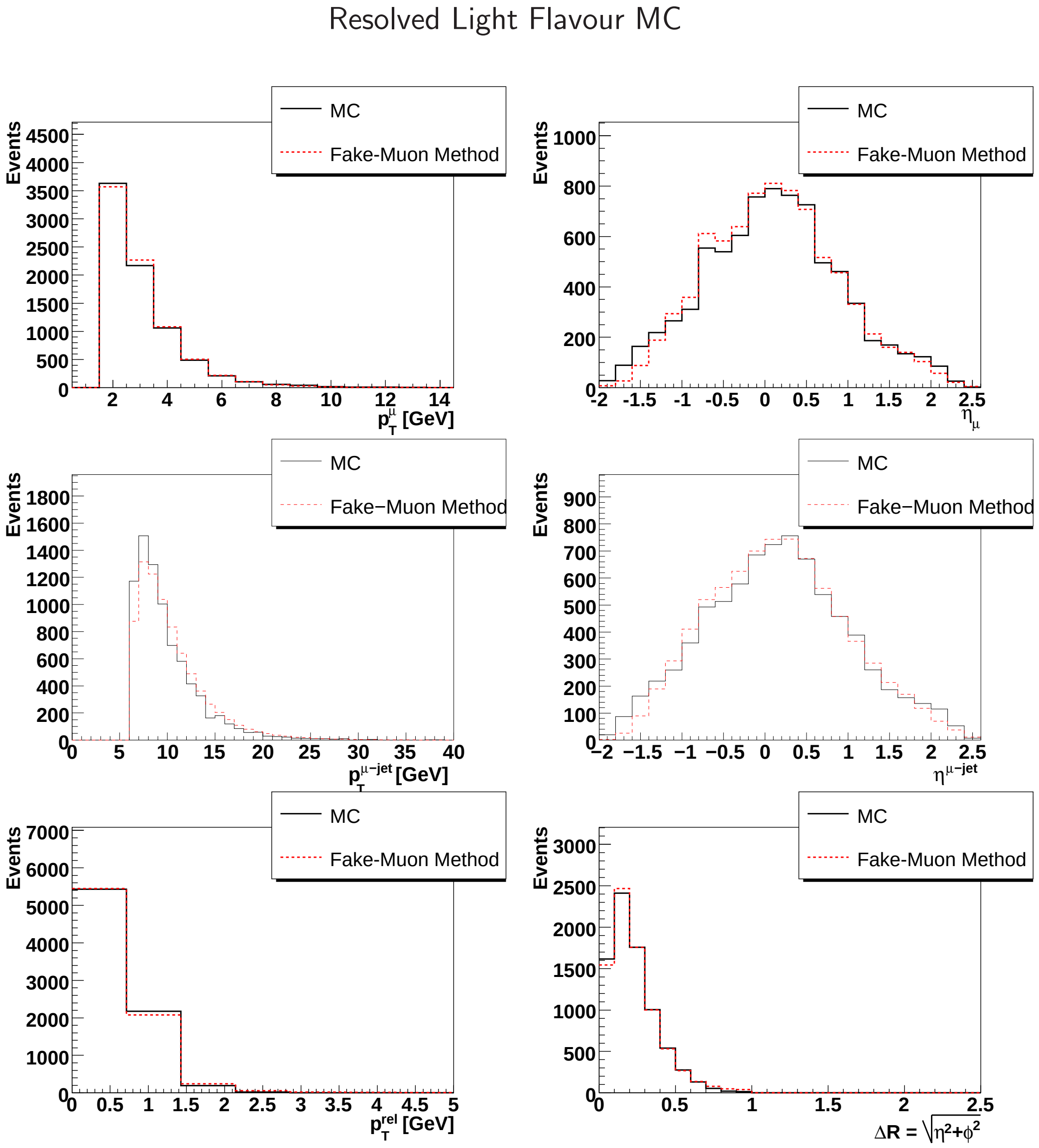

Figure 8.5: Test of the fake-muon method on a resolved light flavour MC sample. The lines are the distributions directly taken from the Monte Carlo, while the dashed lines are the distributions from the fake-muon method applied on the same Monte Carlo. The agreement is perfect in p_T^{rel} and ΔR while there are systematic differences in the muon-jet distributions which are the same as in the test on the direct light flavour sample.

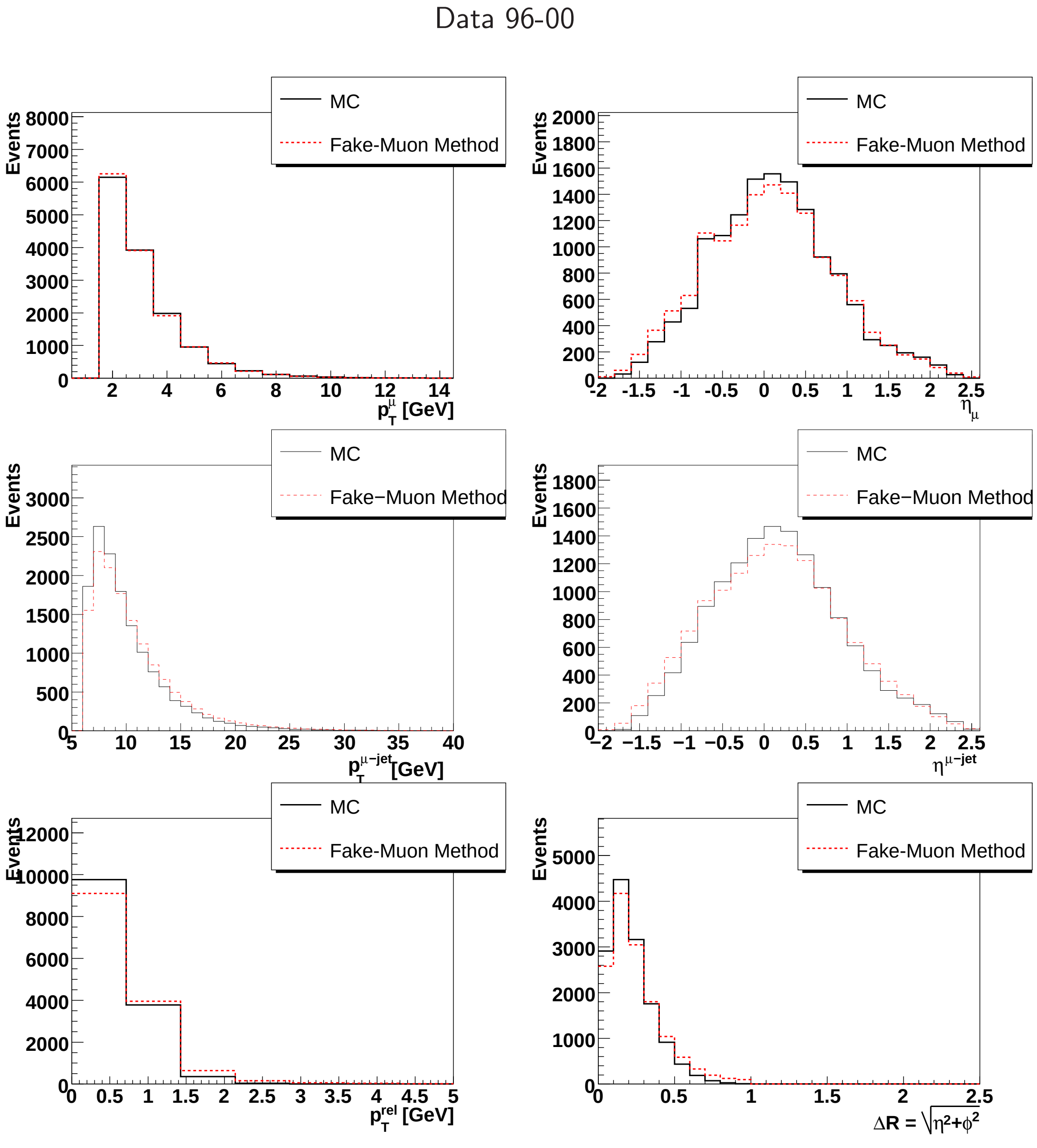

Figure 8.6: Test of the fake-muon method on an inclusive data sample: The fake-muon probabilities are applied on a set of inclusive data samples from 96-00 and compared with a mixture of direct and resolved light flavour Monte Carlo from 96-00. After luminosity weighting an extra factor of 0.4 was applied to the fake-muon plots, coming partly from the method (0.7 for MC) and partly from different light flavour content in data and MC.

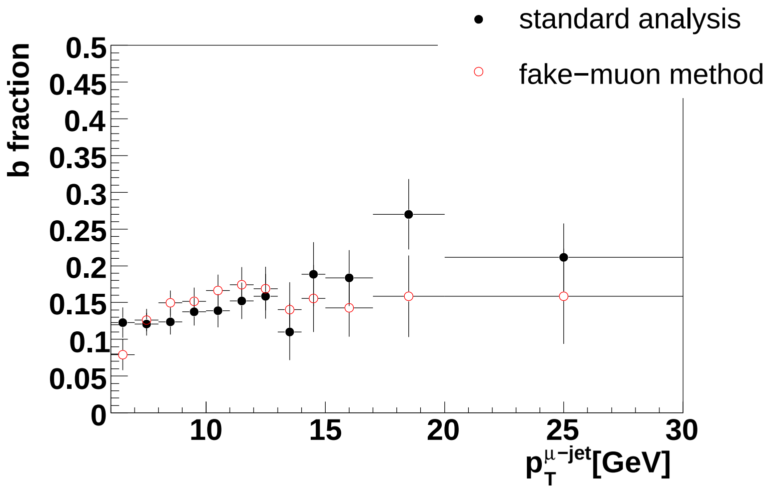

Figure 8.7: Comparison of the beauty fraction as a function of $p_T^{\mu\text{-jet}}$ from the fit using Monte Carlo for the background (solid points) and using the fake-muon method (open points). The fractions fluctuate around each other and agree within errors. The full set of plots can be found in Appendix E.

- muon triggers: forward (MUO1/2/4), barrel/rear (MUO3,EXO11,EXO12);

Dimuon Selection:

- ($p_T^\mu \geq 1.5$ & GMUON quality > 4) or ($p_T^\mu \geq 0.75$ & GMUON quality > 5);
- $|\eta^{\mu 1} - \eta^{\mu 2}| < 3.0$.

Further cleaning cuts to reduce the background are applied, for details see [91].

The sample is subdivided into four samples with different event characteristics, summarised in Table 8.2. A further separation is done by calculating the transverse hadronic energy around each muon, separating the samples into isolated (background) and non-isolated (signal).

Signal and Background Determination

Two main event classes contribute to the beauty signal to be measured. The first class are events where the two muons originate from the same parent B hadron, e.g. through the decay chain $b \to c\mu X \to s\mu\mu X'$. These yield unlike-sign muon pairs produced in the same hemisphere and a low dimuon invariant mass ($m^{\mu\mu} < 4\,\text{GeV}$). The second class of beauty events consists of muons originating from different beauty quarks. These events can produce like-sign and unlike-sign muon pairs, depending on

	low dimuon inv. mass ($m^{\mu\mu} < 4\,\text{GeV}$)	high dimuon inv. mass ($m^{\mu\mu} > 4\,\text{GeV}$)
unlike-sign charge $\pm/\mp$	**muons from same b,** $J/\Psi, \Psi$‘ + light flavour background	**muons from different b** or c, Υ, Bethe Heitler + light-flavour background
like-sign charge $++/--$	**light-flavour background**, few muons from diff. b	**muons from different b**, light flavour background

Table 8.2: Overview of the subdivision into different classes of events contributing in the dimuon analysis.

whether the muons originate from the primary beauty decay, or from the secondary charm decay and whether $B^0\bar{B}^0$ mixing has occurred. These muons are predominantly produced in different hemispheres and will therefore have a large dimuon invariant mass.

The first background contribution arises from primary charm-pair production, both charm quarks decaying into muons. This can only yield unlike-sign muon pairs, where the two muons are predominantly produced in different hemispheres. The charm contribution is too small to be measured directly. Therefore it was normalised using the charm contribution from a $D^* + \mu$ sample, which has a similar event topology and covers a similar though slightly more restricted kinematic range [92].

Other backgrounds like heavy quarkonium decays or Bethe-Heitler processes yield unlike-sign muon pairs without accompanying hadronic activity, thus giving a well-isolated muon signature.

Beauty production is the only source of genuine like-sign muon pairs. Background contributions from light flavour where one or both muons are fake muons contribute to both like-sign and unlike-sign muon combinations. The charge of light-flavour fake muon pairs is almost uncorrelated, i.e. the contributions to the like-sign and unlike-sign dimuon distributions are almost equal [91], with only small corrections. The difference between the unlike (N^u_{data}) and like-sign (N^l_{data}) distributions is thus essentially free from fake-muon background, without the need to simulate this background with MC methods. Once the other background contributions from charm (N_{charm}), J/Ψ and other heavy vector mesons (N_{VM}) and Bethe-Heitler (N_{BH}) are known, the difference between like-sign and unlike-sign can be used to extract the number of beauty events according to the formula:

$$N_{b\bar{b}} = (N^u_{\text{data}} - N^l_{\text{data}} - (N_{\text{charm}} + N_{VM} + N_{BH})) \times \left(\frac{N^u_{b\bar{b}} + N^l_{b\bar{b}}}{N^u_{b\bar{b}} - N^l_{b\bar{b}}} \right)^{MC} , \tag{8.3}$$

where $N^u_{b\bar{b}}$ and $N^l_{b\bar{b}}$ are the unlike-sign and like-sign beauty contributions predicted by the MC.

As like sign dimuon pairs can only originate from beauty decays or light flavour background, once the beauty contribution is known, the fake muon background can be obtained from the data by subtracting the MC like sign beauty contribution properly scaled to the data from the measurement. As the like-sign and unlike-sign contributions are approximately the same, the unlike-sign light flavour contribution can be obtained by mirroring the like-sign distribution to the unlike-sign distribution. This method to determine the fake muon background will be referred to as the subtraction method.

Alternative Background Determination using Fake-Muon Probabilities

As described above for the dimuon analysis, a data sample with a single muon preselection is used. Adding one track to the list of muon candidates results in three classes of events:

- two fake muons;
- one fake muon, one muon from a semi-leptonic beauty decay;
- one fake muon, one muon from a semi-leptonic charm decay.

For the application of the fake-muon probabilities, as a start all events in the data sample are treated as events with two fake muons. Assuming that both muons are fake, a track is chosen according to its probability to be a fake muon and added to the list of muon candidates. The fake-event weight is calculated summing up all fake muon track weights in the event. Afterwards corrections for the events with one muon from a semi-leptonic heavy-flavour decay and one fake muon are applied.

As muon triggers are used in this analysis a distinction has to be made between fake muons that triggered the event and fake muons that did not. The fake-muon probabilities are therefore calculated separately for muons that triggered the event and those that did not. For the muon already preselected one knows if the muon was the source of the trigger or not. To determine if the added muon candidate would have triggered or not, a random variable is used to take the decision according to the fake-triggered-muon probability. A first correction has to be made in the case that both muons in the event or none of them triggered. As the two muons are not distinguishable, the event weight has to be divided by two to avoid double counting of the event.

Not all muons in the data sample with a single muon preselection are fake. The events with one muon from a semi-leptonic beauty decay and one fake muon are part of the beauty signal; the number of these events and their fake-event weights have to be determined from the beauty MC and subtracted from the fake-muon distributions. Events with a semi-leptonic muon from primary charm decays together with a fake muon are part of the light flavour background. Therefore their fraction and their fake-event weights are determined from the charm MC and the fake-event weights are replaced by the original event weights of the charm Monte Carlo events.

The comparison of the light flavour background from the subtraction method and using the fake-muon probabilities is shown in Figures 8.8-8.10. The fake-muon background prediction uses the fake-event weight directly with no further normalisation.

For the tests only muons with quality ≥ 4 and $p_T^\mu > 1.5\,\mathrm{GeV}$ were used in the selection, as the fake muon probabilities for the second class on muons, quality ≥ 5 and $p_T^\mu > 0.75\,\mathrm{GeV}$ do not exist. The two methods agree very well in all variables. This is gratifying, given the large uncertainties coming from the different methods and assumptions discussed in this chapter.

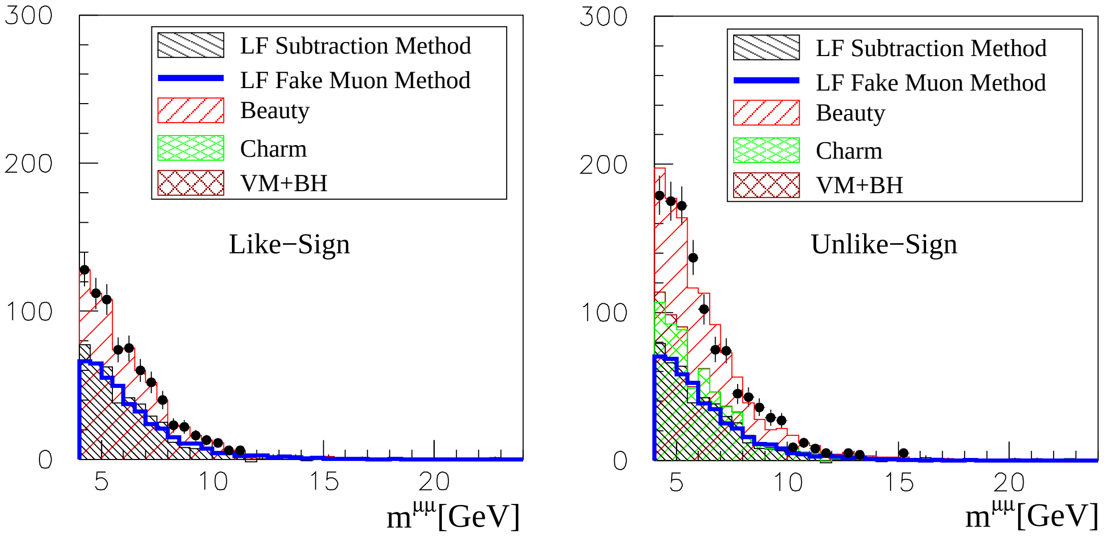

Figure 8.8: Distribution of the dimuon mass for non-isolated muons in unlike sign charge combination (left) and like-sign combination (right) and a dimuon mass $m^{\mu\mu} \geq 4\,\mathrm{GeV}$. The points are the data, the different hashes represent the contribution from beauty, charm, vector mesons (VM) and Bethe-Heitler (BH) and the background. On top of it the background distribution using the fake-muon probabilities is drawn as a blue thick solid line. In both samples the two methods to estimate the background agree very well.

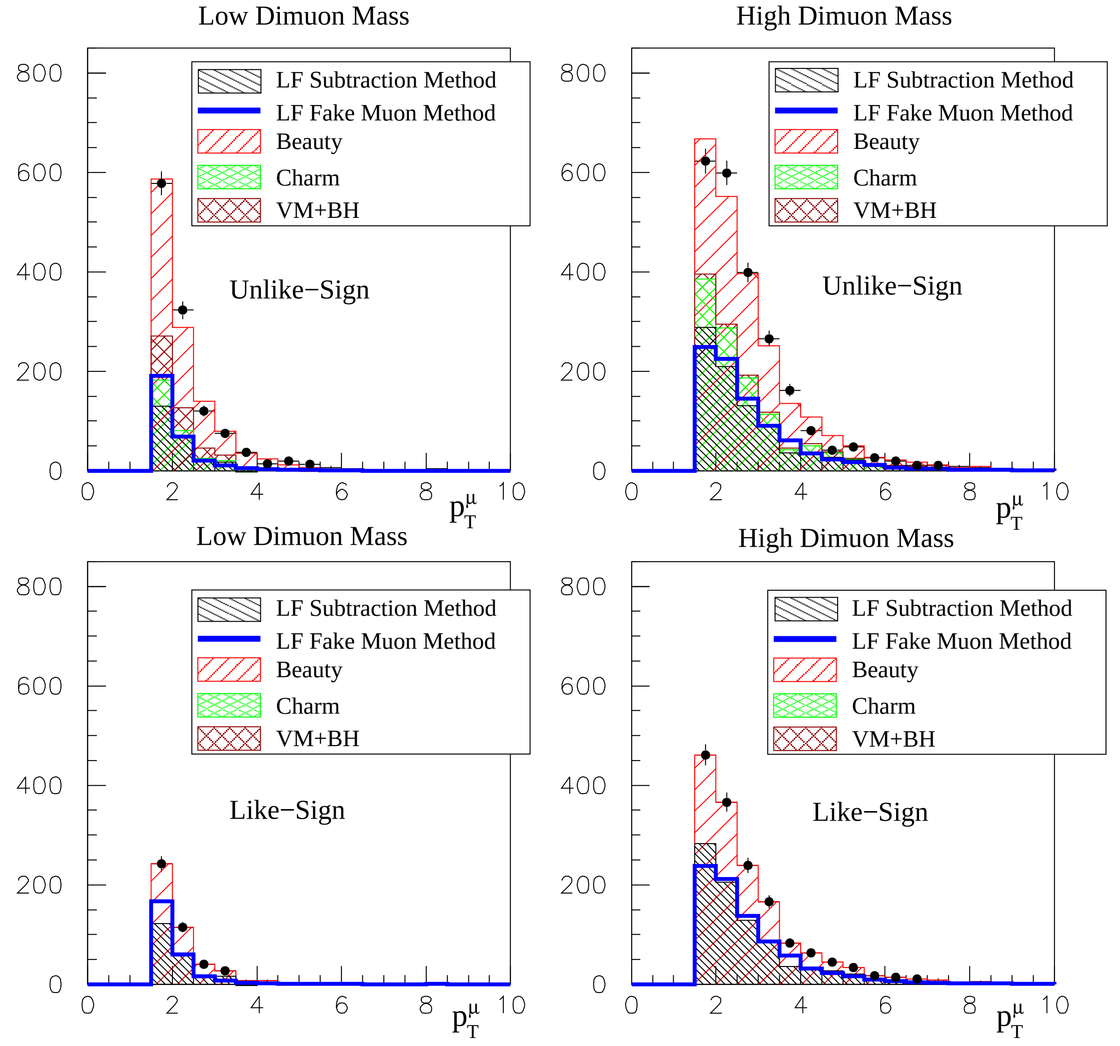

Figure 8.9: Dimuon analysis: p_T^μ distribution non-isolated muons: the left plots are for low dimuon mass muons and the right plots for high dimuon mass muons. The upper plots show the unlike-sign charge combinations and the lower plots the like-sign combinations. The points are the data, the different hashes represent the contribution from beauty, charm, vector mesons (VM) and Bethe-Heitler (BH) and the background. On top of it the background distribution using the fake-muon probabilities is drawn as a blue thick solid line. In both samples the two methods to estimate the background agree very well.

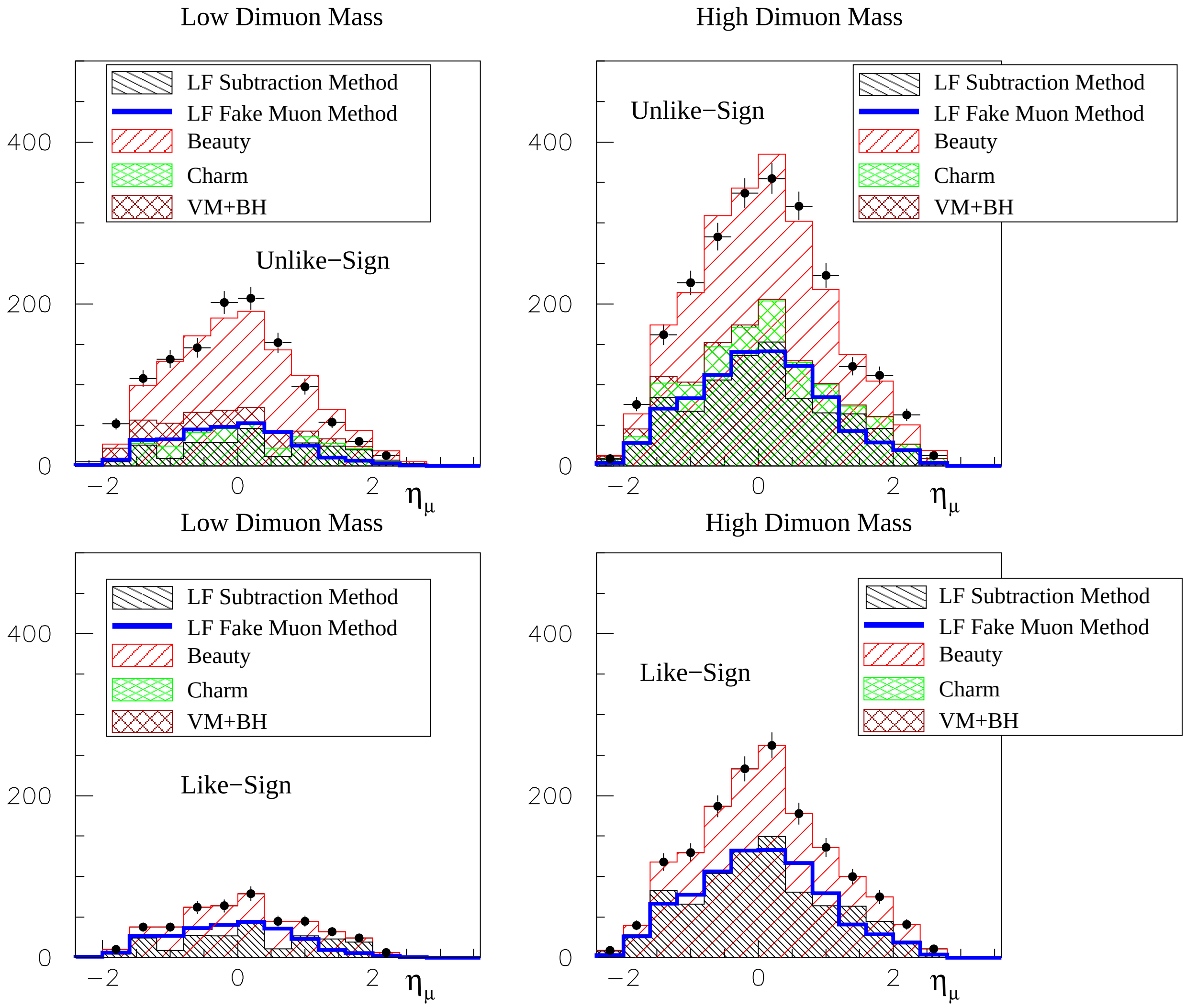

Figure 8.10: Dimuon analysis: η^μ distribution:the left plots are for low dimuon mass muons and the right plots for high dimuon mass muons. The upper plots show the unlike-sign charge combinations and the lower plots the like-sign combinations. The points are the data, the different hashes represent the contribution from beauty, charm, vector mesons (VM) and Bethe-Heitler (BH) and the background. On top of it the background distribution using the fake-muon probabilities is drawn as a blue thick solid line. In both samples the two methods to estimate the background agree very well.

9. Cross-Section Measurement

This chapter describes the measurement of the beauty-quark photoproduction cross-section in the semi-leptonic muon decay channel. The statistics after the event selection are a factor 10 higher compared to the previous analysis [88], resulting in a factor 7.5 more selected beauty events. Hence the differential cross-sections can be measured in a finer binning than the previous analysis and for the first time beauty dijet-correlation cross-sections are measured at ZEUS separately in the direct-enriched and resolved-enriched regions. The measurements are first compared to the LO+PS PYTHIA Monte Carlo followed by a comparison to two different sets of NLO predictions provided by the FMNR program.

9.1. Determination of the Cross-Sections

The cross-section, σ, of a process, p, is defined as the number of events produced in this process per integrated luminosity L:

$$\sigma_p = \frac{N_p}{L} \; . \tag{9.1}$$

In order to measure the cross-section of the process

$$ep \to eb\bar{b}X \to e\mu\text{jet}X' \; , \tag{9.2}$$

in the photoproduction regime, the fraction of events in the data sample coming from this process has to be determined. The cross-section of beauty-quark production, σ_b, is therefore determined using the following relationship:

$$\sigma_b = \frac{N^{\text{data}} \cdot f_b}{L \cdot \mathcal{A}} \; . \tag{9.3}$$

N^{data} denotes the number of selected events in the data sample and f_b is the fraction of beauty events in the data sample determined using a fit of the p_T^{rel} variable as described in Chapter 7. The acceptance, $\mathcal{A}$, defined as in Equation 9.4 using two different counting methods:

$$\mathcal{A} = \left(\frac{N_{\text{reconstructed}}}{N_{\text{true}}} \right)^{\text{beauty MC}} \; . \tag{9.4}$$

- For the event-wise cross-sections the number of reconstructed events is divided by the true (generator level) number of events fulfilling the event selection on true level in the signal Monte Carlo;

- For the particle-wise or muon cross-section the number of reconstructed muon-jet associations is divided by the true (generator level) number of muon-jet associations from beauty quarks.

In order to have a measure of the extrapolation from reconstructed events to true events, the purity is used, defined as the fraction of true events which are also reconstructed in the reconstructed sample:

$$\text{purity} = \frac{N_{\text{rec \& true}}}{N_{\text{rec}}} \ . \tag{9.5}$$

9.2. The Visible Cross-Section

The PYTHIA beauty Monte Carlo described in Section 6.1 is used to determine the acceptance. All events containing a beauty quark or anti-quark, as well as a muon matched to a jet in the following kinematic range are defined as signal: Beauty from gluon splitting is not explicitly excluded, but the fraction in the beauty Monte Carlo is negligible.

- **Photoproduction selection:**

$$Q^2 < 1\,\text{GeV}^2 \ , \tag{9.6}$$

$$0.2 < y < 0.8 \ . \tag{9.7}$$

- **Dijet selection:** at least two MC true jets:

$$p_T^{jet_{1(2)}} \geq 7(6)\,\text{GeV} \ , \tag{9.8}$$

$$|\eta^{jet_{1(2)}}| < 2.5 \ . \tag{9.9}$$

- **Muon selection:** at least one muon originating from a beauty quark:

$$p_T^{\mu} \geq 1.5\,\text{GeV} \ , \tag{9.10}$$

$$-2.0 \leq \eta^{\mu} \leq 2.5 \ . \tag{9.11}$$

- **Muon-Jet association:** For the particle-wise cross-sections a muon-jet association is required

$$\Delta R^{\mu\text{-jet}} < 1 \ . \tag{9.12}$$

The fraction of signal events is determined using this selection and the global p_T^{rel}-fit. The result is shown in Figure 7.5. The total particle-wise visible cross-section is determined to be

$$\sigma_{\text{total}}^{\text{vis}} = 105.4 \pm 6.1^{+17.4}_{-16.3}\,\text{pb} \ , \tag{9.13}$$

where the first error is statistical and the second is systematic as discussed in the next section. The measured cross-section is 1.43 times higher than the PYTHIA prediction. The total cross-section was also calculated for $p_T^{\mu} > 2.5\,\text{GeV}$ to compare it to the previous measurement [88] and was found to be in very good agreement.

9.3. Systematic Uncertainties

The systematic error arising from the event reconstruction and the beauty fraction extraction using the p_T^{rel} method are determined by varying the following procedures and corrections. The total systematic error is the quadratic sum of the individual changes in the cross-section due to the variation.

Charm p_T^{rel} shape correction: The correction for the difference in the shape of the light flavour MC sample is also used for the charm MC samples. For the correction of the charm p_T^{rel} shape, 50% of the correction is applied to the MC samples. As a systematic check, the full p_T^{rel} correction is applied and no correction is applied. The effect on the total cross-section is $^{+7.5}_{-6.4}\%$.

Light Flavour p_T^{rel} shape correction: To account for the uncertainty of the p_T^{rel} shape correction, the correction applied to the light flavour Monte Carlo sample has been varied between 80% and 120%, leading to an additional systematic error $^{+10.4}_{-10.1}\%$.

Charm normalisation: The absolute normalisation of the charm Monte Carlo after the fit is in agreement with the scale-factor measured in a charm analysis in a similar kinematic range [42]. The error on the cross-section from this measurement is about 15 %, the error on the effective $c \rightarrow \mu$ branching ratio is 5%. The $c \rightarrow D^*$ fragmentation fraction in PYTHIA is in agreement with the measured values with an error of 2% [93]. In order to take into account the uncertainty of the charm normalisation the relative charm to light flavour ratio was varied by 20%. The effect on the total cross-section of this variation is $^{+6.0}_{-6.8}\%$.

Statistical uncertainty of muon efficiency correction: To estimate the influence of the statistical uncertainty of the muon efficiency correction, the muon efficiency correction factors were varied 10 times randomly within their statistical errors. The systematic effect is calculated as root mean square of the 10 measurements. The systematic effect of this variation on the total cross-section is 2%.

A second test was performed using muon efficiency correction tables from an independent analysis using the same evaluation method for the correction factors. At the same time a different binning was used. The effect of applying these correction factors to the total cross-section is ±2% and was added to the systematic error.

Systematic uncertainty of muon efficiency correction: To get an idea of the systematic uncertainty of the muon efficiency correction one would want to adjust the muon finder correction factors in order to get the same cross-section for each finder combination in the same geometrical range (forward,barrel, rear). This is not easily possible due to correlations between the different finder combinations. Therefore another approach was followed: the cross-section has been determined using all muons found by the muon chambers regardless of the BAC information and using the BAC regardless of the muon chamber information. The deviations from the nominal value of the cross-section were then taken as an estimate of the systematic error due to the muon efficiency correction. The error on the total cross-section is $^{+8.7}_{-7.2}\%$.

Fake muon efficiency correction: The muon efficiency was determined from real muons and in the analysis applied to real and fake muons. Assuming that the muon efficiency for real muons is correct, the analysis has been reweighted in order to get agreement between data and Monte Carlo in the muon finder combinations by applying additional weights to fake muons in the analysis. This has an effect of ±1.9% on the total cross-section.

Direct and non-direct contributions: The non-direct contributions (low x_γ^{obs}) in the data are substantially higher than the Monte Carlo predictions. The x_γ^{obs} variable is used to distinguish between direct-enriched and non-direct-enriched cross-section measurements. Therefore a reweighting of x_γ^{obs} has been performed and the difference of the cross-section from the nominal value is taken as systematic uncertainty due to this effect. The systematic uncertainty of the total cross-section due to this effect is ±1.8%.

Jet-energy scale: The uncertainty of the jet energy scale was determined to be ±3 % [43] in photoproduction events. In order to estimate the effect on the cross-section, the energy of jets in the Monte Carlo was varied up and down by $\pm 3, 6, 9\%$, while leaving the energies unchanged in the data. A linear fit was performed and the cross-section value at ±3% variation was taken as estimate of the systematic uncertainty. The effect on the total cross-section is ±2%

9.4. Differential Cross-Sections

For the differential cross-sections a separate p_T^{rel} fit is performed in each bin of the differential cross-section and the shape of the p_T^{rel} background distribution is corrected separately for each p_T^{rel} fit, see Section 7.1.1. The cross-section is then defined as:

$$\frac{d\sigma_b}{dx} = \frac{N^{\text{data}} \cdot f_b}{L \cdot \mathcal{A} \cdot \text{binwidth}} \; . \tag{9.14}$$

The systematic error is extracted separately for each cross-section bin. For the systematic error due to the jet-energy scale uncertainty a global error of 2% is applied.

Before comparing the data to the next-to-leading order predictions, a comparison with the LO+PS MC with statistical errors only is shown. The acceptances for the cross-section measurement are extracted from the signal Monte Carlo, hence a good description of the shape of the distributions by the Monte Carlo is essential. LO+PS Monte Carlo generators only describe the shapes of the distributions, therefore the absolute normalisation was taken from the global p_T^{rel}-fit. All following Monte Carlo cross-sections are scaled by the factor of 1.43 obtained from the global p_T^{rel}-fit.

In a first step the muon and muon-jet cross-sections were measured to establish the event selection, as these cross-section have been measured before. The statistics are much higher therefore it was possible to measure the cross-sections in a much finer binning. The first set of plots, Figure 9.1 shows the cross-section, acceptances, efficiencies and purities in bins of p_T^μ. The number of bins has been increased from 3 to 8 with respect to the previous analysis. The measured cross-sections agree well with the scaled predictions and the acceptance, efficiency and purity have reasonable values. The efficiency drops a little for low p_T^μ values. These are muons that do not reach the outer muon chambers.

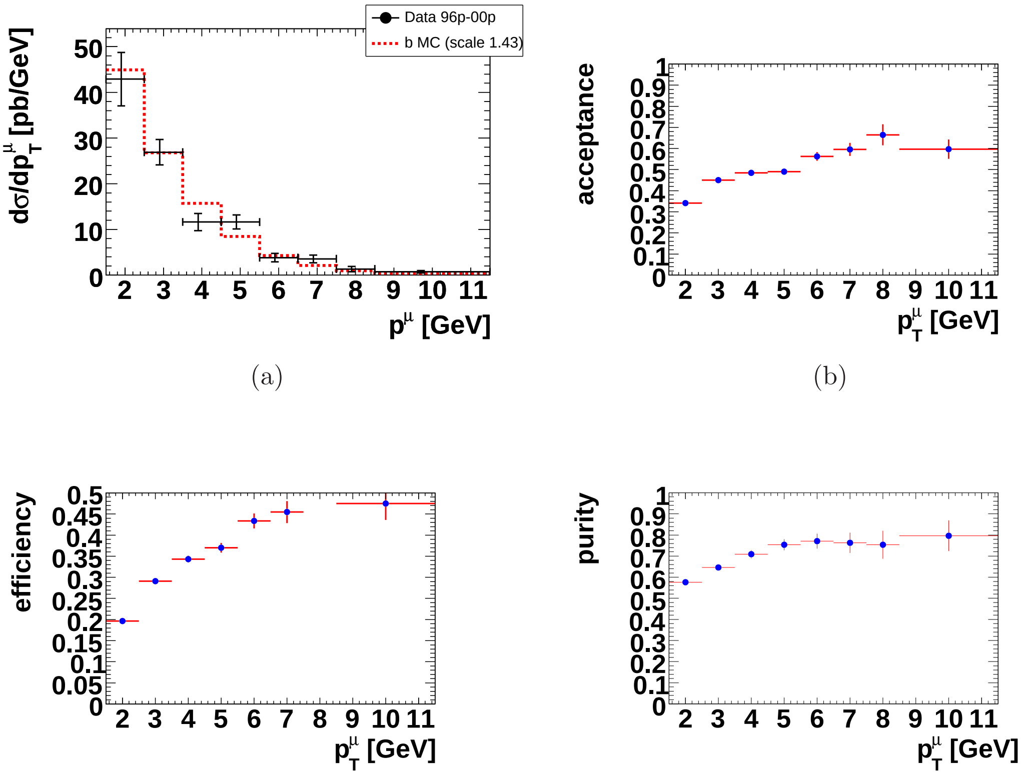

(a) (b)

(c) (d)

Figure 9.1: Cross-section as a function of p_T^μ: Shown are (a) the comparison of the measured cross-section and the predictions by the Monte Carlo scaled by a factor of 1.43 (b) the acceptance, (c) the efficiency, and (d) the purity of the measurement.

The cross-section as a function of η^μ, see Figure 9.2, has been measured in 8 differential bins. The measurement in the region between 0.5 and 1 is 2σ below the prediction. The acceptance and also the fit did not show any noticeable problems. The only explanation is therefore a statistical fluctuation. The measurement in the forward region is higher than the prediction. This has also been the case in a previous analysis. The acceptance drops in this region due to the harder cuts on the reconstructed muons in the forward region. Part of this discrepancy might be due to statistical fluctuations, another reason could be a difference in the muon efficiency in data and Monte Carlo or a wrong cross-section in the Monte Carlo. Several tests have been performed to determine the systematic error of the muon efficiency correction, see Section 9.3.

The cross-section as a function of $p_T^{\mu\text{-jet}}$ agrees well with the LO+PS Monte Carlo and also acceptance, efficiency and purity have reasonable values, see Figure 9.3.

The measurement as a function of $\eta^{\mu\text{-jet}}$, see Figure 9.4, shows the same behaviour as the cross-section in bins of η^μ. This is not surprising, as the the jet has to be associated to a muon.

In the cross-section measurement in bins of x_γ^{obs}, see Figure 9.5, an excess in the

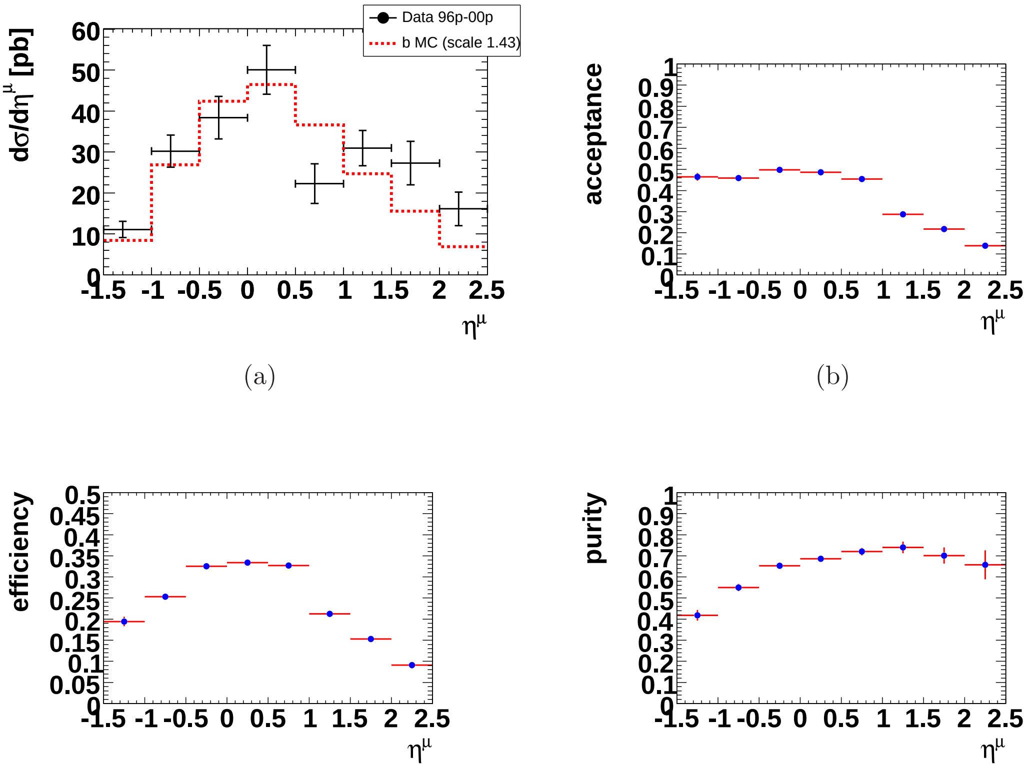

(a) (b)

(c) (d)

Figure 9.2: Cross-section as a function of η^μ: Shown are (a) the comparison of the measured cross-section and the predictions by the Monte Carlo scaled by a factor of 1.43, (b) the acceptance, (c) the efficiency, and (d) the purity of the measurement.

non-direct region ($x_{\gamma^{obs}} < 0.75$) is observed. x_γ^{obs} is used to distinguish between direct- and non-direct processes. While the efficiency of the x_γ^{obs} cross-section is flat, the acceptance rises in the bin before last and drops in the last bin. This behaviour is due to migration effects at the transition between the direct-enriched and non-direct-enriched regions.

The cross-sections of the dijet correlation measurements are compared to PYTHIA and NLO QCD predictions at the same time only. The plots are shown in Section 9.5. The acceptances and purities are given together with the cross-section numbers in Appendix F.

9.5. Comparison to NLO

9.5.1. FMNR NLO parameters

For the comparison with theory the FMNR program described in Section 2.6 was used. This program produces series of $b\bar{b}$ or $c\bar{c}$ events with two or three partons in the

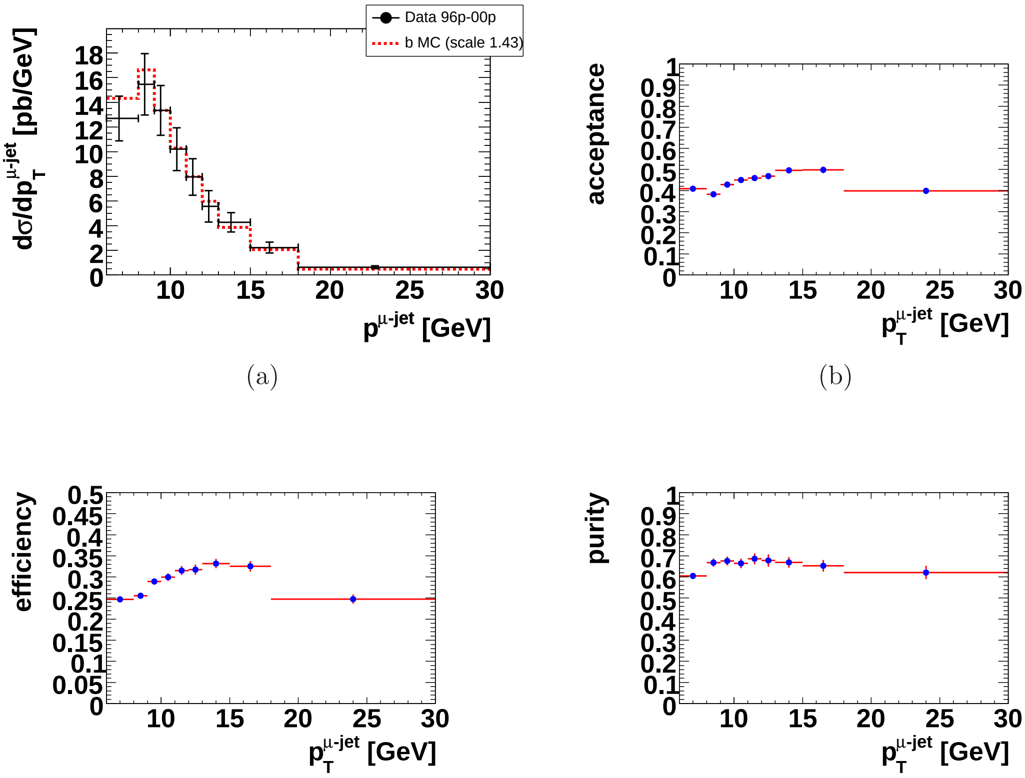

(a) (b)

(c) (d)

Figure 9.3: Cross-section as a function of $p_T^{\mu\text{-jet}}$: Shown are (a) the comparison of the measured cross-section and the predictions by the Monte Carlo scaled by a factor of 1.43, (b) the acceptance, (c) the efficiency, and (d) the purity of the measurement.

final state. The beauty or charm hadrons are then obtained by rescaling the three-momentum of the quark using the Peterson fragmentation function, Equation 2.34. Afterwards the hadron is decayed semi-leptonically into a muon using the decay spectrum from PYTHIA. Jets are obtained by running the k_t algorithm on the outgoing partons. The FMNR cross-section can be separated in a point-like cross-section, where the photon is a point-like particle, as in the direct processes, and a hadron-like cross-section, where the photon acts as a source of partons, like in the resolved and photon-excitation processes. The cross-sections calculated by FMNR are at parton-level, while the measured cross-sections are on hadron level. In order to compare the FMNR predictions to the measurement the cross-sections are transformed into hadron-level cross-sections applying the ratio of hadron-level to parton-level cross-section in PYTHIA to each bin of the FMNR predictions. The global correction factor is 0.9 and flat in most variables. The correction factor in each bin is given together with the cross-section numbers in Appendix F.

Two sets of FMNR predictions are calculated: The first set of parameters summarised in Table 9.1 uses the FMNR parameter settings and variations used in the

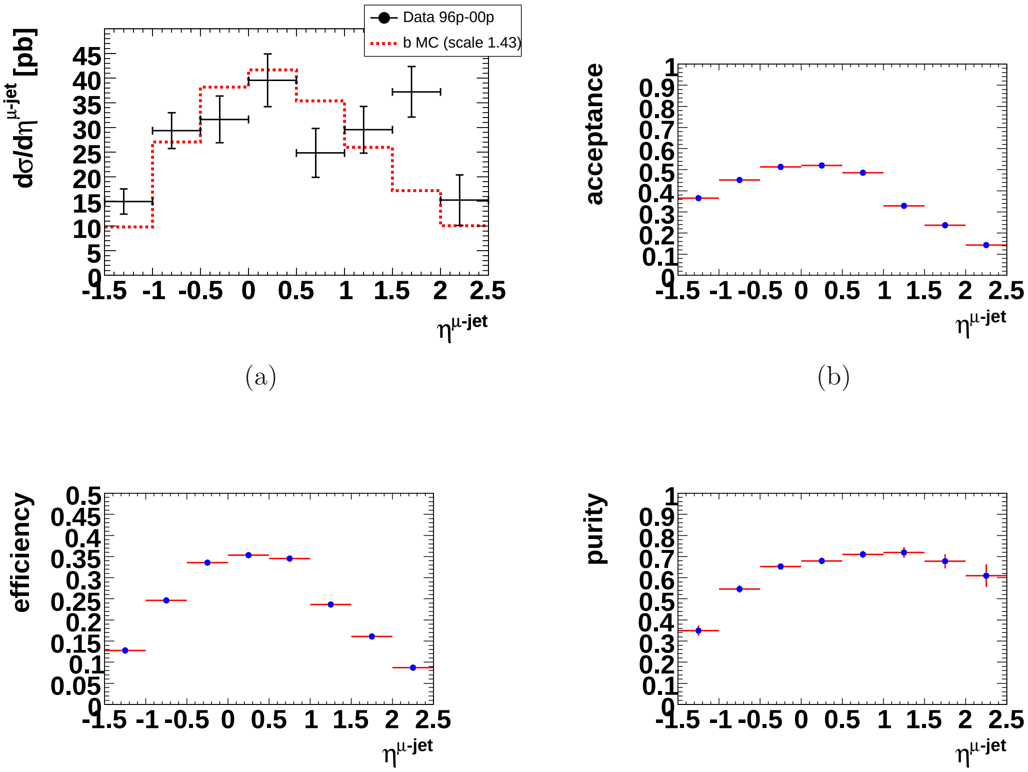

(a) (b)

(c) (d)

Figure 9.4: Cross-section as a function of $\eta^{\mu\text{-jet}}$: Shown are (a) the comparison of the measured cross-section and the predictions by the Monte Carlo scaled by a factor of 1.43, (b) the acceptance, (c) the efficiency, and (d) the purity of the measurement.

previous analysis, while for the second set of parameters the scale has been lowered to $\mu = \mu_0/2$ and the hadron-like part of FMNR has been doubled. The first change is motivated by theory: the calculated cross-section should be scale-independent, which is not the case for fixed-order calculations. Therefore the chosen scale should be very insensitive to scale variations or the calculated cross-section should converge as fast as possible including higher order corrections. In many cases $\mu = \mu_0/2$ is a better choice compared to the *natural* scale $\mu = \mu_0$ [94]. The second change is motivated by the data - comparison with the NLO QCD prediction in the low x_γ^{obs} region and will be explained more explicitly in the next section. For the theoretical uncertainty the same variations as for the standard predictions have been used, scaling the renormalisation and factorisation scale up and down by a factor two.

9.5.2. Dijet Correlation Measurements and Comparison to NLO

Dijet correlations are particularly sensitive to higher-order effects and therefore suitable to test the limitations of fixed-order perturbative QCD calculations. $\Delta\phi^{jj}$ is

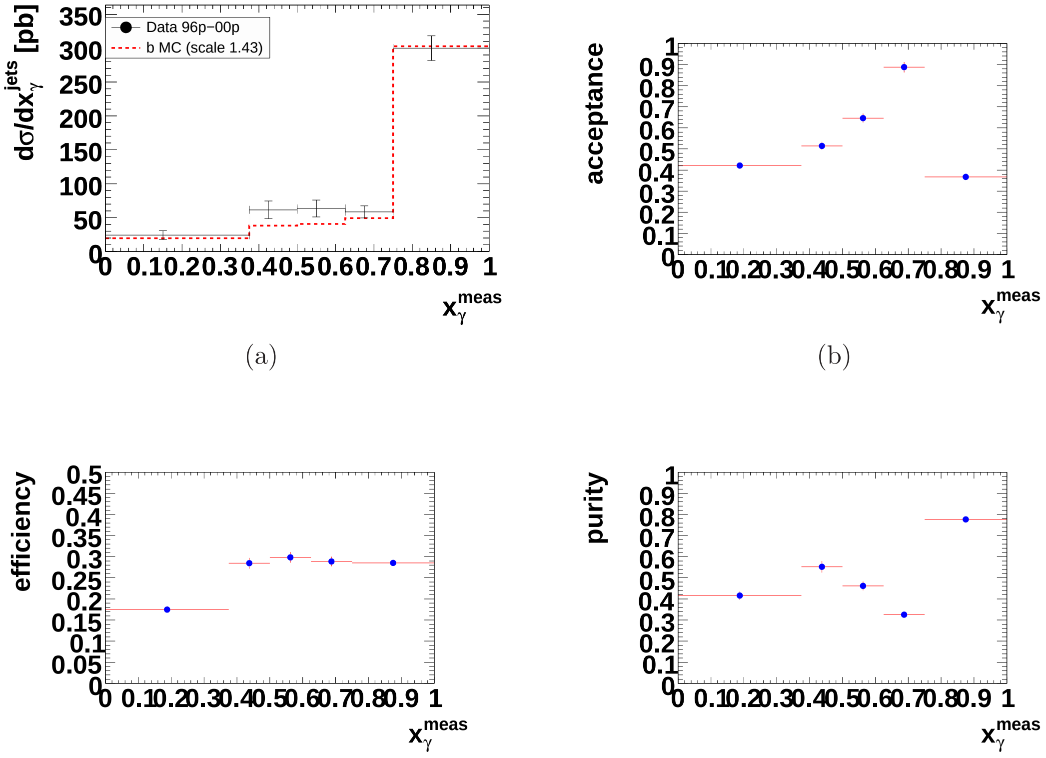

(a) (b)

(c) (d)

Figure 9.5: Cross-section as a function of x_γ^{meas}: Shown are (a) the comparison of the measured cross-section and the predictions by the Monte Carlo, (b) the acceptance, (c) the efficiency, and (d) the purity of the measurement.

defined as the azimuthal angle between the two highest p_T jets, $\Delta\phi^{jj} = (\phi_1^j - \phi_2^j)$. The cross-section as a function of $\Delta\phi^{jj}$ is shown in Figure 9.6. The agreement between the measurement and the PYTHIA Monte Carlo is reasonable given the large errors. The Monte Carlo distribution for the direct-enriched region ($x_\gamma^{obs} > 0.75$), see Figure 9.6 (e, f), falls off more rapidly than the data and lies significantly below the data, indicating that the higher order contributions to the cross-section are not well simulated in the parton showering of the PYTHIA Monte Carlo. This effect has already been observed in the charm measurement, see Figure 3.11.

The NLO QCD predictions describe the data within errors, see Figure 9.6. Using the natural scale the measurement is mostly above or at the upper edge of the predictions, see Figure 9.6 (a, c, e), while moving the renormalisation and factorisation scales to $\mu_{R,F} = \mu_0/2$, give a clearly better agreement between data and NLO, see Figure 9.6 (b, d, f).

Comparing the data-NLO ratio for direct enriched and non-direct-enriched regions separately, the ratio is clearly higher in the non-direct case. The difference is most visible in the last bin of $\Delta\phi^{jj}$, with two back-to-back jets and a photon remnant

FMNR Standard Parameters		
Parameter	Variation	
$m_b = 4.75\,\text{GeV}$	$m_b = 4.5\,\text{GeV}$	$m_b = 5\,\text{GeV}$
$\mu = \mu_0 = \sqrt{\frac{1}{2}(p_t^b)^2 + \frac{1}{2}(p_t^{\bar{b}})^2 + m_b^2}$	$\mu = \mu_0/2$	$\mu = 2\mu_0$
PDF(p)= CTEQ5M [95]	MRST [96]	
PDF(γ)=GRV-G HO [97]	AFG [98]	
Peterson fragmentation	Kartelishvili	
$\epsilon_b = 0.0035$	$\epsilon_b = 0.002$	$\epsilon_b = 0.0055$
$\Lambda_{QCD} = 0.226\,\text{GeV}$	$\Lambda_{QCD} = 0.2\,\text{GeV}$	$\Lambda_{QCD} = 0.25\,\text{GeV}$

Table 9.1: FMNR standard parameter settings and variations.

resulting in a low x_γ^{obs}. The hadron-like contribution in the NLO cross-section is negligible in the direct enriched region, while it is an important fraction of the non-direct-enriched NLO cross-section, especially for large angles where the agreement is worst, see Figure 9.6 (c, d). This indicates that the hadron-like component of the NLO predictions, which is proportional to the gluon content of the photon, might be underestimated by the NLO calculations. The gluon content of the photon is difficult to measure and has large uncertainties. Therefore together with the change of scale, the hadron-like component was increased by a factor of two. This leads to a better agreement between data and NLO QCD predictions in the non-direct region in all measured cross-sections.

The cross-section measurement in bins of the transverse momentum of the dijet system, $(p_T^{\text{jets}})^2$, is correlated to the azimuthal angle between the two highest jets and shows therefore the same agreement and disagreement as the $\Delta\phi^{jj}$ variable. The cross-section spectrum is harder in the data than in the Monte Carlo especially in the direct-enriched region, while the non-direct part agrees well in shape, see Figure 9.7. The NLO predictions describe the data, although a change in scale and an increase of the hadron-like component leads to a better agreement.

ΔR^{jj} is defined as the distance between the two highest p_T jets in the $\eta - \phi$ plane, $\Delta R^{jj} = \sqrt{(\phi_1^j - \phi_2^j)^2 + (\eta_1^j - \eta_2^j)^2}$. The cross-section measured in the whole x_γ^{obs} region agrees well with the predictions from the Monte Carlo, while there are differences in shape in the direct-enriched and non-direct-enriched regions, see Figure 9.8, due to higher order contributions not simulated in the Monte Carlo, as seen in the $\Delta\phi^{jj}$ cross-section. The ΔR^{jj} variable is related to the $\Delta\phi^{jj}$ variable. Therefore it is not surprising that the same behaviour as in $\Delta\phi^{jj}$ can be observed. Comparing to the standard NLO calculations the measurement is always above or at the upper edge of the predictions and the agreement in the low x_γ^{obs} region is better using the increased hadron-like cross-section.

The measurement of the dijet mass, M^{jj}, agrees well with the predictions from the Monte Carlo, see Figure 9.9. In the last bin of the direct-enriched region the statistics were too low to determine the beauty fraction. The comparison to NLO is substantially improved using the new parameter set of FMNR, see Figure 9.9.

The variable $\cos\theta^*$ describes the scattering angle of the dijet system with respect to the proton axis in the dijet rest frame:

$$\cos\theta^* = \tanh\left(\frac{\eta^{\mu\text{-jet}} - \eta^{\text{jet2}}}{2}\right) . \tag{9.15}$$

In this case the dijet system is defined as the muon-jet and the highest p_T^{jet} other jet and the variable is filled for all muon-jet associations in the event. This definition allows to distinguish between the tagged beauty quark being produced in the proton (positive values of $\cos\theta^*$) or in the photon direction (negative values of $\cos\theta^*$) and can therefore give indications of the production process. While the cross-sections as a function of $\Delta\phi^{jj}, (p_T^{\text{jets}})^2, \Delta R^{jj}, M^{jj}$ are event-wise cross-sections, the $\cos\theta^*$ variable is filled for all muon-jet associations and is therefore a particle-wise cross-section.

Direct beauty events originate from the dominant quark-exchange process $\gamma g \rightarrow b\bar{b}$ and are expected to be symmetric in $\cos\theta^*$. Non-direct events are mainly in photon direction consistent with a dominant contribution from gluon exchange, giving a strong rise in the photon direction of $\cos\theta^*$. The cross-section prediction from the Monte Carlo and the NLO calculations for direct-enriched and non-direct-enriched events reflects this behaviour. A slight asymmetry can be observed in the direct-enriched region, coming from the contamination with non-direct events. In the charm measurement, see Section 3.4.2, additional cuts were applied on the dijet mass and the average longitudinal boost in order to get rid of biases coming from explicit cuts on p_T^{jet} and η^{jet}. This cannot be done in the case of beauty as the available statistics are not high enough. Comparing the measurement to the predictions, see Figure 9.10, the data seems to be more asymmetric than the predictions, but agrees within errors. Given the large errors on the measurement a conclusive statement on the $\cos\theta^*$ cross-section is not possible and will have to wait for the analysis on the whole HERA I + II analysis (five times more integrated luminosity) and by using the lifetime information as an additional input to the determination of the beauty fraction.

The cross-section in bins of x_γ^{obs}, which has been shown already in Section 9.4, is also compared to the NLO predictions, see Figure 9.11. The improvement of the agreement between measurement and NLO predictions using the new parameter set of FMNR can be clearly seen. The overall normalisation due to the change of scale and the additional effect from the augmentation of the hadron-like FMNR predictions is clearly visible.

In Figures 9.12 and 9.13 the cross-section comparison for the muon and the jet variables are shown. Also in these variables the agreement between data and NLO is improved by the new FMNR parameter set.

9.6. Summary

All measured cross-sections agree within errors with the predictions from the LO+PS scaled Monte Carlo and the next-to-leading-order predictions. Changing the NLO scales from the natural scale μ_0 to $\mu_0/2$, as was proposed for theoretical reasons, improves the agreement in the overall normalisation. The augmentation of the hadron-like cross-section in FMNR, motivated by the measurements in the non-direct-enriched region, improves the agreement between the measured cross-section and the NLO QCD predictions especially for the low x_γ^{obs} cross-section. For a more conclusive statement the analysis should be run on the whole HERA I+II data set taking advantage of the additional lifetime information in the HERA II data. From the theoretical side it is desirable to compare the measurement to a MC@NLO [99], which allows the combination of NLO matrix elements with parton showers, which is so far not available for *ep* collisions.

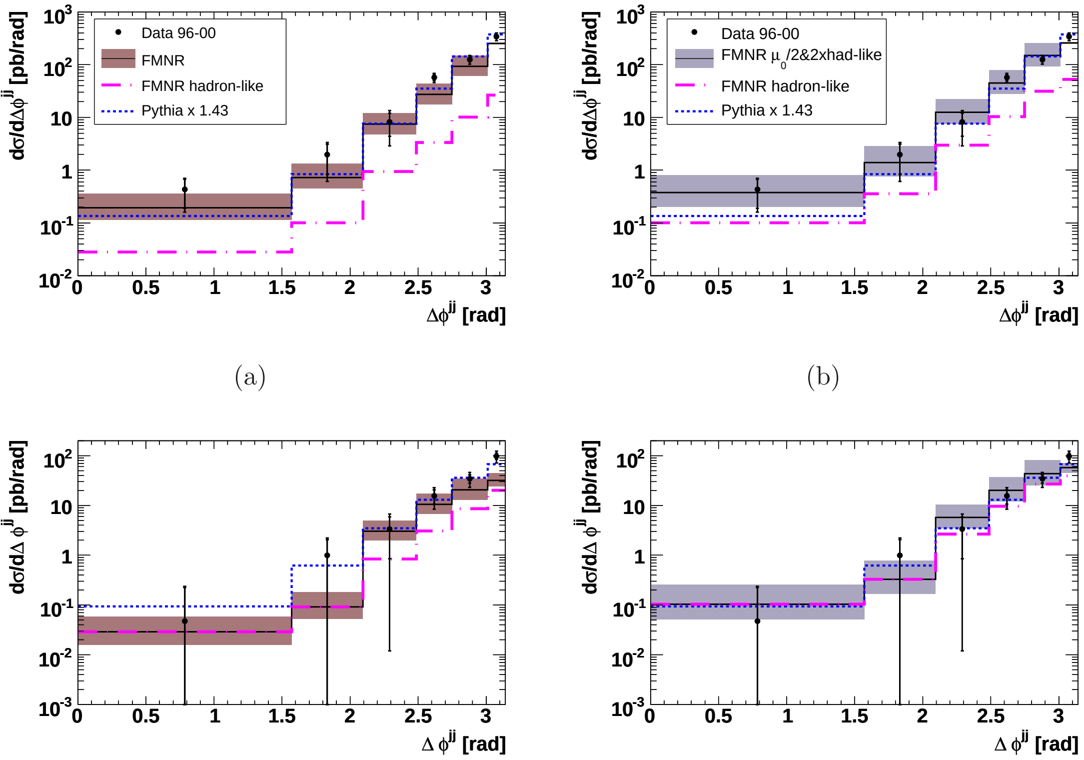

(a)

(b)

(c) non-direct-enriched

(d) non-direct-enriched

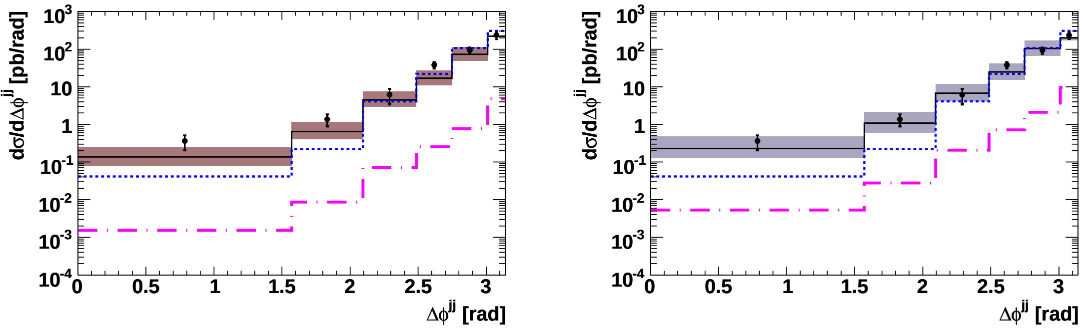

(e) direct-enriched

(f) direct-enriched

Figure 9.6: Cross-section as a function of $\Delta\phi^{jj}$: Shown are the comparisons of the measured cross-section with the predictions by the Monte Carlo and the NLO calculations at hadron level using (a) the standard FMNR parameter set, and (b) the new set of parameters using $\mu_{R,F} = \mu_0/2$ and a doubled hadron-like cross-section. The comparison in the non-direct-enriched region is shown in (c) and (d) and the comparison in the direct-enriched region in (e) and (f).

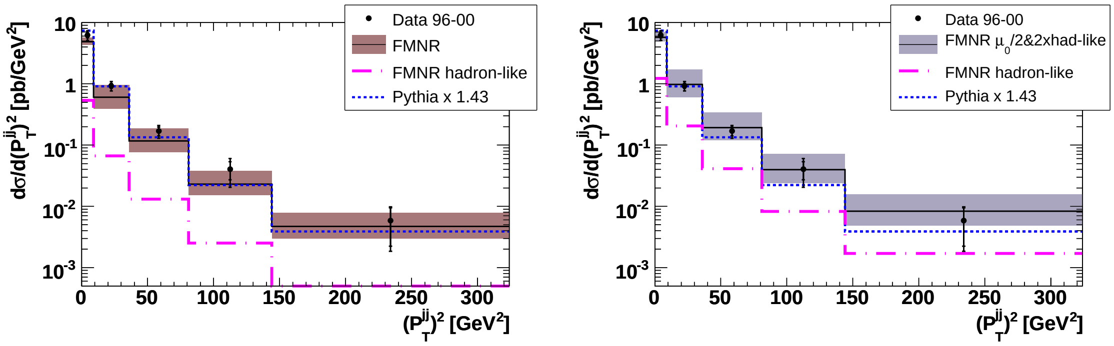

(a)

(b)

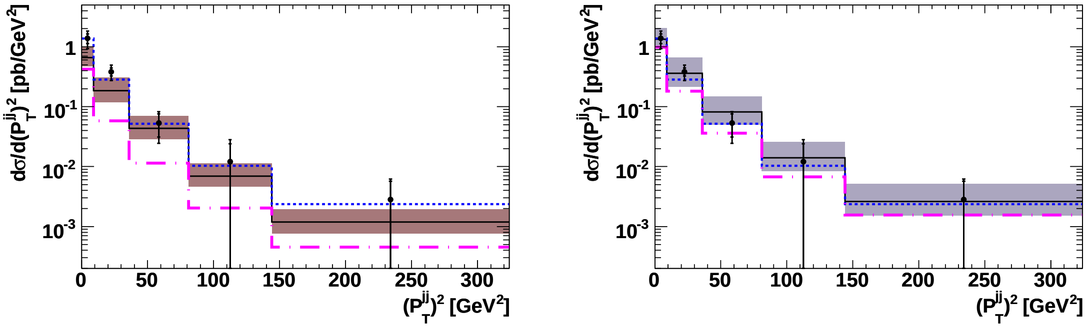

(c) non-direct-enriched

(d) non-direct-enriched

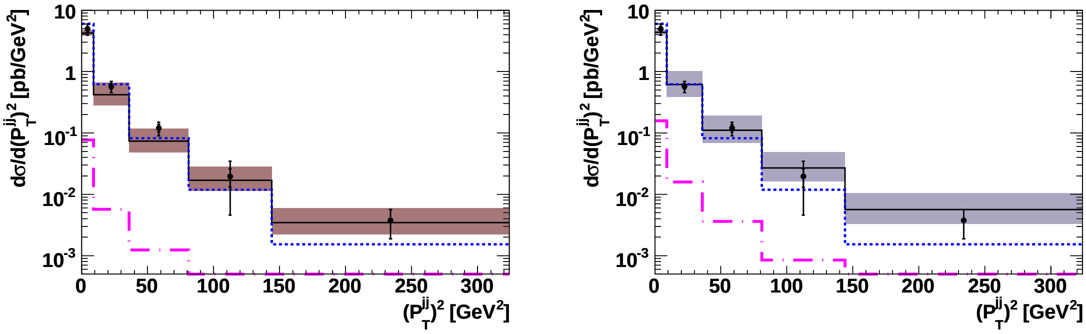

(e) direct-enriched

(f) direct-enriched

Figure 9.7: Cross-section as a function of $(p_T^{\text{jets}})^2$: Shown are the comparisons of the measured cross-section with the predictions by the Monte Carlo and the NLO calculations at hadron level using (a) the standard FMNR parameter set, and (b) the new set of parameters using $\mu_{R,F} = \mu_0/2$ and a doubled hadron-like cross-section. The comparison in the non-direct-enriched region is shown in (c) and (d) and the comparison in the direct-enriched region in (e) and (f).

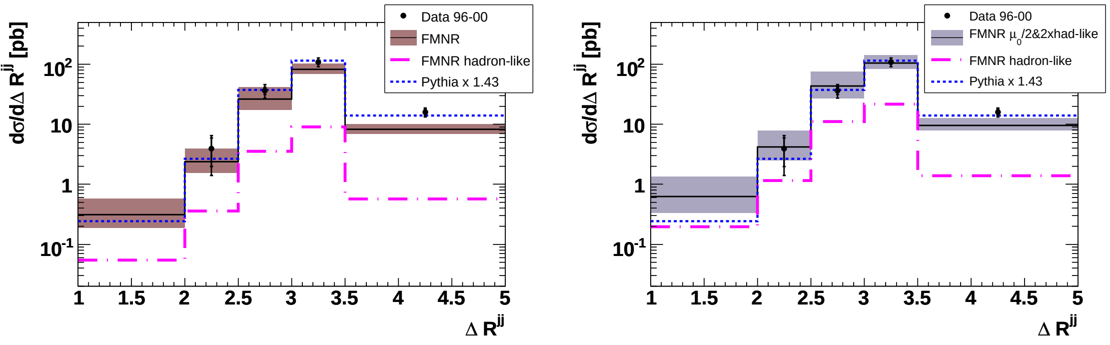

(a)

(b)

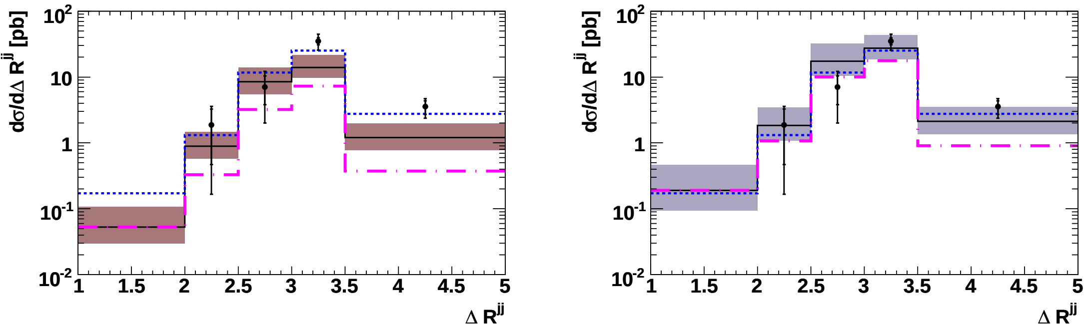

(c) non-direct-enriched

(d) non-direct-enriched

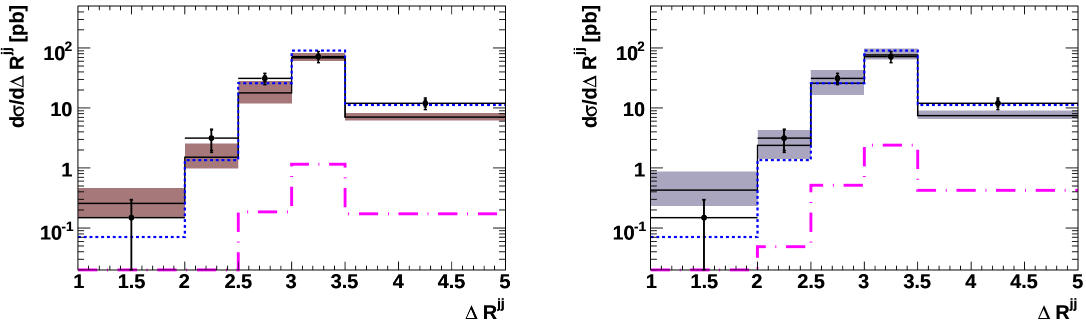

(e) direct-enriched

(f) direct-enriched

Figure 9.8: Cross-section as a function of ΔR^{jj}: Shown are the comparisons of the measured cross-section with the predictions by the Monte Carlo and the NLO calculations at hadron level using (a) the standard FMNR parameter set, and (b) the new set of parameters using $\mu_{R,F} = \mu_0/2$ and a doubled hadron-like cross-section. The comparison in the non-direct-enriched region is shown in (c) and (d) and the comparison in the direct-enriched region in (e) and (f).

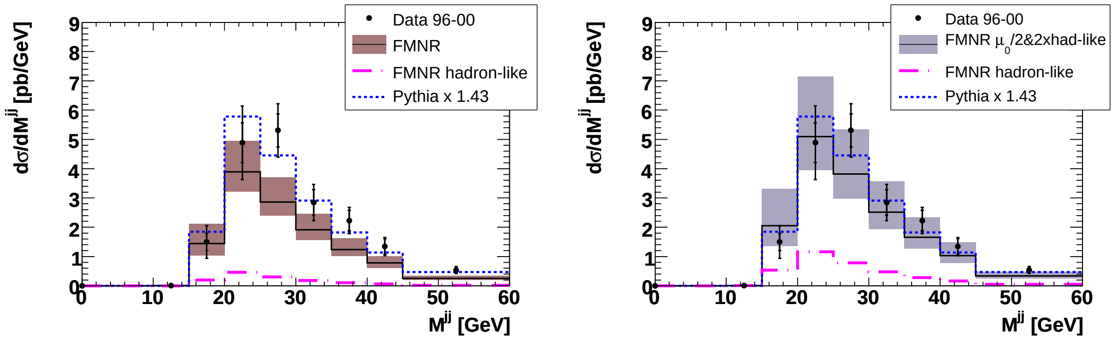

(a) (b)

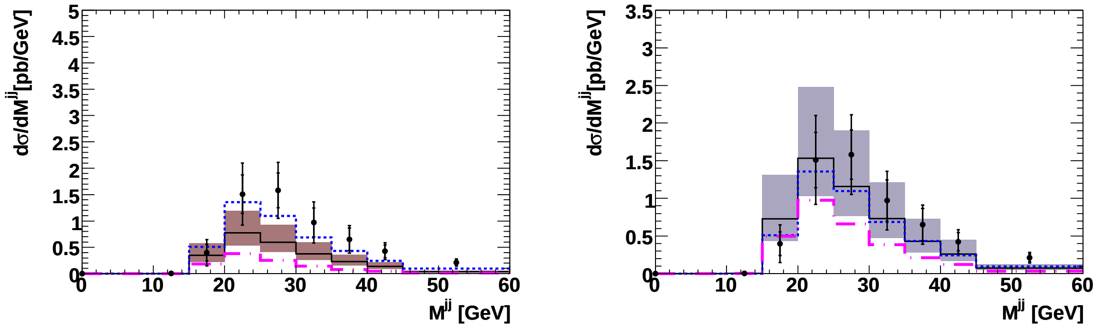

(c) non-direct-enriched (d) non-direct-enriched

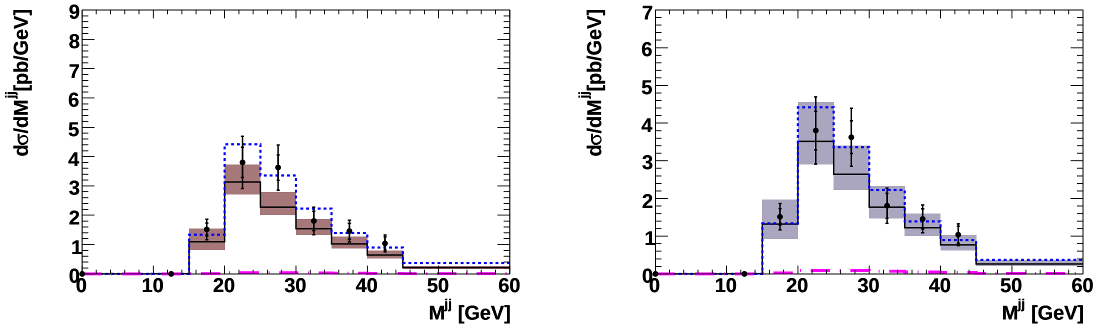

(e) direct-enriched (f) direct-enriched

Figure 9.9: Cross-section as a function of M^{jj}: Shown are the comparisons of the measured cross-section with the predictions by the Monte Carlo and the NLO calculations at hadron level using (a) the standard FMNR parameter set, and (b) the new set of parameters using $\mu_{R,F} = \mu_0/2$ and a doubled hadron-like cross-section. The comparison in the non-direct-enriched region is shown in (c) and (d) and the comparison in the direct-enriched region in (e) and (f).

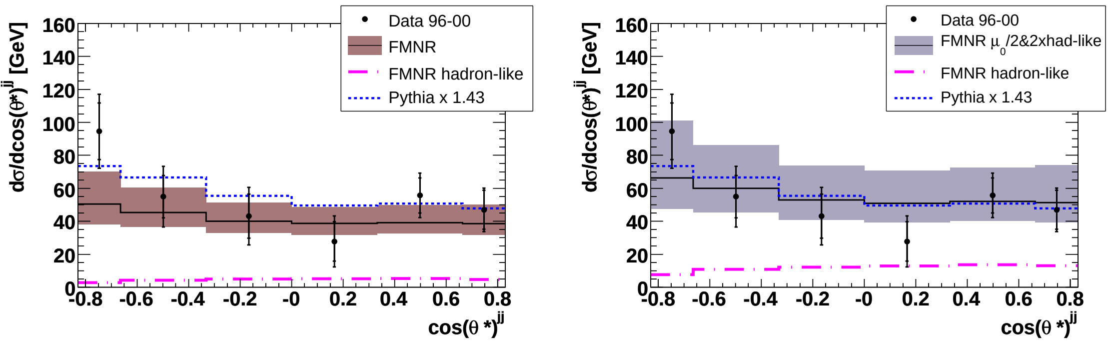

(a)

(b)

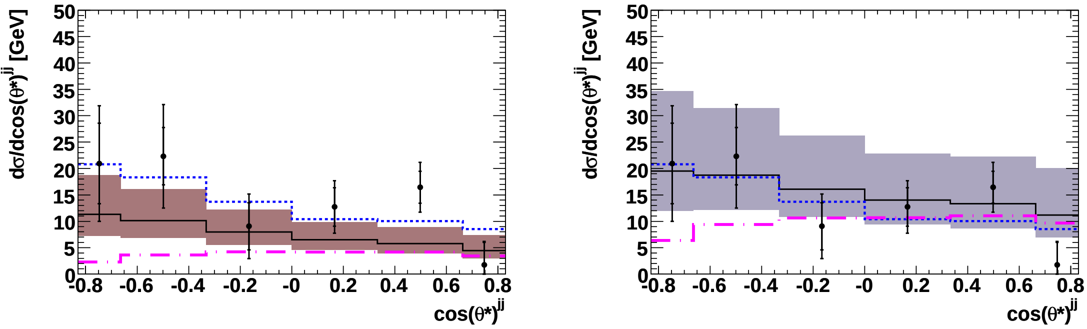

(c) non-direct-enriched

(d) non-direct-enriched

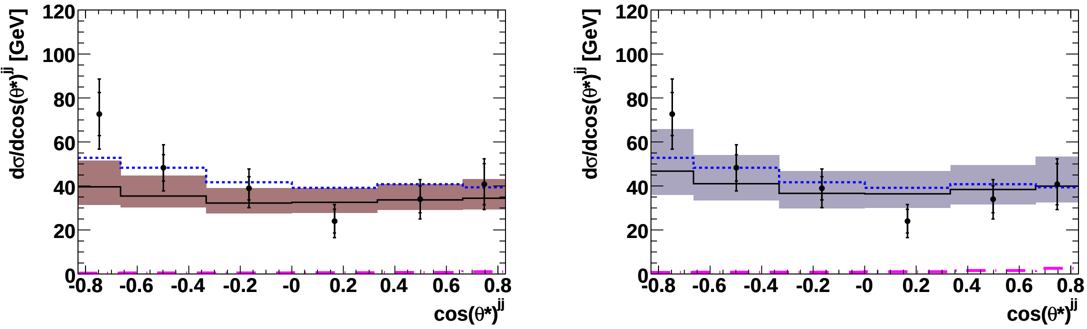

(e) direct-enriched

(f) direct-enriched

Figure 9.10: Cross-section as a function of $\cos\theta^*$: Shown are the comparisons of the measured cross-section with the predictions by the Monte Carlo and the NLO calculations at hadron level using (a) the standard FMNR parameter set, and (b) the new set of parameters using $\mu_{R,F} = \mu_0/2$ and a doubled hadron-like cross-section. The comparison in the non-direct-enriched region is shown in (c) and (d) and the comparison in the direct-enriched region in (e) and (f).

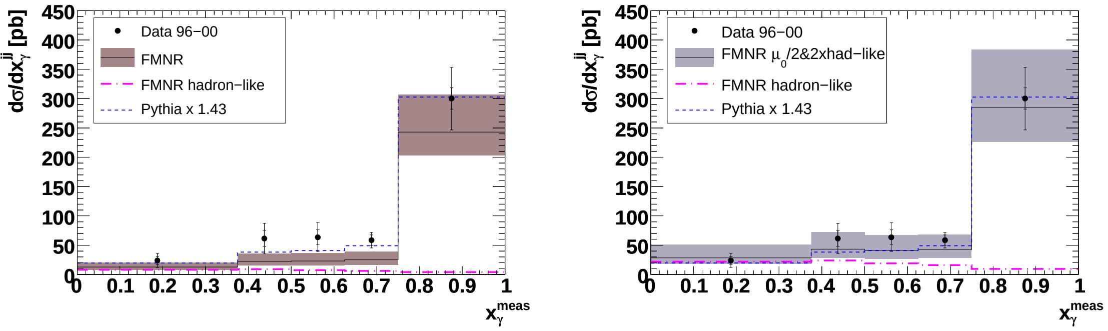

(a) (b)

Figure 9.11: Cross-section as a function of x_γ^{obs}: Shown are the comparisons of the measured cross-section with the predictions by the Monte Carlo and the NLO calculations at hadron level using (a) the standard FMNR parameter set, and (b) the new set of parameters using $\mu_{R,F} = \mu_0/2$ and a doubled hadron-like cross-section.

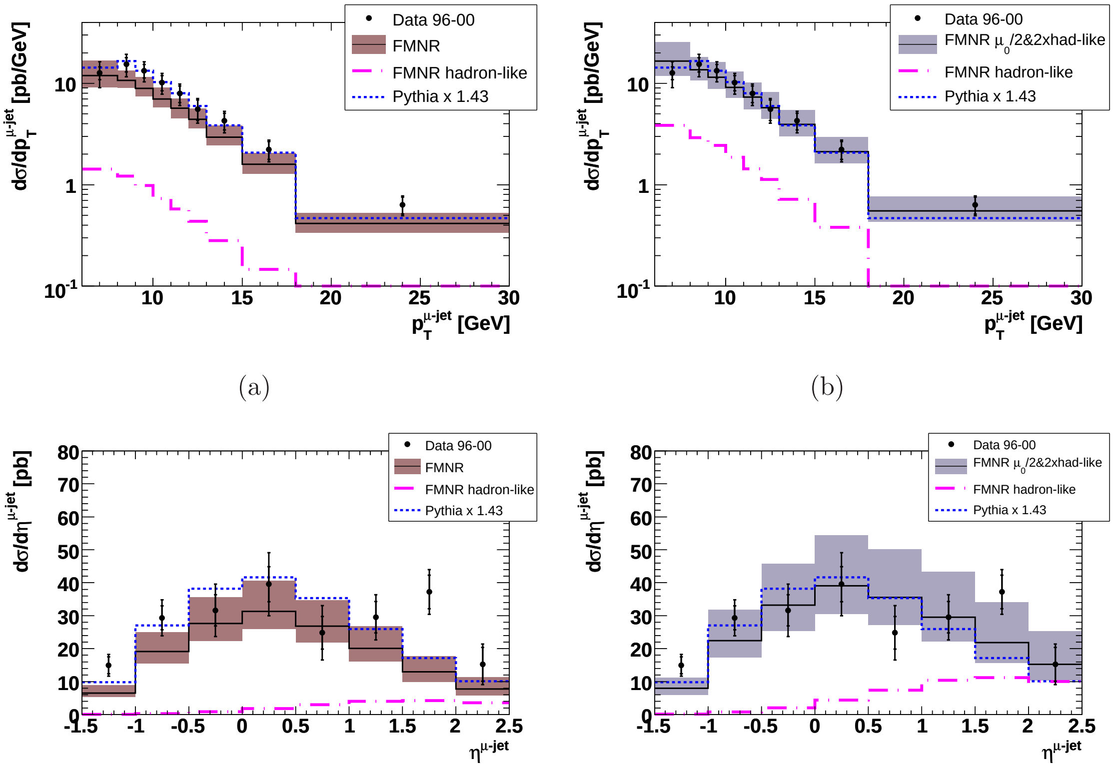

(a) (b)

(c) (d)

Figure 9.12: Cross-section as a function of μ-jet variables,$p_T^{\mu\text{-jet}}$, $\eta^{\mu\text{-jet}}$: Shown are the comparisons of the measured cross-section with the predictions by the Monte Carlo and the NLO calculations at hadron level using (a),(c) the standard FMNR parameter set, and (b),(d) the new set of parameters using $\mu_{R,F} = \mu_0/2$ and a doubled hadron-like cross-section.

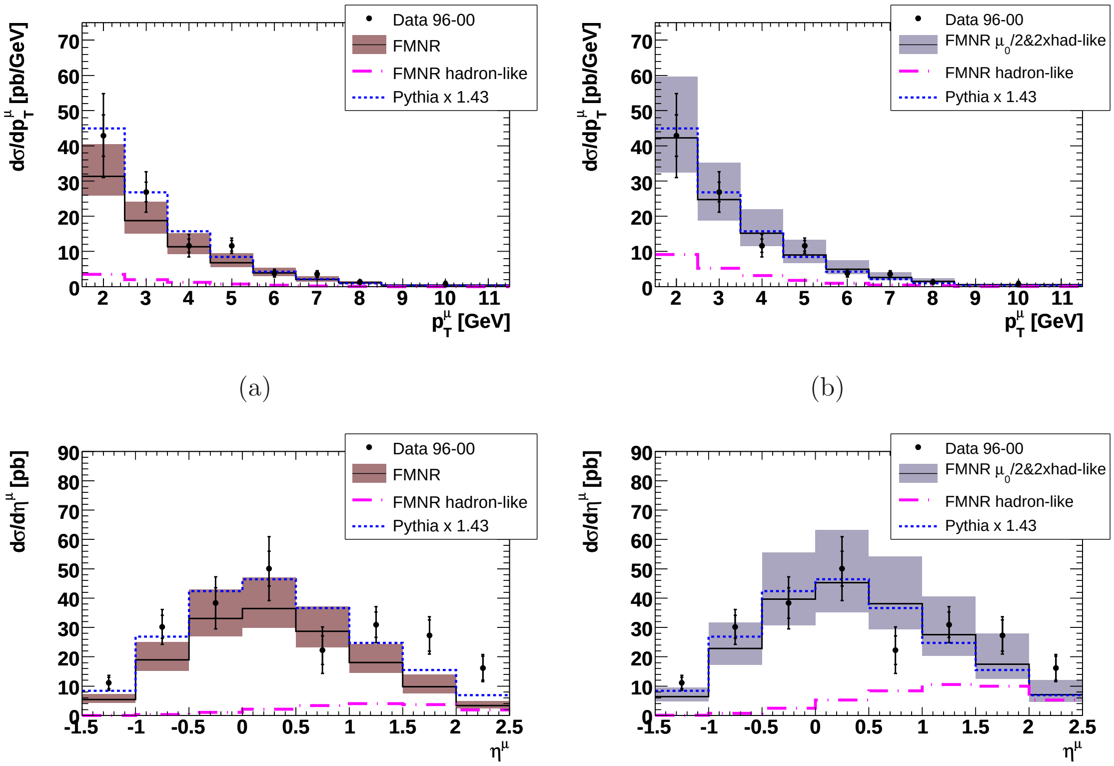

(a) (b)

(c) (d)

Figure 9.13: Cross-section as a function of the μ variables,p_T^μ, η^μ: Shown are the comparisons of the measured cross-section with the predictions by the Monte Carlo and the NLO calculations at hadron level using (a),(c) the standard FMNR parameter set, and (b),(d) the new set of parameters using $\mu_{R,F} = \mu_0/2$ and a doubled hadron-like cross-section.

10. Summary

In the study of the fundamental structure of matter, the main aim of this thesis was the measurement of cross-sections for open $b\bar{b}$ production at HERA, with a special emphasis on beauty dijet correlation cross-sections. The *ep* collision data used for the cross-section determination was recorded with the ZEUS detector between 1996 and 2000. Beauty was tagged by looking for semi-leptonic decays of B hadrons into muons. The kinematic range was restricted to photoproduction with four-momentum transfers $Q^2 < 1\,\mathrm{GeV}$.

An important ingredient of this analysis was the general muon finder, GMUON, which combines information from different muon finders based on information from the calorimeter, the muon chambers, the instrumented iron yoke and central tracking devices. The redundancy of the muon finder algorithms and the larger geometrical coverage increased the muon finding efficiency. Together with a lower cut on the p_T^μ of 1.5 GeV the statistics could be increased by a factor 10 compared to a previous analysis, leading to a factor 7.5 more beauty events. This opened the possibility to measure the cross-sections as a function of $p_T^\mu, \eta^\mu, p_T^{\mu\text{-jet}}$ and $\eta^{\mu\text{-jet}}$ in a finer binning and to measure beauty dijet correlations at ZEUS for the first time.

The p_T^{rel} method was used to determine the fraction of beauty events in the data in a two parameter fit of the beauty signal and background from light flavour and charm.

The cross-section measurement has been compared to the LO+PS Monte Carlo, PYTHIA, as well as to fixed order massive next-to-leading-order calculations using the FMNR program. An overall agreement within errors was found between the measurements and the theoretical predictions. While for the comparison to the next-to-leading-order predictions using the natural scale μ_0 the data was always above or at the higher edge of the predictions, the change of scale to $\mu_0/2$, motivated by theoretical considerations, agrees better with the measurements. From the separate measurement of the dijet correlations in the direct-enriched and non-direct-enriched regions, the hadron-like NLO cross-section, which mainly comes from the gluon content of the photon, is too low. Increasing it by a factor of two improves the agreement between data and NLO in all measured cross-sections.

Unfortunately the errors on the measurements are still large in the differential cross-sections. Using the whole HERA I+II data would increase the statistics by a further factor five. A large systematic error arises from the fixed ratio of charm and light flavour events and the uncertainty in the background p_T^{rel} distribution. In the HERA II data additional lifetime information provides the possibility to determine the three fractions independently and to reduce the influence of the systematic uncertainty due to the misdescription of the p_T^{rel} background distribution. This should give a more conclusive answer on the hadron-like NLO cross-section, which could be used to improve the photon PDF.

As a preparation for a HERA II analysis, tagging the beauty using lifetime information, requiring only one or no jet at all, a major task of this thesis was the development of a method to determine the light flavour background directly from the data, using fake muon probabilities determined from Monte Carlo. This method has been tested on the beauty dijet analysis as well as on a dimuon analysis with no jet requirements. In both analysis the agreement with alternative background determination methods was very good, therefore using these probabilities it should also be possible to predict the fake muon background in a region between these two kinematic regions.

A. Muon Quality Definition

Qual	Finder Combination	CTD match	match DCA cut	vtx ass.	mip prob.	mom. or rap.
6	BREMAT 5dof	yes	> 0.01	yes	-	-
	MPMATCH or	yes	> 0.05	-	-	-
	MUFO	yes	> 0.05	-	-	-
	MPMATCH +MV	yes	> 0.01	-	> 0.6	$p > 1$
	MUFO + MV	yes	< 0.05	-	> 0.6	$p > 1$
5	BREMAT 4dof + MV	yes	> 0.01	yes	> 0.6	$\|\eta\| > 0.6$
	MUBAC + MV	yes	-	yes	> 0.6	$\|\eta\| > 0.6$
	MUBAC+BREMAT 4dof+MV	yes	> 0.01	yes	> 0.6	$\|\eta\| < 0.6$
	MUBAC+BREMAT 5dof+MV	yes	> 0.01	no	> 0.6	-
	MPMATCH or	yes	> 0.01,	-	-	-
	MUFO	yes	< 0.05	-	-	-
	MAMMA+CTD	yes	-	-	impl.	-
4	BREMAT 4dof	yes	> 0.01	yes	-	-
	MUBAC	yes	50 cm	yes	-	-
	MUBAC+MV	yes	120 cm	yes	> 0.6	$\|\eta\| < 0.6$
	MUBAC+MIP	yes	120 cm	-	impl.	-
	MUFO other vtx	no	-	yes	-	-
	MCTS + MV	no	-	no	-	-
	MAMMA + vtx	no	-	yes	impl.	-
3	MV	yes	-	yes	> 0.95	$p > 1$
	BREMAT 5dof	yes	> 0.01	no	-	-
	GLOMU + MV	yes	implicit	-	> 0.6	-
	MUBAC + MV	yes	120 cm	-	> 0.4	$p > 1$
	MUBAC + GLOMU	yes	implicit	-	> 0.6	-
	MAMMA	no	-	-	impl.	-
2	MV	yes	-	yes	> 0.8	$p > 1$
	MCTS	no	-	no	-	-
	BAC	yes	120 cm	yes	-	-
	BREMAT 4dof	yes	> 0.01	no	-	-

	GLOMU	yes	implicit	-	-	-
1	MV	yes	-	yes	> 0.6	$p > 1$
0	MV CAL only	-	-	-	> 0.4	$p > 1$
	MIP	yes	-	-	impl.	$p_t > 2$
-1	BREMAT 5dof	yes	< 0.01	-	-	-
-2	BREMAT 4dof	yes	< 0.01	-	-	-
	MCTS rec. problem	no	-	no	-	-
-3	any finder,same VC track	yes	-	-	-	-
-999	simulatet μ not rec	-	-	-	-	$p > 1, p_t > .5$
-999	simulatet π/K decay, not rec	-	-	-	-	$p > 1, p_t > .5$

Table A.1: Definition of the standard GMUON quality

B. Efficiency Correction Factors

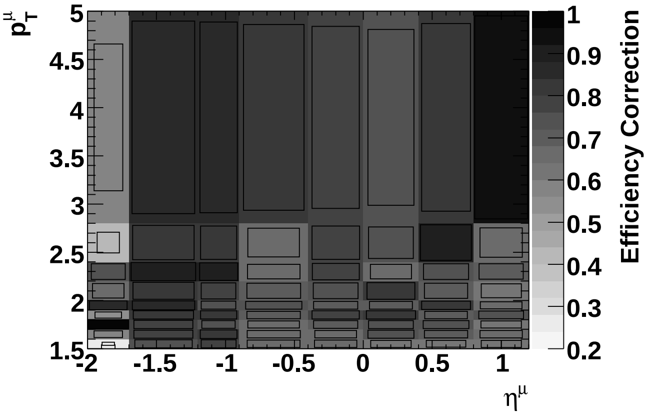

(a) Loose configuration

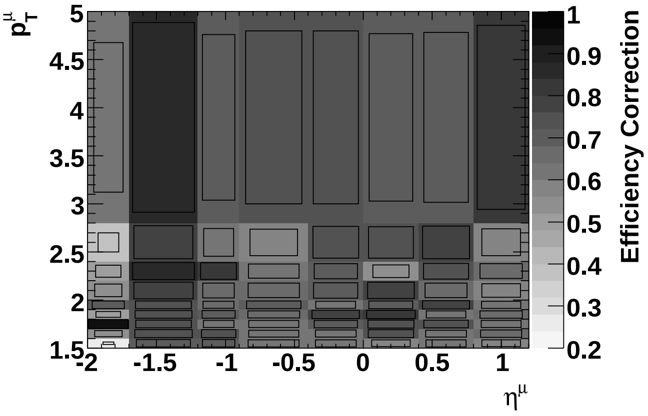

(b) Tight configuration

Figure B.1: Muon efficiency correction factors for the central/rear muon chambers (BREMAT algorithm) in the loose and tight configuration. The area of the rectangles is proportional to the correction factor.

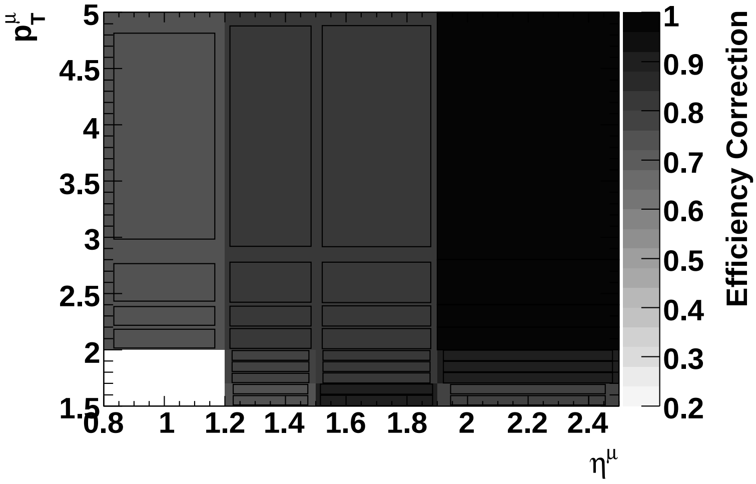

(a) Loose configuration

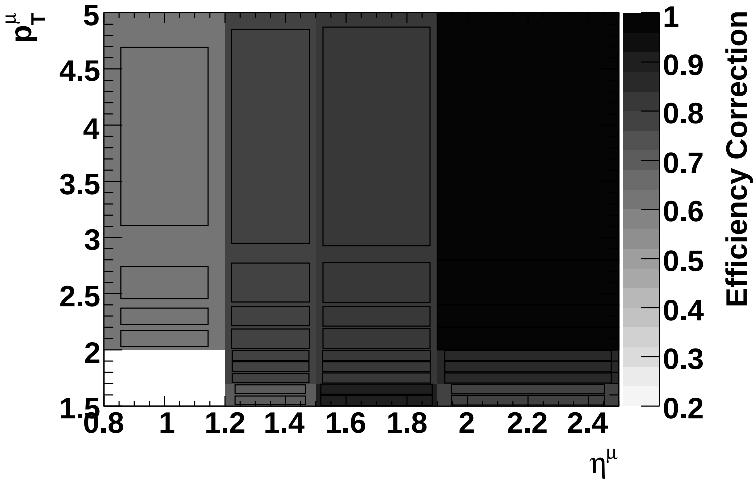

(b) Tight configuration

Figure B.2: Muon efficiency correction factors for the forward muon chambers (MP-MATCH algorithm) in the loose and tight configuration. The area of the rectangles is proportional to the correction factor.

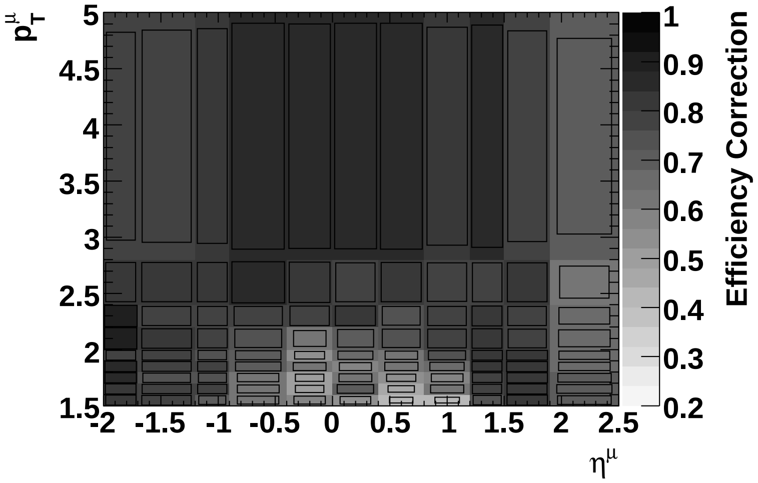

(a) Loose configuration

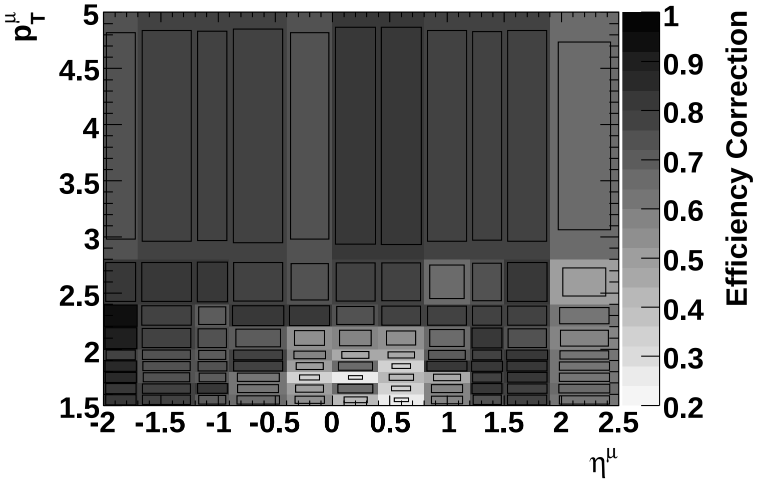

(b) Tight configuration

Figure B.3: Muon efficiency correction factors for the BAC (MUBAC algorithm) in the loose and tight configuration. The area of the rectangles is proportional to the correction factor.

C. Monte-Carlo Sample processes

C.1. Beauty Quark MC Samples

Beauty direct processes:

$$\gamma g \rightarrow b\bar{b}$$

Beauty resolved processes:

$$\begin{aligned} q\bar{q} &\rightarrow b\bar{b} \\ gg &\rightarrow b\bar{b} \end{aligned}$$

Beauty excitation in the proton processes:

$$\begin{aligned} b\gamma &\rightarrow bg \\ bg &\rightarrow bg \\ bq &\rightarrow bq \\ b\bar{b} &\rightarrow b\bar{b} \end{aligned}$$

Beauty excitation in the photon processes:

$$\begin{aligned} bg &\rightarrow bg \\ bq &\rightarrow bq \end{aligned}$$

C.2. Charm Quark MC Samples

Charm direct processes:

$$\gamma g \rightarrow c\bar{c}$$

Charm resolved processes:

$$\begin{aligned} q\bar{q} &\rightarrow c\bar{c} \\ gg &\rightarrow c\bar{c} \end{aligned}$$

Charm excitation in the proton processes:

$$\begin{aligned} c\gamma &\rightarrow cg \\ cg &\rightarrow cg \\ cq &\rightarrow cq \\ c\bar{c} &\rightarrow c\bar{c} \end{aligned}$$

Charm excitation in the photon processes:

$$\begin{aligned} cg &\rightarrow cg \\ cq &\rightarrow cq \end{aligned}$$

C.3. Inclusive MC Samples

Direct processes:

$$\gamma g \rightarrow q\bar{q}$$
$$\gamma q \rightarrow qg$$

Resolved processes:

$$\begin{aligned} q\bar{q} &\rightarrow q\bar{q} \\ q\bar{q} &\rightarrow q\prime\bar{q}\prime \\ q\bar{q} &\rightarrow gg \\ qg &\rightarrow qg \\ gg &\rightarrow q\bar{q} \\ gg &\rightarrow gg \end{aligned}$$

D. Trigger Selection

D.1. HPP14: Low E_T Dijet

- 2 or more jets with $E_T \geq 4\,\text{GeV}$ and $|\eta| < 2.5\,\text{GeV}$;
- CAL:$p_z/E < 1.0$;
- logical OR of second level trigger slots SLT HPP 1,2,3;
- logical OR of first level trigger slots: FLT 40,41,42,43, required by SLT HPP 1,2,3.

D.2. EXO12/12: Barrel/Rear Muon Trigger

- one outer barrel/rear muon reconstructed with the GLOMU algorithm;
- reject if (anti-cosmic muon cut):
  - $N_{tracks(CTD)} \leq 3$ and
  - $E_{FCAL} < 1\,\text{GeV}$ and
  - two highest p_t tracks have $p_t > 0.5\,\text{GeV}$ and $(\cos(\theta_{tracks}) < -0.9998)$;
- CAL timing cut compatible with physics event;
- logical OR of first level trigger slots FLT14 (barrel muon) and FLT15 (rear muon).

D.3. MUO3: Semi-Isolated Muon in Barrel/Rear Muon Chambers

- good inner barrel/rear muon found on second level trigger;
- hit in barrel or rear CAL with $p_t > 1\,\text{GeV}$;
- muon-like CAL island;
- $N_{tracks(CTD)} \geq 1$;
- track going into barrel or rear CAL with $p_t > 1\,\text{GeV}$;

- second level trigger slot: SLT MUO 1;
- included logical OR of first level trigger slots FLT 8,9,10,11 required by SLT MUO 1.

D.4. HFL1: Muon plus Dijets

- only available for 99-00 data;
- good muon found by barrel/rear muon chambers;
- 2 or more jets with $E_T \geq 3.5\,\mathrm{GeV}$ and $|\eta| < 2.5\,\mathrm{GeV}$;
- CAL:$p_z/E < 1.0$;
- CAL:$E - p_z < 100$;
- logical OR of second level trigger SLT HPP 1,2,3;
- logical OR of first level trigger FLT 40,41,42,43 required by SLT slots.

E. Comparison of Beauty Fractions

Comparison of the beauty fraction obtained from the fit of the p_T^{rel} variable using Monte Carlo for the background and using the fake-muon method (open points) for each differential bin. All fractions agree well with each other.

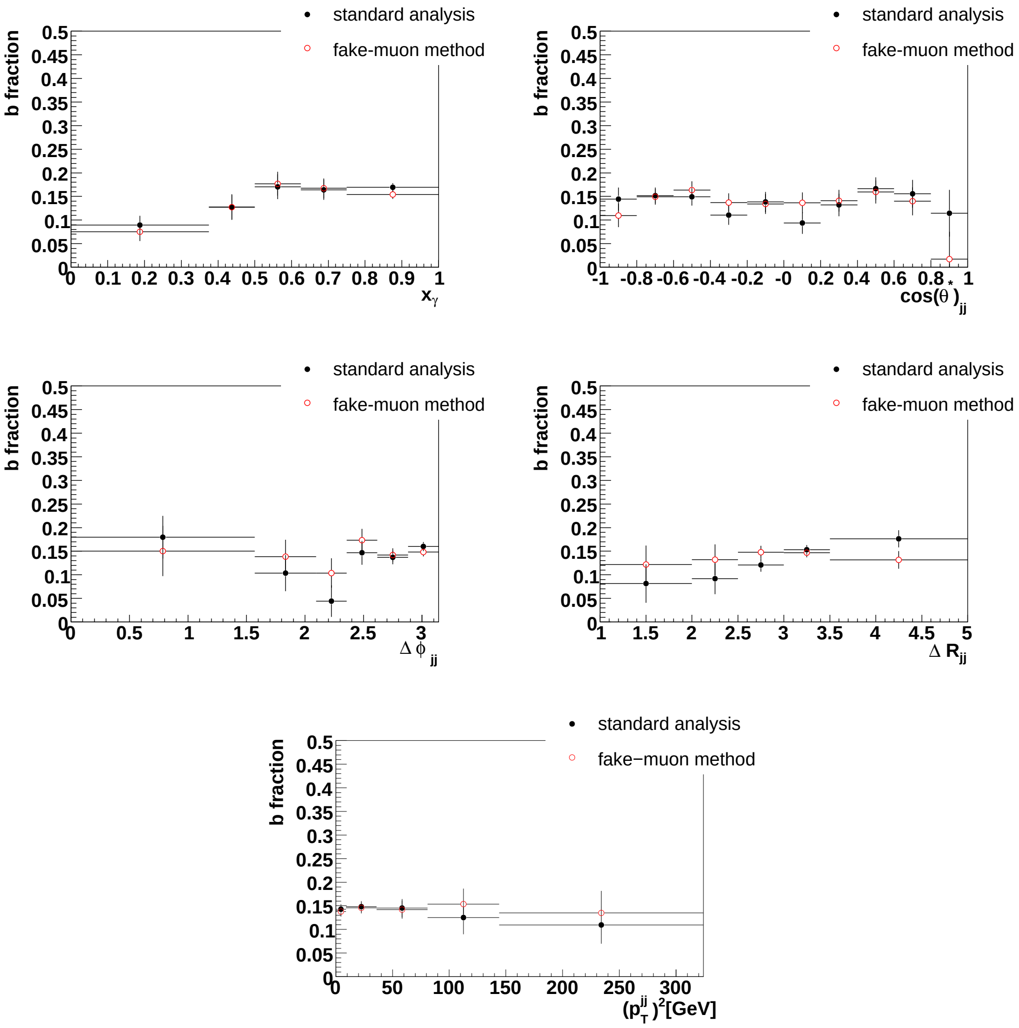

Figure E.1: Comparison of the beauty fraction for the jet correlation variables, $x_\gamma, \cos\theta^*, \Delta\phi^{jj}, \Delta R^{jj}$ and $(p_T^{\text{jets}})^2$.

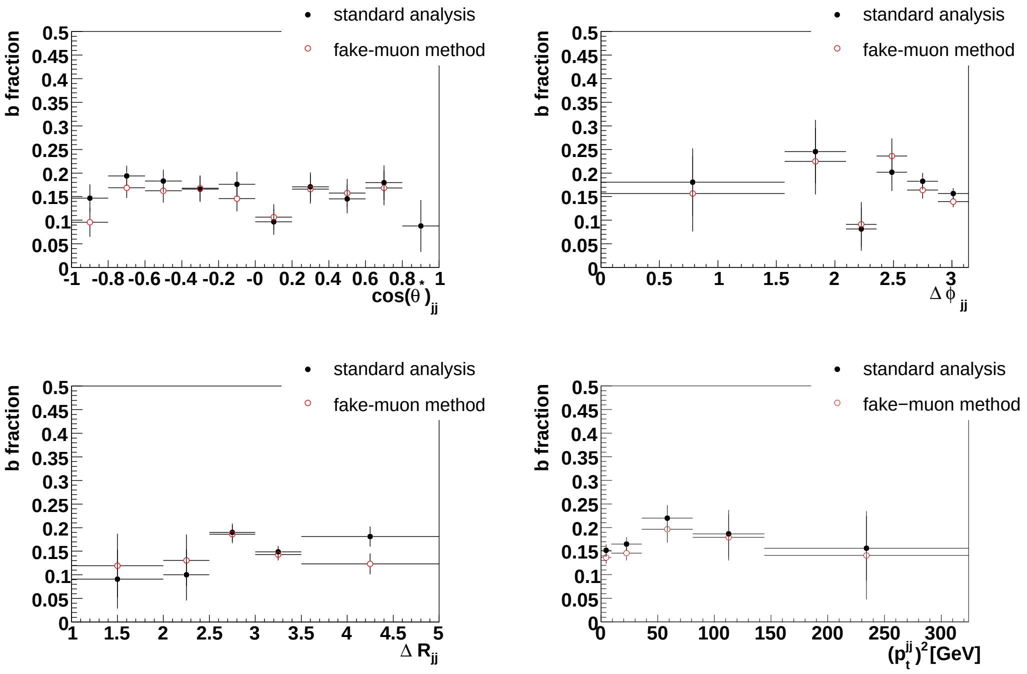

Figure E.2: Comparison of the beauty fraction for $x_\gamma > 0.75$

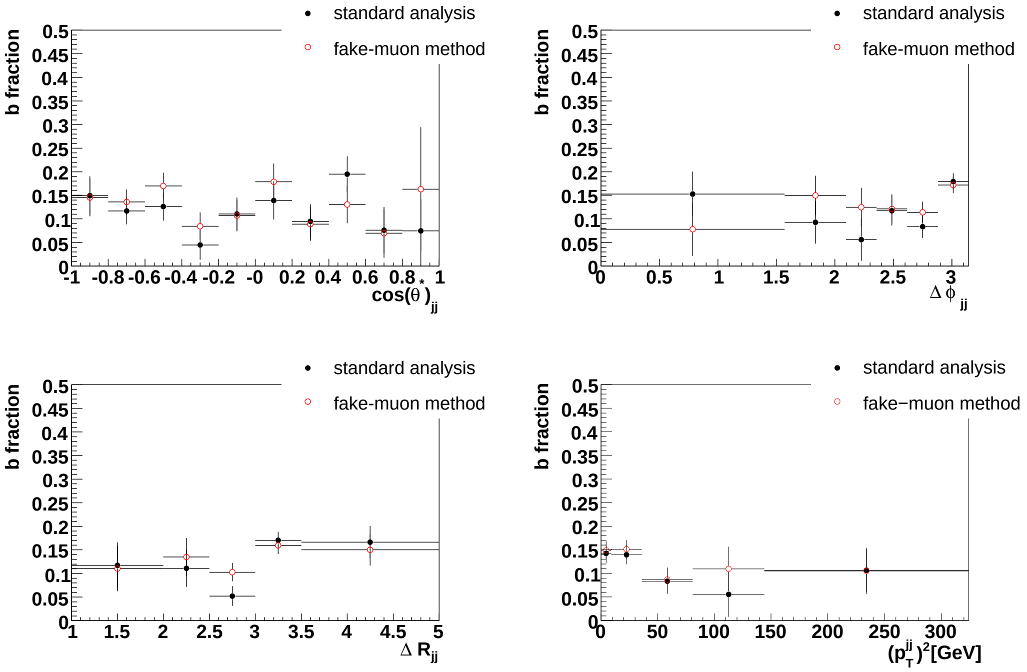

Figure E.3: Comparison of the beauty fraction for $x_\gamma < 0.75$

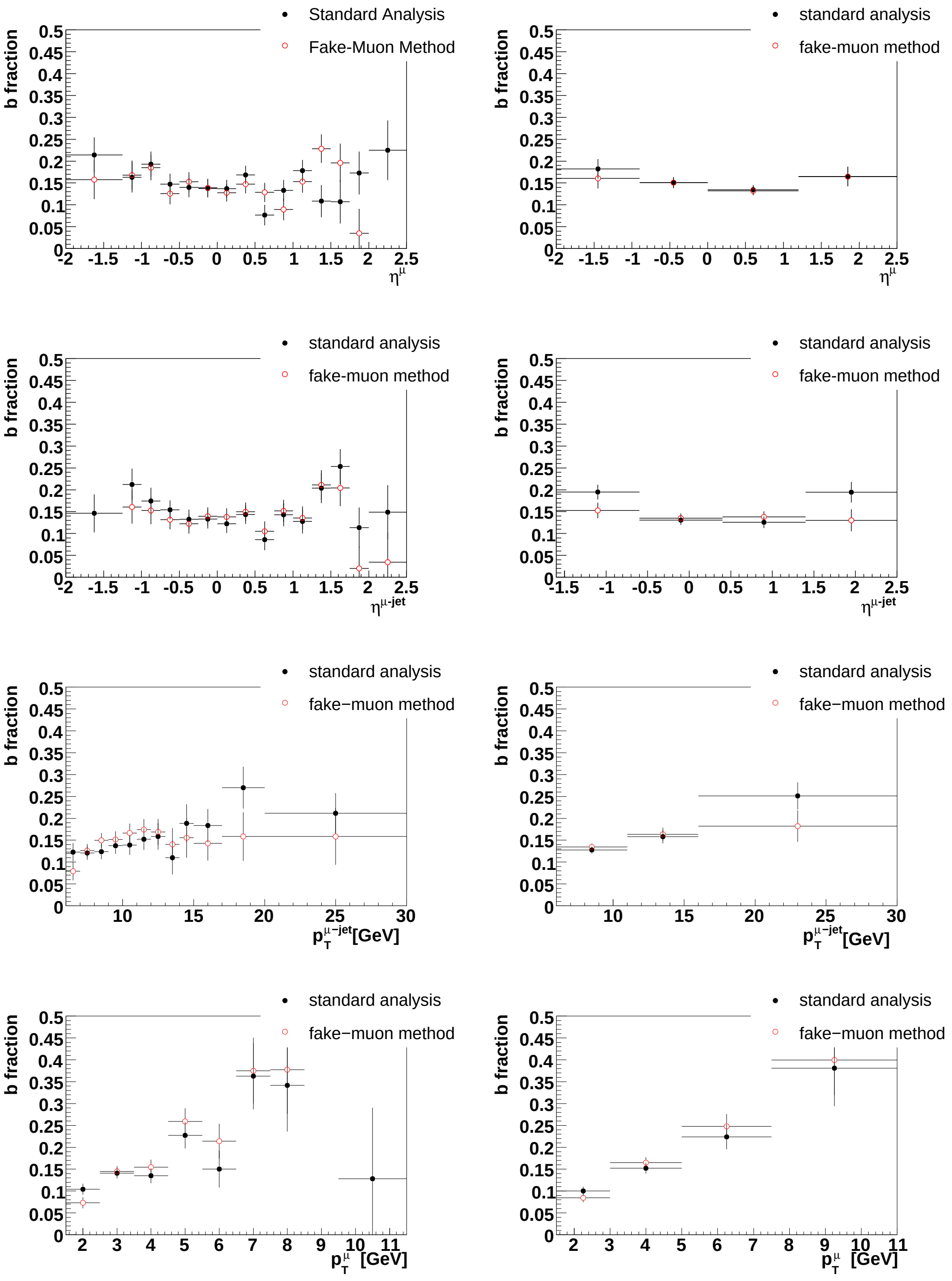

Figure E.4: Comparison of the beauty fraction for the muon and muon-jet variables.

F. Cross-Section Numbers

Given are the acceptances, purities, cross-sections with statistical error, the systematic uncertainty and the uncertainty due to the jet-energy scale uncertainty. In the last column the value of the hadronic correction for the comparison to the NLO QCD predictions are given. All systematic uncertainties are calculated bin-by-bin except for the jet-energy uncertainty. For the jet-energy uncertainty a global error of 2% is applied.

p_T^μ Range [GeV]	Acc	Pur	$d\sigma/dp_T^\mu$±stat. $^{+}_{-}$ sys ±E-scale [pb/GeV]	C_{had}±stat
1.5 : 2.5	0.34	0.58	42.91±5.86 $^{+11.92}_{-11.42}$ ±0.86	0.87±0.01
2.5 : 3.5	0.45	0.65	26.90±2.78 $^{+5.73}_{-5.6}$ ±0.54	0.88±0.01
3.5 : 4.5	0.48	0.71	11.64±1.88 $^{+3.18}_{-3.16}$ ±0.23	0.89±0.02
4.5 : 5.5	0.49	0.75	11.63±1.53 $^{+2.17}_{-2.17}$ ±0.23	0.93±0.02
5.5 : 6.5	0.56	0.77	3.82±0.92 $^{+1.1}_{-1.1}$ ±0.08	0.96±0.03
6.5 : 7.5	0.60	0.76	3.56±0.85 $^{+0.95}_{-0.95}$ ±0.07	0.97±0.05
7.5 : 8.5	0.66	0.75	1.33±0.58 $^{+0.6}_{-0.6}$ ±0.03	0.97±0.07
8.5 : 11.5	0.60	0.80	0.75±0.24 $^{+0.75}_{-0.75}$ ±0.01	0.97±0.07

Table F.1: p_T^μ cross-section numbers.

η^μ Range	Acc	Pur	$d\sigma/d\eta^\mu$±stat. $^{+}_{-}$ sys ±E-scale [pb]	C_{had}±stat
-1.5 : -1.0	0.47	0.42	11.10±1.97 $^{+2.56}_{-2.57}$ ±0.22	0.81±0.03
-1.0 : -0.5	0.46	0.55	30.21±3.92 $^{+5.94}_{-5.96}$ ±0.6	0.86±0.02
-0.5 : 0.0	0.50	0.65	38.37±5.18 $^{+8.86}_{-8.86}$ ±0.77	0.89±0.01
0.0 : 0.5	0.49	0.69	50.05±5.95 $^{+10.91}_{-10.85}$ ±1	0.89±0.01
0.5 : 1.0	0.45	0.72	22.28±4.84 $^{+7.91}_{-7.61}$ ±0.45	0.91±0.01
1.0 : 1.5	0.29	0.74	30.97±4.29 $^{+6.11}_{-5.96}$ ±0.62	0.92±0.02
1.5 : 2.0	0.22	0.70	27.29±5.31 $^{+6.36}_{-6.32}$ ±0.55	0.90±0.02
2.0 : 2.5	0.14	0.66	16.13±4.10 $^{+4.62}_{-4.63}$ ±0.32	0.81±0.03

Table F.2: η^μ cross-section numbers.

$p_T^{\mu\text{-jet}}$ Range [GeV]	Acc	Pur	$d\sigma/dp_T^{\mu\text{-jet}} \pm$stat. $^{+}_{-}$ sys $\pm$E-scale [pb/GeV]	$C_{had} \pm$stat
6.0 : 8.0	0.41	0.60	$12.70 \pm 1.81\ ^{+3.64}_{-3.49} \pm 0.25$	0.90 ± 0.01
8.0 : 9.0	0.38	0.67	$15.46 \pm 2.49\ ^{+3.85}_{-3.80} \pm 0.31$	0.86 ± 0.01
9.0 : 10.0	0.43	0.68	$13.34 \pm 2.02\ ^{+3.01}_{-2.98} \pm 0.27$	0.87 ± 0.02
10.0 : 11.0	0.45	0.66	$10.20 \pm 1.74\ ^{+2.37}_{-2.36} \pm 0.20$	0.88 ± 0.02
11.0 : 12.0	0.46	0.69	$7.95 \pm 1.48\ ^{+1.90}_{-1.90} \pm 0.16$	0.88 ± 0.02
12.0 : 13.0	0.47	0.68	$5.57 \pm 1.27\ ^{+1.53}_{-1.52} \pm 0.11$	0.88 ± 0.03
13.0 : 15.0	0.50	0.67	$4.27 \pm 0.79\ ^{+1.03}_{-1.02} \pm 0.09$	0.91 ± 0.02
15.0 : 18.0	0.50	0.65	$2.22 \pm 0.45\ ^{+0.54}_{-0.54} \pm 0.04$	0.88 ± 0.02
18.0 : 30.0	0.40	0.62	$0.63 \pm 0.12\ ^{+0.14}_{-0.14} \pm 0.01$	0.88 ± 0.03

Table F.3: $p_T^{\mu\text{-jet}}$ cross-section numbers.

$\eta^{\mu\text{-jet}}$ Range	Acc	Pur	$d\sigma/d\eta^{\mu\text{-jet}} \pm$stat. $^{+}_{-}$ sys $\pm$E-scale [pb]	$C_{had} \pm$stat
-1.5 : -1.0	0.36	0.35	$14.95 \pm 2.55\ ^{+3.33}_{-3.34} \pm 0.30$	0.70 ± 0.02
-1.0 : -0.5	0.45	0.55	$29.34 \pm 3.62\ ^{+5.48}_{-5.50} \pm 0.59$	0.81 ± 0.01
-0.5 : -0.0	0.51	0.65	$31.63 \pm 4.73\ ^{+7.95}_{-8.00} \pm 0.63$	0.81 ± 0.01
-0.0 : 0.5	0.52	0.68	$39.55 \pm 5.34\ ^{+9.57}_{-9.52} \pm 0.79$	0.88 ± 0.01
0.5 : 1.0	0.49	0.71	$24.83 \pm 4.95\ ^{+8.26}_{-8.01} \pm 0.50$	0.93 ± 0.01
1.0 : 1.5	0.33	0.72	$29.53 \pm 4.75\ ^{+6.85}_{-6.63} \pm 0.59$	1.00 ± 0.02
1.5 : 2.0	0.24	0.68	$37.21 \pm 5.13\ ^{+6.87}_{-6.80} \pm 0.74$	1.00 ± 0.02
2.0 : 2.5	0.14	0.61	$15.25 \pm 5.11\ ^{+5.58}_{-5.58} \pm 0.30$	1.04 ± 0.03

Table F.4: $\eta^{\mu\text{-jet}}$ cross-section numbers.

x_γ Range	Acc	Pur	$d\sigma/dx_\gamma \pm$stat. $^{+}_{-}$ sys $\pm$E-scale [pb]	$C_{had} \pm$stat
0.0 : 0.4	0.42	0.56	$24.12 \pm 6.67\ ^{+10.51}_{-9.99} \pm 0.48$	0.73 ± 0.02
0.4 : 0.5	0.51	0.59	$61.50 \pm 13.13\ ^{+25.65}_{-25.58} \pm 1.23$	0.85 ± 0.03
0.5 : 0.6	0.65	0.59	$63.58 \pm 12.55\ ^{+25.45}_{-25.54} \pm 1.27$	0.85 ± 0.02
0.6 : 0.8	0.89	0.62	$58.53 \pm 9.00\ ^{+13.48}_{-13.55} \pm 1.17$	0.88 ± 0.02
0.8 : 1.0	0.37	0.70	$300.12 \pm 18.14\ ^{+57.26}_{-57.38} \pm 6.00$	1.00 ± 0.01

Table F.5: x_γ cross-section numbers.

$\Delta\phi^{jj}$ Range	Acc	Pur	$d\sigma/d\Delta\phi^{jj}$±stat. [pb]	$^{+}_{-}$ sys	±E-scale	C_{had}±stat
0.0 : 1.6	1.40	0.47	0.43±0.24	$^{+0.27}_{-0.27}$	±0.01	0.76±0.11
1.6 : 2.1	1.08	0.49	1.97±1.14	$^{+1.36}_{-1.32}$	±0.04	0.75±0.07
2.1 : 2.5	0.63	0.61	8.19±3.77	$^{+5.29}_{-5.16}$	±0.16	0.79±0.03
2.5 : 2.7	0.60	0.63	57.02±7.39	$^{+11.34}_{-11.15}$	±1.14	0.82±0.02
2.7 : 3.0	0.47	0.67	125.21±11.94	$^{+23.44}_{-23.38}$	±2.50	0.88±0.01
3.0 : 3.1	0.34	0.69	340.14±29.09	$^{+56.44}_{-57.63}$	±6.80	0.92±0.01
$x_\gamma > 0.75$						
0.0 : 1.6	0.77	0.47	0.36±0.15	$^{+0.16}_{-0.16}$	±0.01	0.62±0.16
1.6 : 2.1	1.18	0.57	1.37±0.46	$^{+0.51}_{-0.51}$	±0.03	0.76±0.14
2.1 : 2.5	0.47	0.67	6.16±2.51	$^{+2.83}_{-2.82}$	±0.12	0.82±0.04
2.5 : 2.7	0.52	0.68	38.26±5.03	$^{+8.20}_{-8.18}$	±0.77	0.82±0.02
2.7 : 3.0	0.42	0.71	93.07±9.51	$^{+19.44}_{-19.53}$	±1.86	0.90±0.01
3.0 : 3.1	0.30	0.71	232.77±24.65	$^{+49.89}_{-50.32}$	±4.66	0.93±0.01
$x_\gamma < 0.75$						
0.0 : 1.6	1.67	0.47	0.05±0.18	$^{+0.19}_{-0.18}$	±0	0.84±0.15
1.6 : 2.1	1.04	0.45	1.00±1.06	$^{+1.22}_{-1.19}$	±0.02	0.74±0.08
2.1 : 2.5	0.81	0.57	3.37±2.52	$^{+3.36}_{-3.30}$	±0.07	0.75±0.04
2.5 : 2.7	0.73	0.57	15.65±4.98	$^{+7.23}_{-7.11}$	±0.31	0.82±0.03
2.7 : 3.0	0.62	0.60	34.59±6.57	$^{+11.57}_{-11.61}$	±0.69	0.80±0.02
3.0 : 3.1	0.49	0.63	97.71±13.79	$^{+26.26}_{-26.42}$	±1.95	0.84±0.02

Table F.6: $\Delta\phi^{jj}$ cross-section numbers.

ΔR^{jj} Range	Acc	Pur	$d\sigma/d\Delta R^{jj}$±stat. $^{+}_{-}$ sys ±E-scale [pb]	C_{had}±stat
1.0 : 2.0	1.33	0.50	$0.00\pm2.70\ ^{+2.71}_{-2.70}\ \pm0$	0.78±0.10
2.0 : 2.5	0.77	0.60	$3.93\pm1.96\ ^{+2.53}_{-2.42}\ \pm0.08$	0.72±0.04
2.5 : 3.0	0.57	0.67	$36.48\pm5.14\ ^{+9.27}_{-8.93}\ \pm0.73$	0.82±0.01
3.0 : 3.5	0.41	0.69	$109.01\pm8.07\ ^{+18.11}_{-18.30}\ \pm2.18$	0.89±0.01
3.5 : 5.0	0.31	0.60	$15.96\pm1.88\ ^{+2.75}_{-2.78}\ \pm0.32$	0.95±0.01
$x_\gamma > 0.75$				
1.0 : 2.0	1.06	0.50	$0.15\pm0.14\ ^{+0.15}_{-0.15}\ \pm0$	0.76±0.19
2.0 : 2.5	0.57	0.63	$3.13\pm1.17\ ^{+1.31}_{-1.30}\ \pm0.06$	0.75±0.06
2.5 : 3.0	0.50	0.71	$31.02\pm3.68\ ^{+6.64}_{-6.64}\ \pm0.62$	0.84±0.02
3.0 : 3.5	0.37	0.72	$71.85\pm6.56\ ^{+15.07}_{-15.19}\ \pm1.44$	0.91±0.01
3.5 : 5.0	0.26	0.65	$11.98\pm1.62\ ^{+2.62}_{-2.62}\ \pm0.24$	0.97±0.02
$x_\gamma < 0.75$				
1.0 : 2.0	1.44	0.50	$0.00\pm0.60\ ^{+0.60}_{-0.60}\ \pm0$	0.79±0.12
2.0 : 2.5	0.99	0.58	$1.88\pm1.41\ ^{+1.71}_{-1.64}\ \pm0.04$	0.70±0.06
2.5 : 3.0	0.71	0.61	$7.08\pm3.28\ ^{+5.08}_{-4.88}\ \pm0.14$	0.78±0.02
3.0 : 3.5	0.57	0.62	$35.14\pm4.27\ ^{+9.50}_{-9.55}\ \pm0.70$	0.82±0.01
3.5 : 5.0	0.51	0.50	$3.54\pm0.82\ ^{+1.17}_{-1.20}\ \pm0.07$	0.89±0.03

Table F.7: ΔR^{jj} cross-section numbers.

$(P_T^{jj})^2$ Range [GeV^2]	Acc	Pur	$d\sigma/d(P_T^{jj})^2$±stat. $^{+}_{-}$ sys ±E-scale [pb/GeV^2]	C_{had}±stat
0.0 : 9.0	0.27	0.67	$6.22\pm0.57\ ^{+1.14}_{-1.16}\ \pm0.12$	0.91±0.01
9.0 : 36.0	0.68	0.68	$0.93\pm0.08\ ^{+0.16}_{-0.16}\ \pm0.02$	0.85±0.01
36.0 : 81.0	0.92	0.66	$0.17\pm0.03\ ^{+0.04}_{-0.04}\ \pm0.003$	0.82±0.02
81.0 : 144.0	1.06	0.63	$0.04\pm0.01\ ^{+0.02}_{-0.02}\ \pm0.001$	0.80±0.05
144.0 : 324.0	1.03	0.58	$0.01\pm0.00\ ^{+0.004}_{-0.004}\ \pm0.000$	0.81±0.07
$x_\gamma > 0.75$				
0.0 : 9.0	0.23	0.70	$4.95\pm0.49\ ^{+1.02}_{-1.03}\ \pm0.10$	0.93±0.01
9.0 : 36.0	0.65	0.72	$0.57\pm0.06\ ^{+0.12}_{-0.12}\ \pm0.01$	0.87±0.01
36.0 : 81.0	0.94	0.70	$0.12\pm0.02\ ^{+0.03}_{-0.03}\ \pm0.002$	0.84±0.03
81.0 : 144.0	1.09	0.67	$0.02\pm0.01\ ^{+0.01}_{-0.01}\ \pm0.000$	0.88±0.07
144.0 : 324.0	0.93	0.60	$0.00\pm0.00\ ^{+0.00}_{-0.00}\ \pm0.000$	0.80±0.11
$x_\gamma < 0.75$				
0.0 : 9.0	0.43	0.60	$1.38\pm0.25\ ^{+0.45}_{-0.45}\ \pm0.03$	0.83±0.02
9.0 : 36.0	0.75	0.60	$0.38\pm0.06\ ^{+0.11}_{-0.11}\ \pm0.01$	0.81±0.02
36.0 : 81.0	0.89	0.59	$0.05\pm0.02\ ^{+0.029}_{-0.029}\ \pm0.001$	0.78±0.03
81.0 : 144.0	1.03	0.59	$0.01\pm0.01\ ^{+0.016}_{-0.015}\ \pm0.000$	0.72±0.06
144.0 : 324.0	1.10	0.56	$0.00\pm0.00\ ^{+0.0034}_{-0.0033}\ \pm0.000$	0.81±0.08

Table F.8: $(P_T^{jj})^2$ cross-section numbers.

M^{jj} Range [GeV]	Acc	Pur	$d\sigma/dM^{jj}$±stat. [pb/GeV]	$^{+}_{-}$ sys	±E-scale	C_{had}±stat
0 : 5	0	0	0±0	$^{+0}_{-0}$	±0.00	0±0
5 : 10	0	0	0±0	$^{+0}_{-0}$	±0.00	0±0
10 : 15	20.90	0.5	0.004±0.004	$^{+0.005}_{-0.004}$	±0.00	0.14±0.05
15 : 20	0.87	0.63	1.50±0.29	$^{+0.56}_{-0.52}$	±0.03	0.43±0.01
20 : 25	0.78	0.69	4.89±0.88	$^{+1.26}_{-1.25}$	±0.10	0.92±0.01
25 : 30	0.37	0.69	5.31±0.56	$^{+0.91}_{-0.91}$	±0.11	1.02±0.01
30 : 35	0.38	0.69	2.85±0.44	$^{+0.62}_{-0.62}$	±0.06	1.05±0.02
35 : 40	0.39	0.66	2.23±0.35	$^{+0.45}_{-0.45}$	±0.04	1.09±0.03
40 : 45	0.36	0.66	1.34±0.27	$^{+0.31}_{-0.31}$	±0.03	1.07±0.03
45 : 60	0.36	0.63	0.54±0.10	$^{+0.12}_{-0.12}$	±0.01	1.09±0.03
$x_\gamma > 0.75$						
0.0 : 5.0	0	0	0±0	$^{+0}_{-0}$	±0.00	0±0
5.0 : 10.0	0	0	0±0	$^{+0}_{-0}$	±0.00	0±0
10.0 : 15.0	0	0.61	0±0.0	$^{+0.001}_{-0.001}$	±0.00	0.33±0.15
15.0 : 20.0	0.70	0.67	1.52±0.22	$^{+0.35}_{-0.35}$	±0.03	0.44±0.01
20.0 : 25.0	0.31	0.73	3.80±0.52	$^{+0.89}_{-0.90}$	±0.08	0.95±0.01
25.0 : 30.0	0.33	0.73	3.63±0.43	$^{+0.77}_{-0.77}$	±0.07	1.04±0.02
30.0 : 35.0	0.35	0.73	1.81±0.33	$^{+0.47}_{-0.47}$	±0.04	1.07±0.02
35.0 : 40.0	0.37	0.70	1.46±0.27	$^{+0.37}_{-0.37}$	±0.03	1.12±0.03
40.0 : 45.0	0.37	0.69	1.04±0.22	$^{+0.29}_{-0.29}$	±0.02	1.08±0.04
45.0 : 60.0	0.33	0.67	0±0	$^{+0}_{-0}$	±0.00	1.10±0.03
$x_\gamma < 0.75$						
0.0 : 5.0	0	0	0±0	$^{+0}_{-0}$	±0.00	0±0
5.0 : 10.0	0	0.60	0±0	$^{+0}_{-0}$	±0.00	0±0
10.0 : 15.0	56.36	0.43	0.003±0.002	$^{+0.002}_{-0.002}$	±0.00	0.07±0.04
15.0 : 20.0	1.32	0.58	0.34±0.16	$^{+0.25}_{-0.23}$	±0.01	0.42±0.02
20.0 : 25.0	0.59	0.62	1.51±0.37	$^{+0.59}_{-0.59}$	±0.03	0.83±0.02
25.0 : 30.0	0.50	0.61	1.58±0.39	$^{+0.53}_{-0.53}$	±0.03	0.97±0.03
30.0 : 35.0	0.48	0.61	0.97±0.27	$^{+0.39}_{-0.39}$	±0.02	1.00±0.04
35.0 : 40.0	0.48	0.55	0.65±0.22	$^{+0.26}_{-0.26}$	±0.01	1.00±0.05
40.0 : 45.0	0.44	0.59	0.43±0.12	$^{+0.16}_{-0.16}$	±0.01	1.02±0.07
45.0 : 60.0	0.46	0.54	0.21±0.05	$^{+0.07}_{-0.07}$	±0.004	1.06±0.06

Table F.9: M^{jj} cross-section numbers.

$\cos\theta^*$ Range			Acc	Pur	$d\sigma/d\cos\theta^*$±stat. $^{+}_{-}$ sys ±E-scale [pb]	C_{had}±stat
-0.830	:	-0.664	0.47	0.61	94.56±17.18 $^{+22.45}_{-22.52}$ ±1.89	0.90±0.02
-0.664	:	-0.332	0.50	0.67	54.92±12.89 $^{+18.35}_{-18.09}$ ±1.10	0.87±0.01
-0.332	:	0.000	0.48	0.67	43.09±13.28 $^{+17.41}_{-17.00}$ ±0.86	0.85±0.01
0.000	:	0.332	0.45	0.70	27.77±11.89 $^{+15.44}_{-14.93}$ ±0.56	0.86±0.01
0.332	:	0.664	0.38	0.70	55.70±10.62 $^{+13.45}_{-13.38}$ ±1.11	0.88±0.01
0.664	:	0.830	0.28	0.67	46.95±11.81 $^{+13.20}_{-13.20}$ ±0.94	0.96±0.02
$x_\gamma > 0.75$						
-0.830	:	-0.664	0.38	0.67	72.70±9.77 $^{+15.94}_{-15.96}$ ±1.45	0.94±0.02
-0.664	:	-0.332	0.43	0.71	48.24±5.99 $^{+10.52}_{-10.55}$ ±0.96	0.90±0.02
-0.332	:	0.000	0.44	0.71	38.93±5.27 $^{+8.84}_{-8.86}$ ±0.78	0.87±0.02
0.000	:	0.332	0.41	0.73	24.00±5.37 $^{+7.55}_{-7.59}$ ±0.48	0.88±0.02
0.332	:	0.664	0.34	0.74	33.93±6.07 $^{+8.99}_{-9.02}$ ±0.68	0.90±0.02
0.664	:	0.830	0.25	0.72	40.78±9.32 $^{+11.58}_{-11.59}$ ±0.82	0.98±0.03
$x_\gamma < 0.75$						
-0.830	:	-0.664	0.70	0.51	20.95±7.62 $^{+10.94}_{-11.34}$ ±0.42	0.82±0.03
-0.664	:	-0.332	0.67	0.60	22.32±5.43 $^{+9.82}_{-9.73}$ ±0.45	0.80±0.02
-0.332	:	0.000	0.59	0.60	9.05±4.46 $^{+6.12}_{-5.87}$ ±0.18	0.79±0.02
0.000	:	0.332	0.63	0.63	12.72±3.65 $^{+4.97}_{-4.84}$ ±0.25	0.77±0.03
0.332	:	0.664	0.55	0.63	16.45±3.02 $^{+4.74}_{-4.73}$ ±0.33	0.80±0.03
0.830	:	0.830	0.44	0.54	1.72±4.29 $^{+4.47}_{-4.48}$ ±0.03	0.88±0.05

Table F.10: $\cos\theta^*$ cross-section numbers.

References

[1] A. Salam, *Weak and electromagnetic interactions*, in *Selected Papers on Gauge Theory of Weak and Electromagnetic Interactions*, ed. C.H. Lai, p. 188. World Scientific, Singapore, 1981. Reprint of A. Salam, *Weak and Electromagnetic Interactions* in *Elementary Particle Theory* ed. N. Svartholm (Almqvist and Wiskell, Stockholm, 1968);
S. Weinberg, Phys. Rev. Lett. **19**, 1264 (1967);
S.L. Glashow, Nucl. Phys. **22**, 579 (1961).

[2] F. Halzen and A.D. Martin, *Quarks and Leptons: An Introductory Course in Modern Particle Physics.* John Wiley & Sons, Inc, 1984.

[3] H. David Politzer, Phys. Rev. Lett. **30**, 1346 (1973);
H. David Politzer, Phys. Rep. **14**, 129 (1974);
D. J. Gross,Frank Wilczek, Phys. Rev. **D 8**, 3633 (1973);
D. J. Gross,Frank Wilczek, Phys. Rev. Lett. **30**, 1343 (1973);
D. J. Gross,Frank Wilczek, Phys. Rev. **D 9**, 980 (1974).

[4] Particle Data Group, W.-M Yao et al., Journal of Physics G **33**, 1+ (2006).

[5] W.A. Bardeen et al., Phys. Rev. **D 18**, 3998 (1978).

[6] John C. Collins, hep-ph/9510276 (1995).

[7] Particle Data Group, D.E. Groom et al., Eur. Phys. J. **C 15**, 1 (2000).

[8] C.G. Callan and D.J. Gross, Phys. Rev. Lett. **22**, 156 (1969).

[9] A. M. Cooper-Sarkar,R. C. E. Devenish, A. De Roeck **A 13**, 3385 (1998).

[10] R.K. Ellis et al., Nucl. Phys. **B 152**, 285 (1979);
John C. Collins, D.E. Soper and G. Sterman, Nucl. Phys. **B 261**, 2616 (1985);
G.T. Bodwin, Nucl. Phys. **D 31**, 104 (1985).

[11] G. Altarelli and G. Parisi, Nucl. Phys. **B 126**, 298 (1977).

[12] ZEUS Coll., S. Chekanov et al., Phys. Rev. **D 67**, 012007 (2003).

[13] C.F. von Weizsäcker, Z. Phys. **88**, 612 (1934).

[14] E.J. Williams, Phys. Rev. **45**, 729 (1934).

[15] Bo Andersson, *THE LUND STRING MODEL*. In *Durham 1984, Proceedings, Antiproton 1984*, 447-462.

[16] Frixione, Stefano, *Theory versus experiments in heavy flavour production*, 2001.

[17] C. Peterson et al., Phys. Rev. **D 27**, 105 (1983).

[18] P. Nason and C. Oleari, Nucl. Phys. **B565**, 245 (2000).

[19] B. Andersson, G. Gustafson and B. Söderberg, Z. Phys. **C 20**, 317 (1983).

[20] Kartvelishvili, V. G. and Likhoded, A. K. and Petrov, V. A., Phys. Lett. **B78**, 615 (1978).

[21] UA1 Coll., Albajar,Cet al., Z. Phys. **C 61**, 41 (1994).

[22] V. Blobel and E. Lohrmann, *Statistische und numerische Methoden der Datenanalyse*, in Teubner-Studienbücher : Physik. B.G. Teubner, Stuttgart, (Germany), 1998. In German.

[23] T. Sjöstrand, L. Lönnblad, and S. Mrenna, Preprint hep-ph/0108264, 2001.

[24] J. Kroseberg, *A Measurement of Beauty Production in High-Energy Positron-Proton Scattering*. PhD Thesis, University of Zurich, 2002.

[25] Belle Coll., K. Abe et al., Phys. Lett. **B 547**, 181 (2002).

[26] BaBar Coll., B. Auert et al., Phys. Rev. **D 67**, 031101 (2002).

[27] M. Corradi, M. Turcato, *Beauty Production in Dijet Events*, 2004. ZEUS-04-005 Internal note.

[28] R. Brun, F. Bruyant, M. Maire, A.C. McPherson, P. Zanarini, *GEANT3*, revised 1987. CERN-DD/EE/84-1.

[29] S. Frixione et al., Nucl. Phys. **B 412**, 225 (1994).

[30] B. Mele, P. Nason, and G. Ridolfi, Nucl. Phys. **B 357**, 409 (1991).

[31] S. W. Herb et al., Phys. Rev. Lett. **39**, 252 (1977).

[32] Stefano Frixione, Michelangelo L. Mangano, Paolo Nason, and Giovanni Ridolfi, *Heavy-quark production*, 1998, available on `http://de.arxiv.org/pdf/hep-ph/9702287`.

[33] HERA-B Collaboration, I. Abt et al., *Improved measurement of the b-bbar production cross-section in 920 GeV fixed-target proton nucleus collisions*, 2005, available on `http://de.arxiv.org/ps/hep-ex/0512030`.

[34] UA1 Coll., C. Albajar et al., Z. Phys. **C 61**, 41 (1994).

[35] C. Albajar et al., Phys. Lett. **B 256**, 121 (1991). Erratum in Phys. Lett. **B 262**, 497 (1991).

[36] D0 Coll., B. Abbott et al., 2000, available on `http://de.arxiv.org/pdf/hep-ex/9905024`; CDF Coll., F. Abe et al., Phys. Rev. Lett. **71**, 2396 (1993).

[37] Michelangelo L. Mangano, *The saga of bottom production in proton-antiproton collisions*, 2004, available on `http://de.arxiv.org/pdf/hep-ph/0411020`.

[38] CDF Coll., *b-bbar Dijet Production using SVT*, 2000, available on `http://www-cdf.fnal.gov/physics/new/qcd/bb_SVT_07/bbcross.html`.

[39] Chekanov, S. and others, Phys. Rev. **D70**, 012008 (2004).

[40] ZEUS Coll., S. Chekanov et al., *Beauty photoproduction in dijet events measured using decays into electrons*, 2007, available on `http://www-zeus.desy.de/physics/hfla/public/abstracts07/paper/BtoeHeraI.ps`.

[41] ZEUS Coll., S. Chekanov et al., *Measurement of beauty photoproduction at HERA II*, 2007, available on `http://www-zeus.desy.de/physics/hfla/public/abstracts07/paper/BtomuHeraII.ps`.

[42] ZEUS Coll., S. Chekanov et al., Nucl. Phys. **B 729**, 492 (2005).

[43] ZEUS Coll., S. Chekanov et al., Phys. Lett. **B 565**, 87 (2003).

[44] A.A. Sololov and I.M. Ternov, Sov.Phys.Dok **8**, 1203 (1964).

[45] B. Foster et al., Nucl. Inst. Meth. **A 338**, 254 (1994).

[46] R. Hall-Wilton et al., *The CTD Tracking Resolution* (unpublished). ZEUS-99-024, internal ZEUS-note, 1999.

[47] M. Derrick et al., Nucl. Inst. Meth. **A 309**, 77 (1991).

[48] A. Andresen et al., Nucl. Inst. Meth. **A 309**, 101 (1991).

[49] A. Caldwell et al., Nucl. Inst. Meth. **A 321**, 356 (1992).

[50] ZEUS Coll., U. Holm (ed.), *The ZEUS Detector*. Status Report (unpublished), DESY (1993), available on `http://www-zeus.desy.de/bluebook/bluebook.html`.

[51] G. Abbiendi et al., Nucl. Inst. Meth. **A 333**, 342 (1993).

[52] M. De Giorgi et al., Nucl. Inst. Meth. **A 378**, 472 (1996).

[53] H. Bethe and W. Heitler, Proc. Roy. Soc. Lond. **A 146**, 83 (1934).

[54] H. A. Bethe, Phys. Rev. **89**, 1256 (1953).

[55] K. Piotrzkowski and M. Zachara, *Determination of the ZEUS Luminosity in 1994* (unpublished). ZEUS-95-138, 1995.

[56] ZEUS Luminosity Group, *Proposal of an Upgrade Luminosity Monitor for the ZEUS Experiment*, Proposal, DESY, 1999.

[57] A. Caldwell, S. Paganis, R. Sacchi, F. Sciulli, *A Luminosity Spectrometer for ZEUS*, Proposal, DESY, 1999.

[58] S.M. Fisher and P. Palazzi, *ADAMO Programmers Manual – Version 3.2.* CERN ECP, available on `http://adamo.web.cern.ch/Adamo/programmers_manual/TOC_of_adamo.html`.

[59] G.F. Hartner et al., *VCTRAK(3.07/04): Offline Output Information* (unpublished). ZEUS-97-064, internal ZEUS Note, 1997.

[60] G.F. Hartner, *VCTRAK Briefing: Program and Math* (unpublished). ZEUS-98-058, internal ZEUS Note, 1998.

[61] J. Repond, *Jet Energy Corrections* (unpublished). ZEUS-96-133, internal ZEUS Note, 1996.

[62] N. Tuning, *ZUFOs: Hadronic Final State Reconstruction with Calorimeter, Tracking and Backsplash Correction* (unpublished). ZEUS-01-021, internal ZEUS Note, 2001.

[63] G. M. Briskin, *Diffractive dissociation in ep Deep Inelastic Scattering.* PhD Thesis, Tel Aviv University, School of physics and Astronomy, 1998. DESY-THESIS-1998-036.

[64] A. Longhin, *Misura delle sezioni d'urto di fotoproduzione di Open Beauty ad HERA. (In italian).* Master's thesis, University of Padua, 2000.

[65] J.E. Huth et al., *Research Directions for the Decade. Proceedings of Summer Study on High Energy Physics, 1990*, E.L. Berger (ed.), p. 134. World Scientific (1992). Also in preprint FERMILAB-CONF-90-249-E.

[66] S. Catani, Y. Dokshitzer, L. Yuri, B.R. Webber, Phys. Lett. **B285**, 291 (1992).

[67] S.Catani et al., Nucl. Phys. **B 406**, 187 (1993).

[68] A. Geiser, *GMUON - a general ZEUS muon finder*, 2006. ZEUS-06-016 Internal note.

[69] The phantom library.
/afs/desy.de/group/zeus.zsmsm/ZEUSSysSoft/Released/zeus/ZeusUtil/phantom.

[70] V. Kuzmin, Nucl. Inst. Meth. **A 453**, 336 (2000).

[71] G. Abbiendi et al., *Observation of J/psi* $\rightarrow \mu^+\mu^-$ *in the first* $274nb^{-1}$ *of the 1993 run*, 1993. ZEUS-93-120 Internal note.

[72] G. Abbiendi, *Global Tracking of muons in the Barrel and Rear region*, 1999. ZEUS-99-063 Internal note.

[73] GEANE description. In: GEANT 3.15, Detector Description and Simulation Tool, CERN Program Library Long Writeup W5013, CERN 1993.

[74] R. Ciesielski, available on
`http://www-zeus.desy.de/~robertc/ZEUS_ONLY/mubac.html`.

[75] L. Bellagamba, *MVMATCH: A package to match FMUON tracks with Central Detectors*, 1996. ZEUS-96-051 Internal note.

[76] M. Corradi, available on
`http://www-zeus.desy.de/~corradi/ZEUS_ONLY/mpmatch/mpmatch2.html`.

[77] R.E. Kalman, Transactions of the ASME-Journal of Basic Engineering, Series D **82**, 35 (1960).

[78] G. Bruni, available on
`http://www-zeus.desy.de/~bruni/ZEUS_ONLY/muons.html`.

[79] M. Corradi, *Efficiency corrections for the muon finders BREMAT and MPMATCH2*, 2004. ZEUS-04-006 Internal note.

[80] A. Geiser et al., *Muon efficiency corrections for GMUON*, 2008. ZEUS internal note in preparation.

[81] J. Botts et al., Phys. Lett. **B 304**, 159 (1995).

[82] M. Glück, E. Reya and A. Vogt, Z. Phys. **C 53**, 127 (1992).

[83] ZEUS Coll., M. Derrick et al., Phys. Lett. **B 346**, 399 (1995).

[84] F. Jacquet and A. Blondel, *Proceedings of the Study for an ep Facility for Europe*, U. Amaldi (ed.), p. 391. Hamburg, Germany (1979). Also in preprint DESY 79/48.

[85] H. Abramowicz, A. Caldwell and R. Sinkus, Nucl. Inst. Meth. **A 365**, 508 (1995);
R. Sinkus and T. Voss, Nucl. Inst. Meth. **A 391**, 360 (1997).

[86] M. Turcato, *Measurement of beauty photoproduction at HERA*. PhD Thesis, University of Padua, 2003. DESY-THESIS-2003-039.

[87] H1 Coll., T. Ahmed et al., Phys. Lett. **B 297**, 205 (1992);
ZEUS Coll., M. Derrick et al., Phys. Lett. **B 297**, 404 (1992);
ZEUS Coll., M. Derrick et al., Phys. Lett. **B 322**, 287 (1994).

[88] ZEUS Coll., S. Chekanov et al., Phys. Rev. **D 70**, 12008 (2004).

[89] F. James, *Minuit v94.1, CERN Program Library Long Writeup D506* (unpublished), available on `http://wwwinfo.cern.ch/asdoc/minuit/minmain.html`.

[90] A. Longhin, *Fake-muon probabilities studies*, 2005. ZEUS-05-001 Internal note.

[91] I. Bloch, *Measurement of beauty production from dimuon events at HERA / ZEUS*. DESY-THESIS-2005-034.

[92] ZEUS Collaboration; S. Chekanov et al., Eur. Phys. J. **C 50**, 299 (2007).

[93] ZEUS Coll., S. Chekanov et al., Eur. Phys. J. **C 44**, 351 (2005).

[94] A. Geiser, *Review of Beauty Production at HERA and Elsewhere*, available on `http://dx.doi.org/10.3360/dis.2007.163`.

[95] CTEQ Coll., H.L. Lai et al., Eur. Phys. J. **C 12**, 375 (2000).

[96] A.D. Martin et al., Eur. Phys. J. **C 4**, 463 (1998).

[97] M. Glück, E. Reya and A. Vogt, Phys. Rev. **D 46**, 1973 (1992).

[98] P. Aurenche, J.P. Guillet and M. Fontannaz, Z. Phys. **C 64**, 621 (1994).

[99] S. Frixione and B.R. Webber, JHEP **06**, 029 (2002);
S. Frixione, P. Nason and B.R. Webber, JHEP **08**, 007 (2003).

List of Figures

List of Tables